

**Document Version**

Final published version

**Citation (APA)**

Wegman, T. M. (2026). *Observations of estuarine salt intrusion in the Rhine-Meuse Delta*. [Dissertation (TU Delft), Delft University of Technology]. <https://doi.org/10.4233/uuid:cc7dd871-5396-47a2-98b4-e3d30ae34a01>

**Important note**

To cite this publication, please use the final published version (if applicable).  
Please check the document version above.

**Copyright**

In case the licence states "Dutch Copyright Act (Article 25fa)", this publication was made available Green Open Access via the TU Delft Institutional Repository pursuant to Dutch Copyright Act (Article 25fa, the Taverne amendment). This provision does not affect copyright ownership.  
Unless copyright is transferred by contract or statute, it remains with the copyright holder.

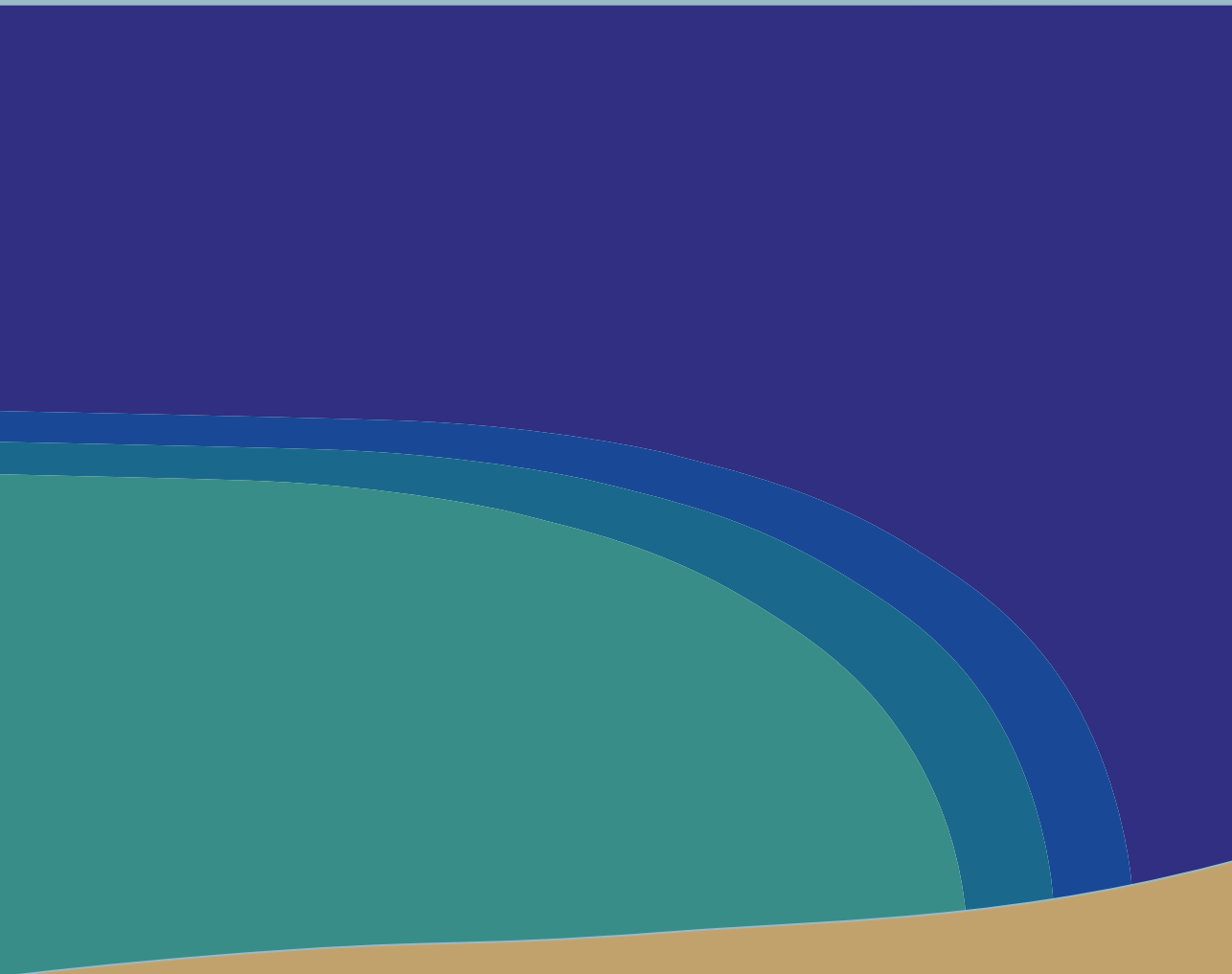
**Sharing and reuse**

Other than for strictly personal use, it is not permitted to download, forward or distribute the text or part of it, without the consent of the author(s) and/or copyright holder(s), unless the work is under an open content license such as Creative Commons.

**Takedown policy**

Please contact us and provide details if you believe this document breaches copyrights.  
We will remove access to the work immediately and investigate your claim.

# Observations of estuarine salt intrusion in the Rhine-Meuse Delta



Tess Wegman

# **Observations of estuarine salt intrusion in the Rhine-Meuse Delta**

Tess Wegman



# **Observations of estuarine salt intrusion in the Rhine-Meuse Delta**

**DISSERTATION**

for the purpose of obtaining the degree of doctor  
at Delft University of Technology  
by the authority of the Rector Magnificus,  
Prof. dr. ir. H. Bijl;  
Chair of the Board for Doctorates  
to be defended publicly on  
Thursday 26 March 2026 at 12:30.

by

**Tess Megan WEGMAN**

This dissertation has been approved by the promotor.

Composition of the doctoral committee:

Rector Magnificus	chairperson
Prof. dr. J. D. Pietrzak	Delft University of Technology, <i>promotor</i>
Prof. dr. A. R. Horner-Devine	University of Washington, USA, <i>promotor</i>
Prof. dr. ir. H. A. Dijkstra	Utrecht University, <i>promotor</i>

*Independent members:*

Prof. dr. ir. A. J. H. M. Reniers	Delft University of Technology
Prof. dr. H. M. Schuttelaars	Delft University of Technology
Prof. dr. H. Burchard	The University of Rostock
Prof. dr. A. Valle-Levinson	University of Florida, USA
Dr. ir. B. C. van Prooijen	Delft University of Technology, <i>reserve member</i>



SALTISolutions



This PhD thesis is part of the SALTISolutions Program with project number P18-32 Project 2 of the TTW Perspectief Programme which is partly financed by the Dutch Research Council (NWO).

*Keywords:* salt intrusion; estuary; turbulence; Rhine-Meuse Delta; wind and tidal forcing; field observations

*Printed by:* Ipskamp Printing

*Cover by:* Tess Wegman

Copyright ©2026 by T. M. Wegman

ISBN 978-94-6536-075-1

An electronic copy of this dissertation is available at

<https://repository.tudelft.nl/>.

# Contents

Summary .....	v
Samenvatting .....	vii
Plain Language Summary .....	ix
<b>1 Introduction .....</b>	<b>1</b>
<b>2 Direct observations of turbulence in a salt wedge estuary.....</b>	<b>11</b>
<b>3 Observations of estuarine salt intrusion dynamics during a prolonged drought event in the Rhine-Meuse Delta .....</b>	<b>39</b>
<b>4 Influences of tides and winds on estuarine inflow conditions .....</b>	<b>67</b>
<b>5 Conclusions and Outlook.....</b>	<b>101</b>
References .....	109
Acknowledgements.....	123
<b>A Supplementary Figures of Chapter 2 .....</b>	<b>125</b>
<b>B Supplementary Figures of Chapter 3 .....</b>	<b>129</b>
<b>C Supplementary Figures of Chapter 4 .....</b>	<b>133</b>
List of symbols .....	141
List of Publications .....	143
Curriculum Vitae .....	145



# Summary

Salt intrusion poses a global threat to estuaries and deltas and is exacerbated by climate change through processes such as sea-level rise and prolonged droughts. This thesis aims to increase the understanding of salt intrusion dynamics in a complex delta system, particularly during drought conditions, using extensive field observations from the Rhine–Meuse Delta, including both moored and ship-borne measurements.

Chapter 2 evaluates turbulence and vertical mixing in the Rotterdam Waterway, a salt wedge estuary in the Rhine-Meuse Delta. A novel data set of density, flow, and turbulence spanning multiple phases of two tidal cycles under contrasting river and tidal conditions is used to do both a qualitative and a quantitative comparison between these variables. Observations show that the Rotterdam Waterway has a stable salt wedge. It is dominated by velocity-shear-generated turbulence, where turbulence damping at the pycnocline is an important phenomenon that helps explain the observed turbulence characteristics. Results show that the gradient Richardson number is often a good measure of vertical mixing, which is supported by the performance of four gradient Richardson-number-based parameterisations of vertical mixing. In particular, the statistical behaviour of vertical mixing is, after calibration, well-resolved in these parameterisations. Accounting for the effect of the limited water depth using a parabolic shape function does not improve the performance of these parameterisations. These insights and the presented data set can potentially improve the representation of mixing in salt intrusion models.

Chapter 3 investigates the influence of river discharge, wind, and tidal variations on salt intrusion in the Rhine-Meuse Delta during drought. Key characteristics of this low-lying delta are its branching channel network and complicated, human-controlled discharge. The analysis is based on a 17-week data set of a historic drought in Europe, capturing dynamics under a wide range of conditions. Despite the system's complexity, we found that the subtidal salt intrusion length, defined as the location where salinity concentration equals 2 PSU ( $L_2$ ), follows a power law relationship with Rhine River discharge ( $L_2 \propto Q_R^{-0.35 \pm 0.03}$ ). Subtidal water level variations contribute to short-term variations in salt intrusion length, which can be attributed to the up-estuary transport of seawater, caused by the estuary adjusting to variations in water levels at its mouth. However, spring-neap variation in the tidal range has no discernible influence on subtidal salt intrusion length. Side branches exhibit distinct dynamics, mainly controlled by downstream salinity, underscoring the need to treat them separately to incorporate the highly variable downstream boundary condition.

Chapter 4 focuses on the dynamic inflow boundary at the estuary mouth, how this changes under the forcing of winds and tides, focusing on the Rhine-Meuse

Delta and the influence of plume processes on estuarine inflow salinity. Field data from the near-field region show that bottom salinity is primarily governed by the tidal amplitude with a 2.5-day lag, suggesting that tidal mixing of plume waters into the lower layer in the mid-field is the leading cause of lower-layer salinity variation in the near-field region. Just as estuarine mixing determines the salinity of outflowing waters, we find that plume mixing determines the salinity of inflowing waters. Although wind mixing has a minimal overall effect on bottom salinity, isolated events show short-term impacts on bottom salinity. Wind-driven transport by upwelling- and downwelling-favourable wind shows no significant impact on bottom salinity, but it does alter the near-field velocity boundary. The along-estuary salinity gradient also correlates with near-field bottom salinity, suggesting a role in modulating exchange flow and up-estuary salt transport. These findings suggest a pathway for estuarine inflow of salt water from the shelf sea, with salinity values influenced by mid-field plume mixing.

This thesis further advances the knowledge of salt intrusion in complex deltas, based on an observational study in the Rhine-Meuse Delta. Observations of intratidal flow, density, and turbulence patterns show the importance of velocity shear-induced turbulence generation and turbulence damping at the pycnocline. Fitting of Richardson-number-based parameterisations shows promising results for the statistical representation of turbulence. Idealised subtidal relations between salt intrusion and forcing of river discharge and set-up hold in the main estuary. Side branches with distinct dynamics have to be treated separately, where the downstream boundary is an important control. This dynamic boundary condition is also relevant for the main estuary. This thesis provides insights into the main variations in this dynamic boundary condition in the shallow shelf sea, where the salinity changes are imposed by spring-neap variations of mid-field plume mixing.

# Samenvatting

Zoutindringing vormt wereldwijd een groeiend probleem voor estuaria en delta's en wordt versterkt door klimaatverandering via processen zoals zeespiegelstijging en langdurige droogteperiodes. Dit proefschrift beoogt het inzicht in de dynamiek van zoutindringing in een complex deltasysteem te vergroten, met bijzondere aandacht voor droogtecondities. Dit is gedaan op basis van uitgebreide veldobservaties in de Rijn-Maasdelta, waaronder zowel vaste meetopstellingen als metingen vanaf onderzoeksschepen.

Hoofdstuk 2 evalueert turbulentie en verticale menging in de Nieuwe Waterweg, een sterk gelaagd estuarium binnen de Rijn-Maasdelta. Een nieuwe dataset van dichtheid, stroming en turbulentie over twee getijcycli, onder verschillende rivier- en getijomstandigheden, is gebruikt voor zowel een kwalitatieve als kwantitatieve vergelijking. De waarnemingen laten zien dat de Nieuwe Waterweg een stabiele zouttong heeft, waarin turbulentie voornamelijk wordt gegenereerd door verticale snelheidsgradiënten, met duidelijke demping van turbulentie ter hoogte van de spronglaag. De resultaten tonen aan dat het Richardsongetal vaak een goede indicator is voor verticale menging. Dit wordt bevestigd door de goede werking van vier Richardsongetalgebaseerde parameterisaties, die na kalibratie het statistisch gedrag van verticale diffusiviteit goed beschrijven. Het meenemen van het effect van de beperkte waterdiepte via een paraboolvormige profielcorrectie leidt niet tot een betere prestatie van deze parameterisaties. De inzichten en dataset uit dit hoofdstuk kunnen bijdragen aan een verbeterde modellering van menging in zoutindringingsmodellen.

Hoofdstuk 3 onderzoekt de invloed van rivierafvoer, wind en getijvariabiliteit op zoutindringing in Rijn-Maasdelta tijdens een historische droogte. Kenmerkend voor dit laaglandgebied zijn het vertakte kanaalnetwerk en de sterk gereguleerde verdeling van rivierafvoer. De analyse is gebaseerd op een 17 weken durende veldmeetcampagne in de Rijn-Maasdelta, waarin dynamiek onder uiteenlopende omstandigheden is onderzocht. Ondanks de complexiteit van het systeem blijkt de getijgemiddelde lengte van zoutindringing, gedefinieerd aan de hand van de locatie van een zoutconcentratie van 2 PSU ( $L_2$ ), een duidelijk machtsverband te vertonen met de Rijnafvoer ( $L_2 \propto Q_R^{-0,35 \pm 0,03}$ ). Getijgemiddelde waterstandsvariabiliteit veroorzaakt kortetermijnschommelingen in de lengte van zoutindringing, doordat het estuarium zich aanpast aan veranderingen in waterstanden bij de monding. Spring-doodtijvariabiliteit in de getijamplitude blijken daarentegen geen invloed te hebben op de getijgemiddelde zoutindringing. Zijtakken vertonen een afwijkende dynamiek ten opzichte van de hoofdgeul, en de zoutindringing daarin wordt voornamelijk bepaald door de zoutconcentratie aan de benedenstroomse rand. Dit onderstreept het belang van een afzonderlijke benadering van zijtakken om de sterk variabele randvoorwaarden correct mee te nemen.

Hoofdstuk 4 richt zich op de dynamische instroomrandvoorwaarde bij de riviermonding en op de invloed van wind- en getijforcering hierop, met specifieke focus de Rijn-Maasdelta en de invloed van pluimprocessen op de instroomsaliniteit van het estuarium. Velddata nabij de riviermonding ("near-field") van de Rijnpluim laten zien dat de bodemsaliniteit in deze regio voornamelijk bepaald wordt door het getij, met een vertraging van circa 2,5 dag. Dit suggereert dat menging benedenstrooms in de rivierpluim ("mid-field") het zoutgehalte in de onderste waterlagen nabij de riviermonding beïnvloedt. Net zoals estuariene menging de saliniteit van uitstromend water bepaalt, laten de resultaten zien dat pluimmenging de saliniteit van instromend water bepaalt. Hoewel menging ten gevolge van wind over het algemeen een beperkt effect heeft, tonen enkele gevallen wel kortdurende invloeden op de bodemsaliniteit. Transport door kustparallele winden blijkt geen directe invloed te hebben op bodemsaliniteit, maar heeft wel effect op de snelheidsverdeling nabij de riviermonding. De bodemsaliniteit nabij de riviermonding correleert met zoutgehalten tot 27 km landinwaarts in het estuarium en met de zoutgradiënt in de lengterichting van het estuarium, wat wijst op een rol in het landinwaartse transport van zout. Deze bevindingen tonen een mechanisme voor zoutinstroom vanuit de zee naar het estuarium, waarbij de zoutconcentraties worden beïnvloed door menging in de rivierpluim, met name benedenstrooms van de monding. De resultaten benadrukken het belang van een nauwkeurige beschrijving van de randvoorwaarden aan de zeezijde om de respons van estuariene zoutverdeling op externe forcering goed te kunnen begrijpen en voorspellen.

Dit proefschrift levert nieuwe inzichten in zoutindringing in een complex deltasysteem, gebaseerd op gedetailleerde veldobservaties in de Rijn-Maasdelta. Waarnemingen van stroming, dichtheid en turbulentie binnen een getijcyclus tonen het belang van door snelheidsgradiënten opgewekte turbulentie en de demping van turbulentie aan de spronglaag. Parameterisaties gebaseerd op het Richardsongetal geven, na kalibratie, een goede statistische beschrijving van verticale menging. In de hoofdgeul gelden vereenvoudigde getijgemiddelde relaties tussen zoutindringing en forcering door rivierafvoer en opzet. Zijtakken moeten echter afzonderlijk worden benaderd vanwege hun specifieke dynamiek, waarbij de benedenstroomse randvoorwaarde een cruciale rol speelt. Deze dynamische randvoorwaarde blijkt ook van belang voor de hoofdgeul. Dit proefschrift levert de eerste inzichten in de variabiliteit van deze randvoorwaarde in de ondiepe kustzee, waarin zoutveranderingen worden veroorzaakt door spring-doodtijvariaties in menging benedenstrooms van de monding.

# Plain Language Summary

An estuary is where saline seawater and fresh river water meet and mix. During low river flow, seawater can be transported far upstream into normally fresh regions, a process known as salt intrusion. Salt intrusion can pose significant challenges, particularly during droughts, by stressing freshwater supplies for drinking, agriculture, and industry. Climate change is expected to worsen this problem through more frequent droughts and rising sea levels. To study salt intrusion, the distance seawater travels upstream is examined: a distance called the salt intrusion length. The goal of this thesis is to understand how winds, tides, and river flow influence the variations in salt intrusion length in a complex delta system.

As a real-world test case to study this problem, field measurements were done in the Rhine-Meuse Delta, the Netherlands. The Rhine-Meuse Delta estuary is more complex than most single-channel estuaries because of its branching channel network and human-controlled river discharge.

Chapter 2 focuses on mixing between salt and fresh water inside the estuary. Mixing is a key process that controls salt intrusion. Measurements of water flow velocity, salinity and a proxy for mixing showed that this complex process can be described by a relatively simple parameterisation balancing buoyancy (the tendency of lighter freshwater to float on top of denser saltwater) and mixing. This dataset also provides a valuable reference for testing and improving computer models of salt intrusion.

Chapter 3 shows that the salt intrusion length mainly depends on the amount of freshwater flowing in from the Rhine River. Short-term variations (lasting 1-3 days) are caused by water level variations at the river mouth, associated with storm surges. However, the spring-neap tidal cycle does not have a detectable effect on the tidally averaged salt intrusion length. Side branches behave differently from the main river; their salt intrusion length mainly depends on downstream salinity. This thesis shows that treating side branches separately is crucial.

Chapter 4 investigates how wind and tides affect water flow and salinity just offshore of the river mouth. Here, the bottom salinity in this region is primarily governed by the strength of the tidal currents. This relation lags 2.5 days, suggesting that mixing occurs farther offshore, not right at the mouth. Strong wind events also influence salinity near the river mouth. Salinity at the river mouth also correlates with salinity levels up to 27 kilometers inland, although this effect weakens farther into the estuary, where river flow becomes more important.

Overall, this thesis advances our understanding of salt intrusion in a complex delta system. The findings highlight how river flow, wind, and tides influence salt intrusion, especially under drought conditions, which are expected to occur more often with climate change.



# 1

## Introduction

### 1.1 Salt intrusion in estuaries

As the interface between river and sea, estuaries are vital coastal regions that sustain high population densities and major industrial activity. The upstream advection of seawater is a natural and essential aspect of estuarine dynamics. Problems arise when saline seawater is advected farther inland than usual, and it intrudes into regions that are normally freshwater. This process is referred to as salt intrusion. Salt intrusion can pose significant challenges, particularly during droughts, by stressing freshwater supplies for drinking, agriculture, and industry.

The extent to which saline waters enter the estuary, referred to as the salt intrusion length, depends on estuarine geometry and external forcings such as river discharge, tides, winds, and sea level (MacCready and Geyer, 2010). Climate change is expected to intensify salt intrusion globally due to rising sea levels and reduced low-flow discharges (Kay et al., 2018; Lee et al., 2025). In European estuaries, extreme salt intrusion events are expected to become five times more frequent by the end of the century (Lee et al., 2024), and similar trends are expected globally (Eslami et al., 2019, 2021b; Dai et al., 2011; Sherin et al., 2020; Liu et al., 2019; Hong et al., 2020; Lee et al., 2025).

In the Rhine-Meuse Delta (RMD), even small increases in salt intrusion can severely impact freshwater availability. As dry periods become more frequent (Lee et al., 2024), a deeper understanding of the physical drivers of salt intrusion is urgently needed.

While estuarine and coastal plume dynamics have been studied separately, few have examined the full continuum from the coastal ocean, through the estuary including its mixing processes, to the inland limit of salt intrusion, especially under severe drought conditions. This thesis addresses this knowledge gap by investigating salt intrusion across the full plume–estuary system in the complex and urbanised RMD under extreme low-flow conditions.

## 1.2 Context

### 1.2.1 Characteristics of estuaries and river plumes

An estuary is a partially enclosed, coastal water body where freshwater from rivers meets salt water from the ocean. Naturally, this is connected to the buoyant river water flowing into the coastal ocean, known as the river plume. The river plume can be divided into three dynamic regions (Fig. 1.1a): the near-field, the mid-field, and the far-field river plume (Horner-Devine et al., 2015). The near-field is the jet-like region of initial plume expansion, the mid-field, the region where Earth's rotation begins to dominate, deflecting the plume in the downcoast direction, and the far-field, where the plume becomes a buoyant coastal current.

In the estuary, the horizontal density gradient between the saline ocean and fresh river waters creates a density-driven flow, where fresh river water flows downstream at the surface, and saline salt water propagates upstream at depth (Fig. 1.1b), this is known as a salt wedge (Geyer and Ralston, 2011). This exchange flow pattern, with outflow at the surface and inflow at depth, is referred to as estuarine circulation or estuarine exchange flow (Geyer and MacCready, 2014).

Another important mechanism in estuaries is the mixing of saline and fresh waters, which is primarily driven by tidal currents and wind-induced turbulence (Geyer and MacCready, 2014). The salt balance in an estuary is a competition between buoyancy inputs and mixing processes, which together determine the import and export of salt.

The farthest extent of saline waters into the estuary is referred to as the salt intrusion length. This can be defined as the upstream distance at which a certain salinity concentration is found. The remainder of the introduction discusses the key processes that influence salt intrusion length in an estuary.

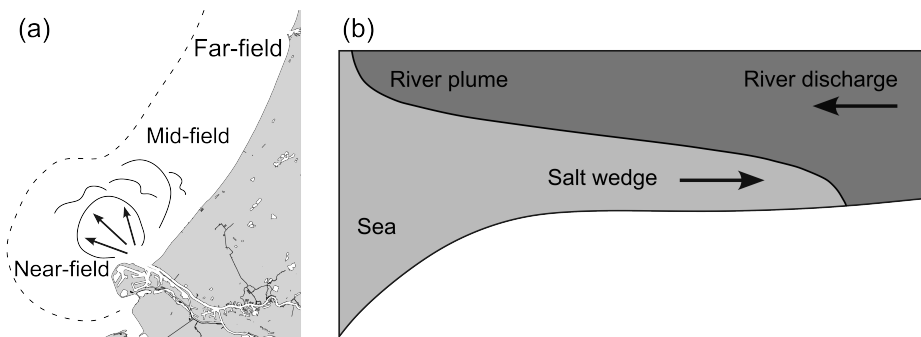


**Figure 1.1:** (a) Schematic of the Dutch coast, indicating the different dynamic regions of the river plume, adapted from Rijsburger (2021). (b) Schematic of the cross-section of the plume and estuary.

### 1.2.2 Mixing in estuaries

Vertical mixing in estuaries is highly variable and responds dynamically to tidal phase, river discharge, and stratification. Field observations have shown that mixing generally increases during spring tides and decreases during neaps (Geyer et al., 2000; Giddings et al., 2011), while strong river discharge enhances stratification, thereby reducing turbulence (Monismith et al., 2002). Intratidal variability of vertical mixing is also important in many estuaries, for example, stratification-induced turbulence suppression during flood tide and increased mixing during ebb have been documented in multiple systems, including the Rotterdam Waterway (de Nijs et al., 2011; MacDonald and Horner-Devine, 2008; Spicer and Huguenard, 2020).

Capturing these dynamics is essential for accurate modelling of salt intrusion. While high-resolution numerical models can capture many of these complexities, their accuracy hinges on the proper representation of vertical mixing. Most idealised models assume a constant vertical diffusivity, while more sophisticated models rely on turbulence closure schemes like  $k-\varepsilon$  or Mellor–Yamada 2.5 (Jones and Launder, 1972; Mellor and Yamada, 1982). However, the vertical mixing parameterisations, particularly those involving bottom friction or interfacial shear, are often poorly constrained due to the difficulty of acquiring field observations (Geyer and Smith, 1987; Tedford et al., 2009; Giddings et al., 2011).

The parameterisation of vertical mixing is commonly based on the gradient Richardson number ( $Ri$ ), which expresses the energy balance between potential energy and kinetic energy. While  $Ri$ -based formulations have been developed for oceanic vertical mixing (Pacanowski and Philander, 1981; Large et al., 1994), their application to estuaries remains uncertain due to stronger bottom-generated turbulence and sharper density gradients. Several estuary-specific modifications have been proposed (Lehfeltdt and Bloss, 1988; Park and Kuo, 1993), and some studies evaluated those parameterisations against observations.

For example, Nunes Vaz and Simpson (1994) compared multiple turbulence closure schemes for predicting stratification and compared those to observations, and demonstrated that the choice of parameterisation substantially affects the simulated temporal evolution of estuarine stratification. Among the tested schemes, the closure of Pacanowski and Philander (1981) provided the best overall qualitative and quantitative agreement with observations, although it systematically underestimated stratification intensity. In contrast, de Nijs and Pietrzak (2012) found in the Rotterdam Waterway that the classical formulation of Munk and Anderson (1948) provided the best agreement with observations, whereas other parameterisations failed to reproduce the observed turbulence dynamics. Recognising the importance of three-dimensional estuarine dynamics, Basdurak et al. (2017) extended existing  $Ri$ -based parameterisations by introducing a lateral fit to account for the influence of lateral circulation, relevant in wide estuaries. This approach successfully captured the observed lateral variability in eddy viscosity across a broad range of  $Ri$  values. Nevertheless, systematic statistical evaluations

of turbulence parameterisations against observed diffusivity remain scarce. Such assessments are needed to constrain the skill and regime dependence of commonly used parameterisations in estuarine modelling.

### 1.2.3 Subtidal response

While intratidal dynamics govern short-term variability in estuaries, longer-term trends in salt intrusion are driven by subtidal responses to external forcing. The salinity distribution in estuaries reflects a dynamic balance between seaward salt transport by river discharge and landward salt transport due to baroclinic exchange flows and tidal dispersion processes (Hansen and Rattray, 1965; Chatwin, 1976; MacCready, 2004). Understanding the relative contributions of these mechanisms and how they respond to external forcing, such as river discharge, winds, and the spring-neap tidal cycle, is critical for predicting salt intrusion length. Subtidal analyses, which average out high-frequency tidal variability, offer a valuable approach to isolating the effects of these more slowly varying forcings (Jay, 2010).

River discharge plays a primary role in modulating salt intrusion. Numerous studies show that the salt intrusion length decreases with increasing discharge for most estuaries and that the sensitivity of this relationship intensifies during periods of high flow (Abood, 1974; Ralston et al., 2010; Cook et al., 2023). Estuarine response time—how quickly salinity adjusts to changes in forcing—varies seasonally with discharge, and affects whether an estuary can respond to the spring-neap cycle. During drought conditions, response times may exceed the spring-neap period, making salt intrusion largely insensitive to tidal variability, as observed in the Hudson River (Bowen and Geyer, 2003; Lerczak et al., 2009).

In addition to discharge and tides, wind forcing significantly affects subtidal salinity dynamics. Wind-driven water level variations can alter the barotropic pressure gradient between the ocean and estuary, leading to wind-induced volume fluxes of similar magnitude to river runoff. These fluxes modify salinity distributions throughout the estuary (Wong and Valle-Levinson, 2002; Ralston et al., 2008; de Nijs et al., 2008; Li and Li, 2011; Zhu et al., 2020; Cook et al., 2023; Gerritsma et al., 2025).

Whether an estuary responds to subtidal variability in forcing depends on the relationship between the response time and the timescale of the forcing. In idealised systems under constant forcing, the response time represents the adjustment period required for the salinity structure to attain a new steady state following a perturbation. In real estuaries, however, forcing varies continuously, and the response time represents the timescale over which the system approaches a quasi-equilibrium following a change in boundary conditions. Theoretical estimates of this adjustment timescale scale with the ratio of salt intrusion length to the characteristic estuarine velocity,  $T_{\text{adj}} \sim L_s/\bar{u}$ , with proportionality factors depending on the dominant dynamics (MacCready, 2007). Observational studies suggest that actual response times can exceed these theoretical estimates (Lerczak et al., 2009).

### 1.2.4 Offshore forcing and plume dynamics

Subtidal variability of salt intrusion is not only shaped by river discharge and local winds but also by shelf processes and returning plume waters from the same estuary. Wind-driven upwelling and downwelling can modify ocean salinity and stratification, thereby impacting exchange flow.

For example, studies in Willapa Bay and the Columbia River estuary showed that wind-driven upwelling and downwelling affect horizontal density gradients and salt intrusion through changes in ocean salinity and stratification (Hickey et al., 2002; Chawla et al., 2008; Brasseale and MacCready, 2025). Giddings and MacCready (2017) showed that upwelling enhances, while downwelling suppresses or reverses estuarine exchange flow by altering baroclinic and barotropic pressure gradients. Geraeds et al. (2025) found the same relation between along-shore winds and exchange flow in the Rhine–Meuse Delta. Alongshore winds can influence plume structure through cross-shore Ekman transport, which affects estuarine salinity. For example, under downwelling-favourable conditions, the Columbia River plume is driven onto the shelf, potentially recirculating low-salinity water into nearby estuaries (Fong and Geyer, 2001; Lentz, 2004; Whitney and Garvine, 2005; Hickey and Banas, 2003). Such a buoyant coastal current may form a salt plug, inducing inverse inlet circulation and increasing estuarine flushing times (Juarez et al., 2020, 2022).

### 1.2.5 Estuary-Plume connection

Estuarine mixing has been shown to be important for determining the near-field plume salinity (Nash et al., 2009), which highlights the dynamic connectivity between plumes and estuaries. For the reverse problem, where inflowing saline waters are at depth, we hypothesise that plume mixing influences the inflow salinity. Following this line of reasoning, the near-field plume region can be regarded as a seaward boundary condition for the estuarine system.

The near-field plume region is characterised by jet-like plume expansion, with intense mixing (Horner-Devine et al., 2015). Characteristic here is that the entrainment velocity is consistently positive, meaning that saltwater tends to be entrained into the near-field plume, rather than freshwater being detrained and mixed down (MacDonald and Geyer, 2004; McCabe et al., 2009).

Furthermore, particle pathways investigated by Brasseale and MacCready (2021) showed that particles released in the plume can recirculate and make their way back into the estuary. Particles are able to travel away from the mouth in the plume, mix down into the lower layer, and can be transported back into the estuary at depth.

The studies discussed above support a tightly coupled estuary–plume system. To further explore this coupling, in the next section, the case study is introduced: the Rhine-Meuse Delta and its associated river plume.

### 1.3 Case study: Rhine-Meuse Delta

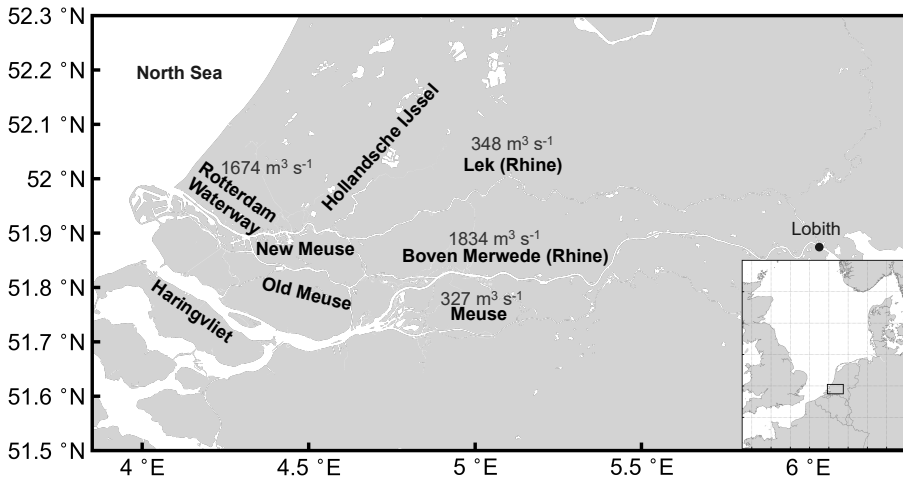


**Figure 1.2:** Map of the Rhine-Meuse Delta, indicating its location within the Netherlands, the relevant branches, the North Sea, and Lobith.

#### 1.3.1 Rhine-Meuse Delta estuary

The Rhine and Meuse River waters are carried towards the North Sea through the Rhine-Meuse Delta, a complex, multichannel estuarine system in the Netherlands. The only permanently open connection between the rivers and the sea is through the Rotterdam Waterway (Fig. 1.2), which forms the main outflow channel. Upstream of the Rotterdam Waterway, the flow is supplied by three major branches: the Lek and Beneden Merwede (Rhine), and the Meuse. The Rhine River enters the Netherlands at Lobith, and is there split into two branches.

Average annual discharges are  $348 \text{ m}^3 \text{ s}^{-1}$  through the Lek,  $1834 \text{ m}^3 \text{ s}^{-1}$  through the Waal (boven Merwede), and  $327 \text{ m}^3 \text{ s}^{-1}$  through the Meuse (Cox et al., 2021). These values do not sum exactly to the discharge through the Rotterdam Waterway ( $1674 \text{ m}^3 \text{ s}^{-1}$ ), because the semi-enclosed Haringvliet occasionally discharges water when the Haringvliet gates are open. However, during drought conditions, these gates typically remain closed.

The Dutch Rhine-Meuse Delta is a heavily engineered and urbanised multi-channel estuary with complex bathymetry, tidal phase differences, and a complicated, human-controlled discharge distribution. Such systems differ substantially from single-channel estuaries, as they introduce additional mechanisms such as tidal trapping, inter-channel exchange flows, and local reversals in salinity gradients at junctions. These mechanisms can enhance tidal dispersion and subtidal flow convergence (Stacey et al., 2001; MacVean and Stacey, 2011; Conroy et al.,

2020; Garcia et al., 2022). Different branches may also exhibit distinct responses to forcing, depending on their mixing regimes and stratification, as shown in studies of the Mekong Delta (Eslami et al., 2021a).

The Rotterdam Waterway has previously been classified as a salt wedge estuary (de Nijs et al., 2011; Niesten et al., 2024), characterised by a strong gradient between nearly freshwater and seawater, where the inland extent of saltwater has the shape of a wedge (Geyer and Ralston, 2011). However, the estuarine dynamics and classification of the upstream branches of the RMD have not previously been described in this context, due to a lack of observations during drought conditions.

The Rhine-Meuse Delta is densely populated and intensively used for agriculture and industry. The most downstream section of the estuary, the Rotterdam Waterway, is the approach channel to Europe's largest harbour (Port of Rotterdam), which undergoes regular dredging for shipping. Due to its industrial nature and high population density, it is extensively managed by the government and regional water boards to ensure an adequate freshwater distribution for all stakeholders.

### 1.3.2 Rhine River plume

The Rhine River plume is formed when the Rhine and Meuse waters discharge into the North Sea. This is a shallow shelf sea, where bottom friction and tides are important (Simpson, 1997). Unlike deeper systems such as the Columbia River plume, surface and bottom layers are dynamically coupled, making it ideal for studying plume–estuary interactions.

Studies on the Rhine River plume are in line with the expected response to wind forcing: downwelling-favourable winds thicken and trap the plume against the coast, while upwelling-favourable winds thin and detach it (Fong and Geyer, 2001; Keyzer, 2025). These winds also affect the alongshore speed of tidal plume fronts, aligned with the wind direction (Rijnsburger et al., 2018).

The dominant intratidal pattern in the mid-field and far-field of the Rhine River plume is characterised by alternating patterns of stratification and mixing over a tidal cycle, referred to as Strain-Induced Periodic Stratification (Simpson et al., 1990; Visser et al., 1994; Simpson and Souza, 1995). This leads to counter-rotating tidal ellipses for stratified plume conditions, but they disappear during well-mixed spring tide conditions (Souza and Simpson, 1996; de Boer et al., 2006).

## 1.4 Knowledge gaps

Salt intrusion poses a growing global threat to estuarine and deltaic systems, exacerbated by the consequences of climate change, such as sea-level rise and prolonged droughts. Understanding the physical processes that govern salt intrusion under such extreme conditions is crucial for the sustainable management of freshwater resources in low-lying coastal areas. In particular, delta systems like the Rhine-Meuse Delta (RMD) present additional challenges due to their complex morphology, multiple branches, and engineered structures. Despite decades of estuarine research, several knowledge gaps remain:

### **Scarcity of observations of turbulence in salt wedge estuaries**

Turbulence and vertical mixing play a central role in controlling the salinity structure of estuaries, yet the processes governing turbulence in the strongly stratified RMD are still not well constrained by observations. Also, simple parameterisations are crucial for idealised models, and so far, have mainly been developed for the coastal ocean. While several estuary-specific parameterisations have been tested, systematic statistical evaluations of turbulence parameterisations against observed diffusivity remain scarce. Such assessments are needed to constrain the skill and regime dependence of Richardson-number-based parameterisations in estuarine modelling.

### **Limited observational understanding of salt intrusion during drought in branching delta systems**

The response of salt intrusion to the complex interplay of river discharge, wind, and tidal forcing has not been extensively studied in branching delta systems. This gap is largely due to the scarcity of high-resolution, spatially extensive observations under extreme conditions such as droughts.

### **Limited insight into the downstream estuary boundary condition**

While much research has focused on the fate of riverine freshwater in the coastal ocean, the reverse process of saline water intruding from the coastal sea into estuaries has received comparatively little attention. However, growing evidence suggests that the river plume, a dynamic boundary condition at the downstream end of the estuary, can significantly influence estuarine dynamics. The origin, transport pathways, and mixing history of intruding salt water remain poorly understood, especially in shallow shelf seas like the North Sea.

## 1.5 Research Objectives and Questions

The overarching aim of this thesis is to increase our understanding of salt intrusion dynamics in a branching delta system (the Rhine-Meuse Delta), particularly during drought conditions, which are the most relevant conditions for salt intrusion. To achieve this, the following research questions are formulated:

1. **How is vertical mixing and turbulence characterised in the Rhine-Meuse Delta estuary, and can we capture this in simple Richardson-number-based parameterisations?** (Chapter 2)

The relationship between flow, density, and turbulence is examined through qualitative comparisons against microstructure measurements, and Richardson-number-based diffusivity parameterisations are quantitatively evaluated using statistical metrics. Parts of this chapter are under review for publication in the *Journal of Coastal Research* as:

**Wegman, T. M., Biemond, B., Piccolroaz, S., Horner-Devine, A. R., Dijkstra, H. A., & Pietrzak, J. D.** (in review). Direct observations of turbulence in a salt wedge estuary. *Journal of Coastal Research*.

2. **What drives salt intrusion length variations in the Rhine-Meuse Delta during a period of exceptional drought?** (Chapter 3)

This chapter examines the main drivers of salt intrusion in the RMD during the historic 2022 drought, based on extensive salinity, discharge, water level, and wind observations. Differences between the main estuary and its side branches are also explored. This chapter has been published in *Journal of Geophysical Research: Oceans*:

**Wegman, T. M., Pietrzak, J. D., Horner-Devine, A. R., Dijkstra, H. A., & Ralston, D. K.** (2024). Observations of estuarine salt intrusion dynamics during a prolonged drought event in the Rhine-Meuse Delta. *Journal of Geophysical Research: Oceans*, 129, e2024JC021655.

3. **What determines the source conditions for estuarine inflow?** (Chapter 4)

This chapter investigates how wind and tidal forcing influence flow and salinity near the river mouth, thereby modulating the dynamic boundary condition for estuarine salt intrusion. This problem is addressed using moored field observations of salinity and flow in the near-field Rhine River plume and the Rhine-Meuse Delta estuary, with a particular focus on a severe drought event. This chapter is being prepared for submission as:

**Wegman, T. M., Pietrzak, J. D., Horner-Devine, A. R., Ralston, D. K., & Kranenburg, W. M.** (in preparation). Influences of tides and winds on estuarine inflow conditions.



# 2

## Direct observations of turbulence in a salt wedge estuary

### Key Points

- A dataset of vertical mixing observations in a salt wedge estuary is presented.
- The salt wedge remains stable throughout the tidal cycle.
- $Ri$ -based parameterisations capture the statistical properties of vertical mixing.

---

Parts of this chapter are under review for publication in the Journal of Coastal Research as: Wegman, T. M., Biemond, B., Piccolroaz, S., Horner-Devine, A. R., Dijkstra, H. A., & Pietrzak, J. D. (in review). Direct observations of turbulence in a salt wedge estuary. *Journal of Coastal Research*.

The measurement data is available in the repository of 4TU.ResearchData, with doi:10.4121/bcf32f81-291a-4d60-be5e-90a92ca37aa1.

## Abstract

2

Salt intrusion is a pressing problem in many estuaries around the world, in particular due to climate change. The characterisation of vertical mixing is important to understand the salinity structure of estuaries, but direct observational data is scarce. Here, we present a novel observational dataset containing salinity, flow, and direct turbulence measurements spanning multiple phases of two tidal cycles under two different tidal and river discharge conditions, in the Rotterdam Waterway, a salt wedge estuary in the Netherlands. The patterns of turbulent diffusivity, velocity shear, and stratification show that the gradient Richardson number is often a good measure of vertical mixing in this estuary. This is supported by the performances of four gradient Richardson number-based parameterisations of vertical mixing when evaluated for this dataset. The statistical behaviour of vertical mixing is, after calibration, well captured by the Pacanowski and Philander (1981) parameterisation. The other investigated parameterisations fail to reproduce the largest values of the vertical mixing.

## 2.1 Introduction

With the increasing probability of dry periods in a warming climate, salt intrusion is increasing in many coastal areas (Lee et al., 2024, 2025). This is a serious problem, particularly in the Rhine-Meuse Delta (RMD) in the Netherlands, where fresh water is used intensively for industry, drinking purposes, and agriculture. During summer droughts, a shift of a few kilometres in the extent of salt intrusion in this region can have substantial consequences for its livability. To ensure freshwater resources now and in the future, it is essential to have a detailed understanding of the physical mechanisms that drive the salt-intrusion dynamics. These mechanisms include longitudinal and lateral advection, as well as vertical and horizontal turbulent diffusion of salt. The strength of vertical mixing determines the exchange of momentum and salinity across the pycnocline, thereby influencing the vertical and longitudinal salinity structure.

Modelling efforts are essential for the understanding and prediction of salt intrusion properties in estuaries; a hierarchy of models is available for this purpose. One of the weaker aspects in all these models is the representation of the vertical mixing, usually expressed by the vertical turbulent eddy viscosity and eddy diffusivity. In many idealised models (MacCready, 2004; Dijkstra and Schutteleaars, 2021), the vertical eddy diffusivity is taken constant in the entire domain. More detailed numerical models usually implement second-order turbulence closures like  $k-\varepsilon$  (Jones and Launder, 1972; Umlauf and Burchard, 2003) or Mellor-Yamada 2.5 (Mellor and Yamada, 1982). Often bottom friction, which is an important source of vertical shear in most estuaries (Bowden, 1981; Geyer et al., 2000) is used as a calibration parameter (Ralston et al., 2017; Matte et al., 2017; Zhu et al., 2021; Mohammadian et al., 2022), after which the performance of the model is evaluated in terms of reproducing the mean currents and salinity. Besides bottom-generated turbulence, interfacial shear contributes to turbulence in strongly stratified estuaries (Geyer and Smith, 1987; Tedford et al., 2009; Giddings et al., 2011). However, a validation of these mixing representations with field data is rarely carried out as such observations are time-consuming, challenging, and expensive.

Field observations in estuaries show that turbulence levels are highly variable in time and space, mainly due to varying forcing of tides and river discharge. Vertical mixing generally increases during spring tides and decreases during neap tides (Geyer et al., 2000; Giddings et al., 2011). Furthermore, increased river discharge can increase the stratification and thereby reduce turbulence levels (Monismith et al., 2002).

Due to baroclinic tidal asymmetry (Jay and Musiak, 1996), many estuaries also showed intratidal variability of vertical mixing (e.g., de Nijs et al., 2011; MacDonald and Horner-Devine, 2008; Giddings et al., 2011; Spicer and Huguenard, 2020). Microstructure observations by Spicer and Huguenard (2020) showed that bottom-generated turbulence is larger during ebb than during flood tide, due to the increased turbulence damping induced by stratification during flood tide. In

strongly stratified estuaries, observations of mid-depth flood velocity maxima around the pycnocline have been associated with the combination of turbulence suppression at the pycnocline and increasing baroclinic pressure gradients over depth (Geyer and Farmer, 1989; Chant et al., 2007; de Nijs et al., 2011). de Nijs et al. (2011) showed that in the Rotterdam Waterway, these flow features lead to an increase in upstream advection of saline waters toward regions of lower salinity and momentum. Other studies showed the importance of interfacial mixing (e.g., Geyer and Smith, 1987; Tedford et al., 2009; Holleman et al., 2016), which becomes largest on the ebb tide, when tidal straining produces maximum shear at the pycnocline (MacDonald and Horner-Devine, 2008; Giddings et al., 2011).

In idealised models, a relationship between vertical mixing and the mean flow field and stratification is needed, and this can be deduced from the observed turbulence using the gradient Richardson number  $Ri$  (Equation 2.3), which is the ratio between potential energy and kinetic energy. For instance, Peters (1999) observed that variability of vertical mixing in the Hudson River estuary correlated well with variations in  $Ri$ , whereas correlation with river discharge was weak. For the ocean, relatively simple  $Ri$ -based parameterisations of vertical diffusivity ( $K_v$ ) have been proposed (Munk and Anderson, 1948; Pacanowski and Philander, 1981; Large et al., 1994). These parameterisations contain information about the functional dependence and scaling relationships between vertical density gradients, shear, and diffusivity. However, their validity is not guaranteed in estuaries, as typical values of velocities and density gradients in these environments exceed those in the ocean, and bottom-friction-generated turbulence is stronger. For example, Simpson et al. (2005) found that these functional relationships between  $Ri$  and vertical diffusivity show only a limited degree of agreement with observations in the York River. Despite these limitations, the functional relationships are being used in models of estuaries (Liu et al., 2002; Huijts et al., 2006; Dijkstra et al., 2022). Refined versions of these formulations for estuaries, which additionally consider the water depth (Lehfeldt and Bloss, 1988; Park and Kuo, 1993) and lateral effects (Basdurak et al., 2017) have been proposed. Nunes Vaz and Simpson (1994) compared multiple turbulence closure schemes for predicting stratification and compared those to observations, and demonstrated that the choice of parameterisation substantially affects the simulated temporal evolution of estuarine stratification. Among the tested schemes, the closure of Pacanowski and Philander (1981) provided the best overall qualitative and quantitative agreement with observations, although it systematically underestimated stratification intensity. A field study in a large harbour basin of the Rotterdam Waterway, directly measuring near-bottom turbulence (de Nijs and Pietrzak, 2012), interestingly showed the best agreement for Munk and Anderson (1948), while the Pacanowski and Philander (1981) and Lehfeldt and Bloss (1988) parameterisations did not give a good agreement. The de Nijs and Pietrzak (2012) study showed the importance of buoyancy forces, which can result in countergradient buoyancy fluxes, which is not considered in these parameterisations, and was previously described by Gerz and Schumann (1996).

The goal of this chapter is to find the relation between observed turbulence and flow and density. We use a combination of qualitative comparisons and quantitative analyses based on gradient Richardson number-based parameterisations of vertical eddy diffusivity. To characterise the stratified turbulence throughout the tidal cycle and evaluate representations of vertical mixing, we present and analyse microstructure measurements in the Rotterdam Waterway.

The remainder of this chapter is structured as follows. Section 2.2 provides the theoretical background. In section 2.3, the study site, measurements, and the environmental background conditions are described. Section 2.4 qualitatively describes the observations on flow properties, stratification, and turbulence quantities over multiple phases of two tidal cycles in the Rotterdam Waterway under two different background conditions. In addition, a quantification of the performance of Richardson number-based parameterisations of vertical diffusivity is carried out with a statistical method. Section 2.5 provides a discussion of the results, and section 2.6 presents the conclusions.

## 2.2 Theoretical background

Here we introduce the relevant variables in the analysis, to quantify stratification, velocity shear and vertical mixing. Moreover, we present the parameterisations which are considered in our analysis.

### 2.2.1 Shear, stratification and stability

To quantify stratification, we use the buoyancy frequency  $N$ , which is defined as

$$N = \sqrt{-\frac{g}{\rho_0} \frac{\partial \rho}{\partial z}}, \quad (2.1)$$

where  $g = 9.81 \text{ m s}^{-2}$  is the gravitational acceleration,  $\rho_0 = 1000 \text{ kg m}^{-3}$  is reference density,  $\rho$  is water density and  $z$  is the vertical coordinate. Here,  $z = 0$  indicates the water surface and  $z = -H$  is the bottom, where  $H$  is the local water depth, so  $z$  is defined positive upwards.

Vertical velocity shear  $S$  can be calculated from the two horizontal velocity components  $u$  and  $v$ , i.e.,

$$S^2 = \left( \frac{\partial u}{\partial z} \right)^2 + \left( \frac{\partial v}{\partial z} \right)^2. \quad (2.2)$$

The ratio between potential energy and kinetic energy in a flow is the gradient

Richardson number, which is defined as

$$Ri = \frac{-g \frac{\partial \rho}{\partial z}}{\rho \left( \frac{\partial u}{\partial z} \right)^2} = \frac{N^2}{S^2}. \quad (2.3)$$

$Ri$  indicates the static stability of the fluid (Miles, 1961), where  $Ri > 0.25$  is generally accepted as a threshold value for stability. The vertical diffusivity  $K_v$  can be estimated with the Osborn relation (Osborn, 1980)

$$K_v = \Gamma \frac{\varepsilon}{N^2}, \quad (2.4)$$

where  $\varepsilon$  is the turbulent kinetic energy (TKE) dissipation rate and  $\Gamma$  is the mixing efficiency parameter and describes how effectively the TKE dissipation ( $\varepsilon$ ) contributes to vertical mixing. We set  $\Gamma = 0.2$ , which is considered to be a fair approximation of the long-term average, but it is important to keep in mind that evidence exists that this value differs for individual observations (Holleman et al., 2016).

## 2.2.2 Parameterisations

We consider four existing parameterisations that quantify the relationship between  $Ri$  and  $K_v$ , described by

1. Munk and Anderson (1948) (MA):

$$K_v = c_1 \left( 1 + \frac{10}{3} Ri \right)^{-\frac{3}{2}}; \quad (2.5)$$

2. Pacanowski and Philander (1981) (PP):

$$K_v = A_v (1 + 5Ri)^{-1} + c_2, \quad \text{where} \quad A_v = c_3 (1 + 5Ri)^{-2} + c_4; \quad (2.6)$$

3. Lehfeldt and Bloss (1988) (LB):

$$K_v = c_5 z^2 \left( 1 + \frac{z}{H} \right)^2 \left| \frac{\partial u}{\partial z} \right| (1 + 3Ri)^{-3}; \quad (2.7)$$

4. Park and Kuo (1993) (PK):

$$K_v = c_6 z^2 \left( 1 + \frac{z}{H} \right)^2 \left| \frac{\partial u}{\partial z} \right| (1 + c_7 Ri)^{-\frac{3}{2}}. \quad (2.8)$$

Here, the coefficients  $c_1$ – $c_7$  represent calibration parameters for the respective parameterisations. Each of these parameterisations consists of a shape function of the form  $(1 + \alpha_1 Ri)^{-\alpha_2}$ , where  $\alpha_1$  and  $\alpha_2$  are positive constants. This shape

function is multiplied by the value that  $K_v$  would attain without suppression by stratification (i.e.  $Ri = 0$ ). For MA and PP this value is constant, while for LB and PK, it depends on the dimensionless depth ( $z/H$ ) through the formulation introduced by Rossby and Montgomery (1935).

## 2.3 Observations and analysis

### 2.3.1 Study site and instruments

The Rotterdam Waterway, in the Dutch Rhine-Meuse Delta (Fig. 2.1), is a dynamic salt wedge estuary with a semi-diurnal tide and a range of approximately 2.0 m during spring tide and 1.2 m during neap tide (de Nijs et al., 2011).

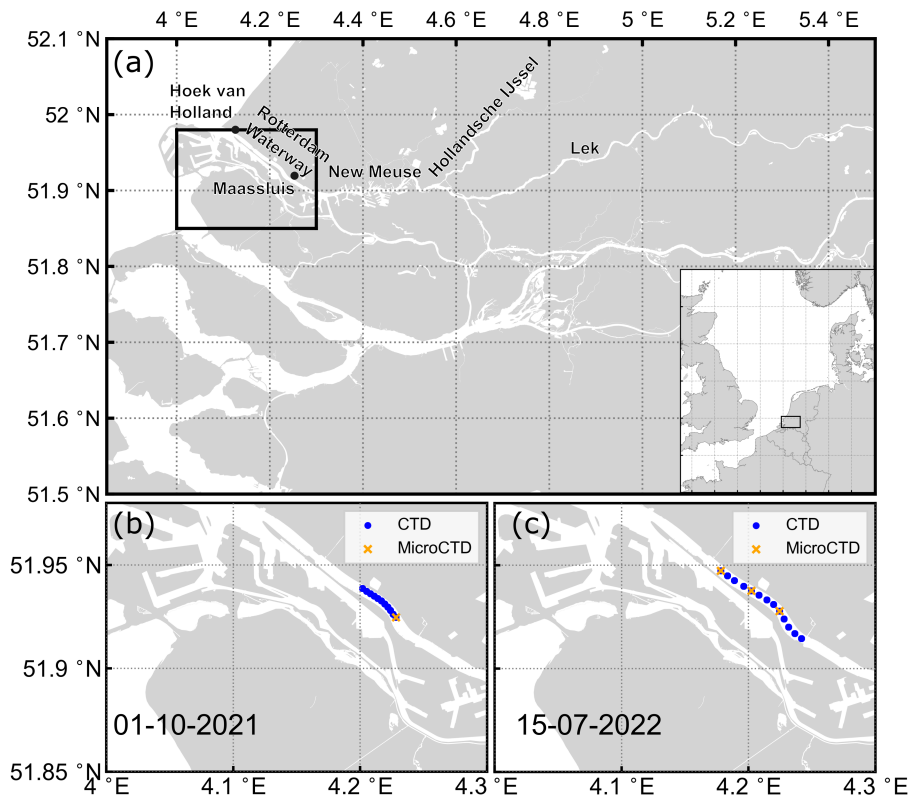


**Figure 2.1:** (a) Map of the Rotterdam Waterway and location of the Netherlands. (b) Locations of the measurements on the 1<sup>st</sup> of October 2021. (c) Locations of the measurements on the 15<sup>th</sup> of July 2022. The CTD measurements are indicated with blue dots and the MicroCTD measurements with yellow crosses.

Measurements were performed in the Rotterdam Waterway on two days with

contrasting environmental conditions. On 1<sup>st</sup> October 2021 it was a neap tide, and the Rhine River discharge was approximately  $1290 \text{ m}^3 \text{ s}^{-1}$ ; winds were moderate ( $9 \text{ m s}^{-1}$ ) from alongshore (downwelling-favourable) direction. The total survey captured a full tidal cycle but the turbulence measurements were taken during the flood tide, through slack, and during most of the ebb tide. It was a spring tide on 15<sup>th</sup> July 2022 and the Rhine River discharge was approximately  $1020 \text{ m}^3 \text{ s}^{-1}$ , winds were moderate ( $5 \text{ m s}^{-1}$ ) and directed onshore. The total duration of the survey was 8 hours and captured the ebb tide and the onset of flood.

The water levels at the nearest tide gauge station (Maassluis) during the surveys are shown in Figure 2.2. During the October 2021 survey, there was a small coastal set-up of roughly 0.2 metres, following the difference between the astronomical tide and the measured water level at Maassluis (Fig. 2.2a). During the survey of July 2022, the coastal set-up was negligible (Fig. 2.2b). The city of Hoek van Holland is the reference location for the estuary mouth.

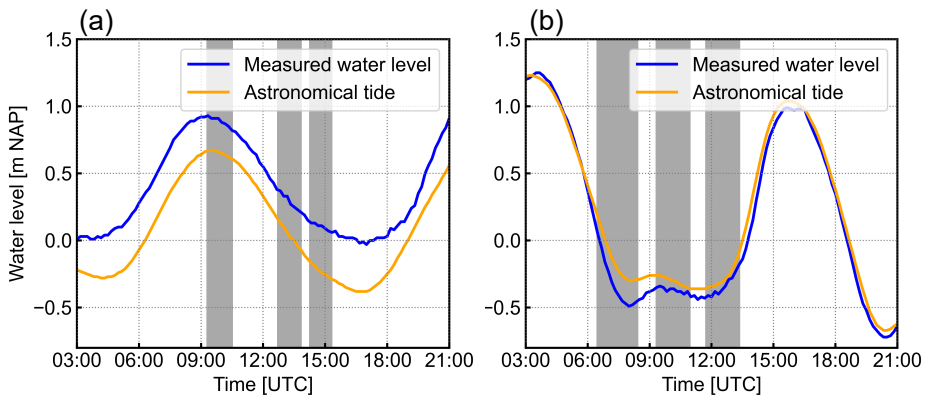


**Figure 2.2:** Water level (metres above Normaal Amsterdams Peil (NAP)) at the tide gauge station closest to the location of the ship survey (Maassluis, shown in Figure 2.1). The blue line corresponds to the measured water level and the orange line to the astronomical tide. (a) On October 1, 2021, (b) on July 15, 2022. The grey shading indicates the time intervals of the analysed transects.

During both ship surveys we took measurements of flow velocity, density and turbulence. Velocity measurements were collected using a ship-mounted Broadband 614.4 kHz Acoustic Doppler Current Profiler (ADCP). The sampling frequency was 1 Hz, and the vertical bin size was 50 cm. The velocity measurements were taken continuously. At all measurement stations, we took regular conductivity, temperature, depth (CTD) measurements. During the survey of October 2021 we used a Siltprofiler to take CTD measurements. The Siltprofiler was developed by Deltares in collaboration with Ravensrodd Consultants, Ltd. A Valeport SWiFT Sound Velocity Profiler was used on the survey of July 2022. The instrument directly measures temperature, pressure, and sound velocity at a frequency

of 32 Hz. Conductivity, salinity, and density are calculated using Valeport's proprietary algorithm (Allen et al., 2017). In the rest of the manuscript, we refer to this instrument as a CTD as well.

Microstructure profiles were collected using a free-falling MicroCTD, developed by Rockland Scientific. The MicroCTD measures turbulence properties with two microstructure velocity airfoil shear probes and two fast thermistor sensors (type FP07), all sampling at a high frequency of 512 Hz. The two shear probes are positioned perpendicular to each other, to measure both components of the horizontal velocity shear fluctuations. The vertical positioning of the profiler is tracked with a pressure sensor, sampling at 64 Hz. The dynamics of the profiler flight are measured using a two-axis vibration sensor sampling at 512 Hz and a two-axis inclinometer sampling at 64 Hz. These measurements are applied during data processing to correct shear data for instrument-induced vibrations and, if necessary, to discard non-optimal profiles.

We sailed transects in the thalweg of the estuary to measure the along-channel characteristics, which we repeated throughout the tidal cycle. In 2021, the transect was 2.5 km long, with CTD profiles taken every 250 m, and a subset of MicroCTD profiles taken at the end of the transect (Fig. 2.1b). In 2022 the transects were 6 km long, with CTD profiles taken every 500 m and a subset of MicroCTD profiles taken every 2 km (yellow crosses in Figure 2.1c). Such a subset of MicroCTD profiles consisted of five to ten consecutive casts, which we used in the analysis to obtain robust turbulence statistics.

### 2.3.2 Data processing and analysis

ADCP velocity data of the lower 10% of the water column were removed to exclude the side-lobe effect. The velocity data were transformed to streamwise  $u$  and stream-normal  $v$  velocities through a principal component analysis. Five-minute intervals of velocity measurements were matched to the CTD and the MicroCTD casts based on time.

The CTD measurements were lowpass filtered using a Butterworth filter. The Thermodynamic Equation Of Seawater - 2010 (TEOS-10) was used to convert observations of temperature and conductivity into salinity and density.

Based on the density profile, the buoyancy frequency  $N$  was calculated using Equation 2.1. Velocity shear  $S$  was calculated based on the stream-wise  $u$  and stream-normal  $v$  ADCP velocities, with Equation 2.2. The vertical derivatives in both  $S^2$  and  $N^2$  were calculated using central differences, and on the edges forward and backward differences were used. For evaluation of the  $Ri$ -based parameterisations, density data of the MicroCTD was used, because this corresponds exactly to the location and time of the measurements of the vertical diffusivity. For all other analyses on the density, the CTD measurements were used. In addition, the velocity data were interpolated to the resolution of the density data. When computing  $Ri$ , the velocity profiles were smoothed using a Gaussian filter before calculating vertical gradients. This was done to prevent the occurrence of

large variations in  $Ri$  (note that  $Ri$  goes to infinity for  $S^2 \rightarrow 0$ , which commonly occurs for unsmoothed velocity data). Around the remaining local extremes in the velocity field, we used a lower bound of  $S^2 = 4 \cdot 10^{-4} \text{ s}^{-2}$  for the vertical velocity gradients. It was a posteriori confirmed that with this threshold for shear, the minimum values of  $K_v$  in the parameterisations were in the same range as the minimum observed  $K_v$ .

Turbulent kinetic energy dissipation rate  $\varepsilon$  was determined from velocity shear spectra measured with the MicroCTD, using the same methods presented in Piccolroaz et al. (2021). Data processing included the following steps. First, the raw microstructure shear profiles were cleaned by removing spikes (outliers mainly due to instrument collisions with suspended particles). Then, low-frequency noise caused by the motion of the free-falling profiler was removed by high-pass filtering with a cut-off wavenumber equal to half the instrument length. Each vertical cast was divided into 1.0 m long, 50% overlapping bins for which shear frequency spectra were derived by ensemble averaging the Fast Fourier Transform power spectra computed for 0.33 m and 50% subsegments, detrended and Hanning tapered. The shear frequency spectra were converted to the corresponding wavenumber spectra according to Taylor's frozen turbulence hypothesis and knowing the profiling velocity. Finally, the spectra were corrected for the spatial response of the probe and denoised using the information obtained from the piezo-accelerometers installed inside the instruments. The turbulent kinetic energy dissipation rate was calculated according to its definition for small-scale isotropic turbulence

$$\varepsilon = \frac{15}{2} \nu \left\langle \left( \frac{\partial u'}{\partial z} \right)^2 \right\rangle = \frac{15}{2} \nu \int_0^\infty \Psi_S(k) dk \quad (2.9)$$

where  $\nu$  is the kinematic viscosity of water and  $\partial u' / \partial z$  is the velocity shear fluctuation. To calculate  $\varepsilon$ , we integrated the measured spectrum between the inertial subrange and a suitably imposed upper bound, adding the fraction of the shear variance that is not resolved as explained in Piccolroaz et al. (2021). We refer the reader to this source for a complete explanation.

A bin was discarded when the mean absolute deviation ( $MAD$ ) between the reference Nasmyth spectrum and the measured spectrum, was larger than a critical value of  $MAD_c = 2(2/d)^{0.5}$ . This critical value is based on the degrees of freedom ( $d$ ) of the spectral estimate, depending on the spectral technique, window, and averaging methods used.

We note that we were operating in a highly dynamic environment, and we found many instances of  $\varepsilon > 10^{-7} \text{ m}^2 \text{ s}^{-3}$ , which is an upper limit for acceptable spectral fits when using the FP07 temperature sensors according to Piccolroaz et al. (2021), and confirmed by a preliminary analysis we performed on the temperature gradient spectra. For this reason, we have only used the shear probe data in this analysis and do not comment on the processing of the FP07 data. In 2021 we had 90% good bins for the shear sensors and in 2022 92%. In Figure A.1 of the

Supplementary Information we show the percentage of the rejected bins, based on the criteria described above.

### 2.3.3 Stochastic parameterisation calibration

To focus on the functional relationship between  $Ri$  and  $K_v$ , and not be obstructed by an unsuitable choice of coefficients, we calibrated constants  $c_1 - c_7$  in Equations 2.5-2.8 first. For the calibration, we grouped the values of  $K_v$  from observations and parameterisations based on their vertical coordinate in bins of 1 m. For each of these bins, we calculated the Kullback-Leibler divergence (Kullback and Leibler, 1951) (KLD), which is defined as

$$KLD = \sum_x P(x) \log \left( \frac{P(x)}{Q(x)} \right), \quad (2.10)$$

in which  $P(x)$  and  $Q(x)$  are the density distributions of observed and parameterised  $K_v$ , respectively. The KLD is a measure of statistical disagreement between two distributions and thus indicates the statistical difference between the observed and parameterised  $K_v$ . A value of 0 indicates that distributions are indistinguishable and the KLD increases for more different distributions. We then optimised the values of  $c_1 - c_7$  using a gradient descent algorithm to find the minimum KLD. Note that the properties of the KLD do not allow for defining a threshold for which the agreement between two distributions is considered good; see Cover and Thomas (2006) for a more extensive discussion on the characteristics of the KLD.

## 2.4 Results

### 2.4.1 The evolution of internal flow structure and turbulence

Due to the difference in forcing conditions, the estuary was more stratified during the 2021 survey than the 2022 survey. The Rhine-Meuse estuary generally has a stronger stratification on neap tides than on spring tides (Wegman et al., 2025). Additionally, higher discharges also stratify the estuary. We present our results below, following the characteristics of the observed flow and stratification patterns during the two surveys.

#### Stratified flood tide October 2021

During the flood tide in October 2021 (Fig. 2.3), the flow was characterised by a vertically sheared, unidirectional landward structure with a strong stratification. Flow velocities reached a maximum near the pycnocline situated around mid-depth (approximately 7–9 m depth; Figure 2.3a), forming a mid-depth jet (de Nijs et al., 2011).

The highest values of velocity shear  $S^2$  (Fig. 2.3c), ranging between 0.05 and  $0.06 \text{ s}^{-2}$ , were observed around the pycnocline and throughout the upper layer. The strongest stratification, indicated by  $N^2$  exceeding  $0.05 \text{ s}^{-2}$ , coincided with the velocity maximum (Fig. 2.3b), although elevated  $N^2$  was vertically more confined than the region of enhanced shear.

The enhanced shear in the upper layer arose from the vertical structure of the velocity profile, with velocities close to zero at the surface increasing with depth towards the pycnocline. This vertical shear reflected an increasing barotropic pressure gradient within the upper layer and was therefore internally generated, rather than driven by bottom friction.

The turbulence measurements in October 2021 were mainly limited to the upper layer of the water column. Due to constraints in operating the instrument in the dynamic Rotterdam Waterway with substantial shipping traffic, the instrument's deployment time and the depth range of the measurements were limited.

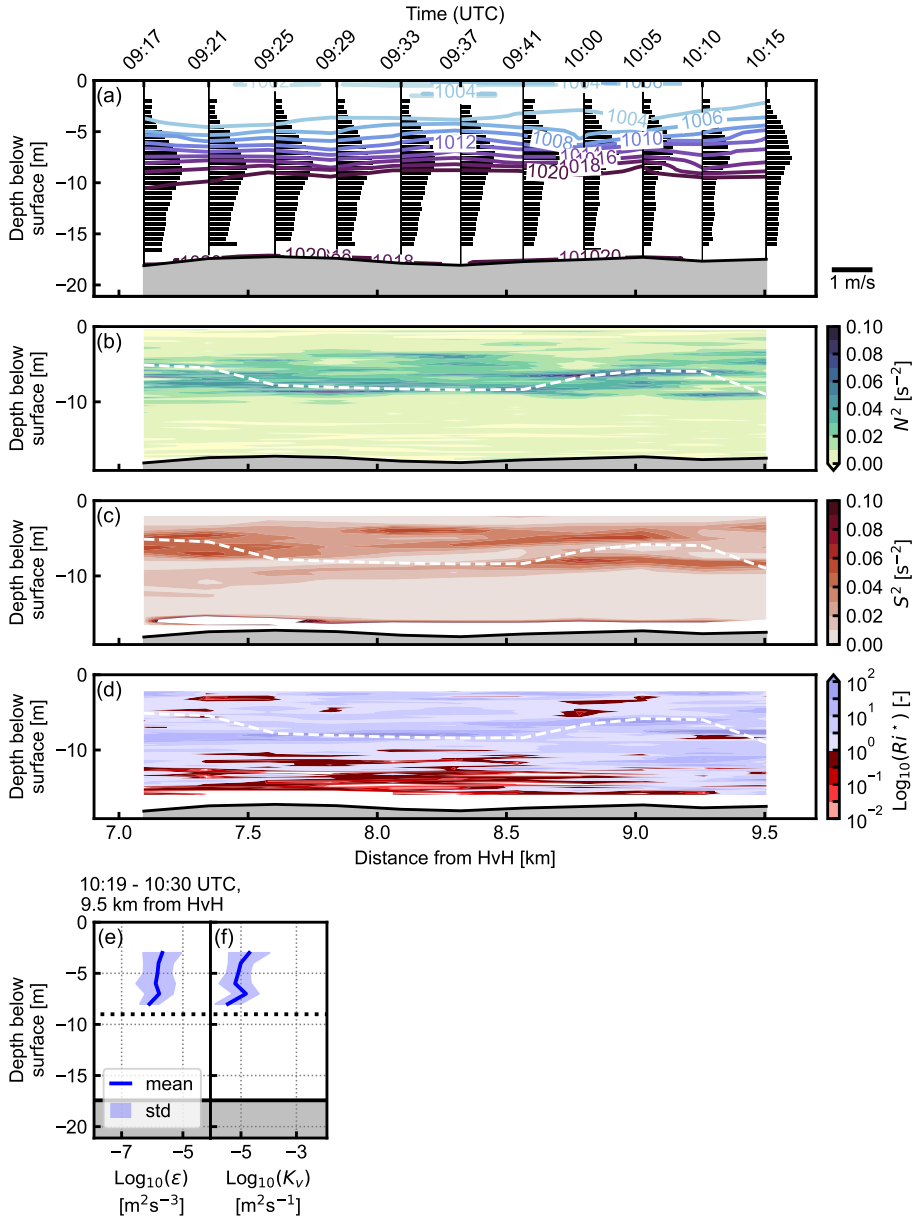
During the flood phase, the upper half of the water column (between 3 and 7 m) was characterised by values of  $\varepsilon$  and  $K_v$  of  $10^{-6} \text{ m}^2 \text{ s}^{-3}$  and  $10^{-5} \text{ m}^2 \text{ s}^{-1}$  (Fig. 2.3e-f), respectively, which were lower than the maximum values observed during ebb tide that day, described below.

Figure 2.3d shows that the water column from the surface down to about the pycnocline was mostly characterised by  $Ri > 1$ , signifying stability, despite the strong velocity shear around the pycnocline. This is because locations with high values of  $S^2$  generally align with places where  $N^2$  is also high (exceeding  $0.05 \text{ s}^{-2}$ ). Below the pycnocline, the well-mixed bottom layer contained regions with  $Ri < 0.25$ , suggesting the potential for turbulent mixing. Although direct turbulence observations were unavailable in this layer, the generally low values of  $N^2$  and  $S^2$  (below  $0.01 \text{ s}^{-2}$ ) imply weak turbulence and mixing.

### Stratified high water slack and ebb tide October 2021

During high water slack and the onset of ebb tide in October 2021, the flow structure changed substantially while stratification structure remained similar (Fig. 2.4). The flow was characterised by ebb flow in the upper half of the water column and a near-stationary lower layer (Fig. 2.4a). The strongest velocity shear (Fig. 2.4c), with values ranging between 0.05 and  $0.10 \text{ s}^{-2}$ , was still concentrated above the pycnocline, but there was less shear directly at the pycnocline itself than during ebb. At the onset of ebb tide the barotropic ebb flow opposed the baroclinic flow in the bottom layer, which resulted in a nearly-stationary bottom layer. In the upper layer the barotropic tide was aligned with the baroclinic flow, causing increasing ebb flow towards the surface, and a corresponding strong shear above the pycnocline.

Accordingly, the strongest turbulence and mixing were observed above the pycnocline, with values of  $\varepsilon$  and  $K_v$  reaching up to  $10^{-5} \text{ m}^2 \text{ s}^{-3}$  and  $10^{-4} \text{ m}^2 \text{ s}^{-1}$  at depths of 7 m (Fig. 2.4e, f). Around the pycnocline, these values decreased by one to two orders of magnitude as the stratification increased ( $N^2$  between



**Figure 2.3:** (a) Internal flow structure (along-channel velocity and density), (b) buoyancy frequency  $N^2$ , (c) velocity shear squared  $S^2$ , (d) dimensionless gradient Richardson number  $Ri^* = \frac{Ri}{0.25}$ , (e-f) MicroCTD profiles of TKE dissipation rates and diffusivity rate along the section between 9:17 and 10:15 UTC (flood tide), on October 1<sup>st</sup>, 2021. The white dashed line indicates the pycnocline depth, defined as the maximum gradient in  $N^2$ . The x-axis indicates kilometres from Hoek van Holland (sea side).

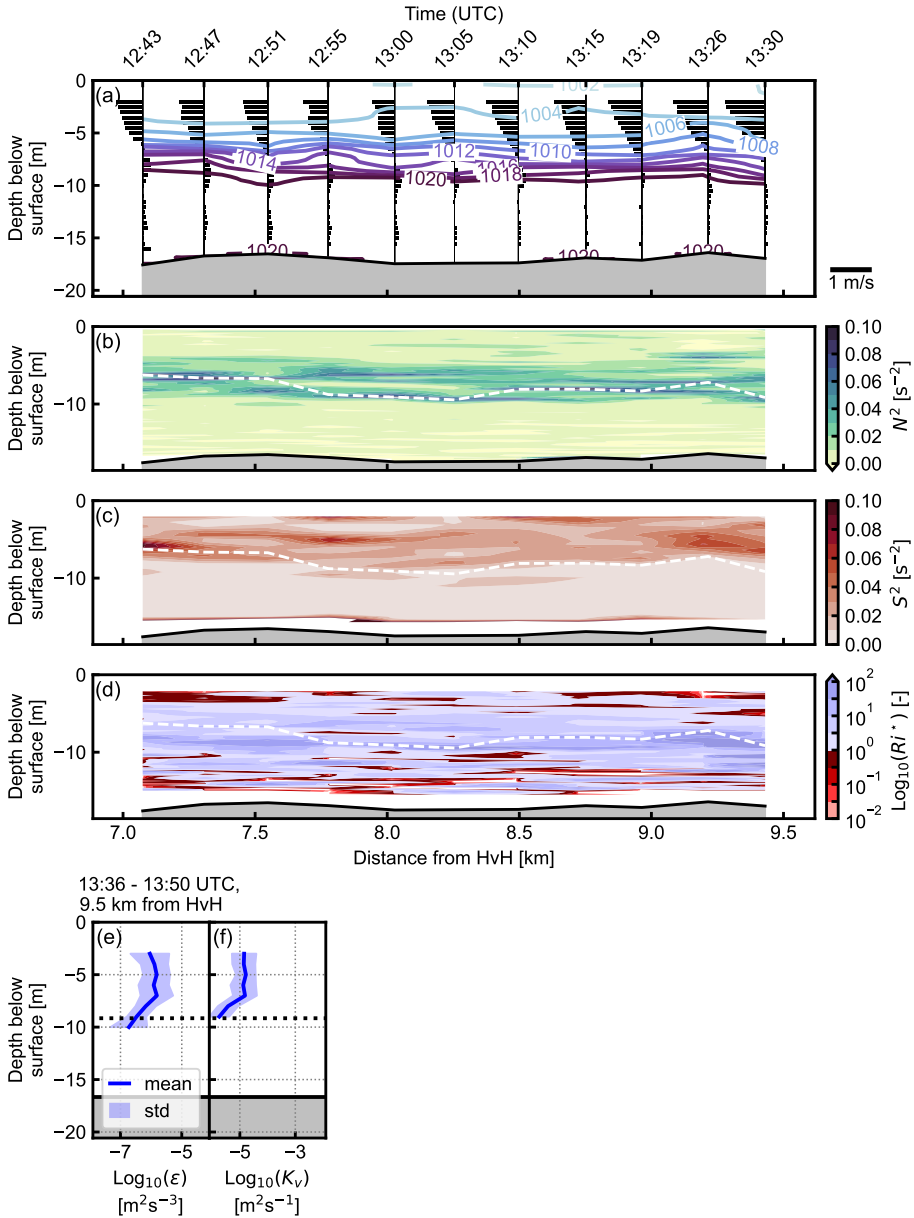


**Figure 2.4:** (a) Internal flow structure (along-channel velocity and density), (b) buoyancy frequency  $N^2$ , (c) velocity shear squared  $S^2$ , (d) dimensionless gradient Richardson number  $Ri^* = \frac{Ri}{0.25}$ , (e-f) MicroCTD profiles of TKE dissipation rates and diffusivity rate along the section between 12:43 and 13:30 UTC (beginning of ebb tide), on October 1<sup>st</sup>, 2021. The white dashed line indicates the pycnocline depth, defined as the maximum gradient in  $N^2$ . The x-axis indicates kilometres from Hoek van Holland (sea side).

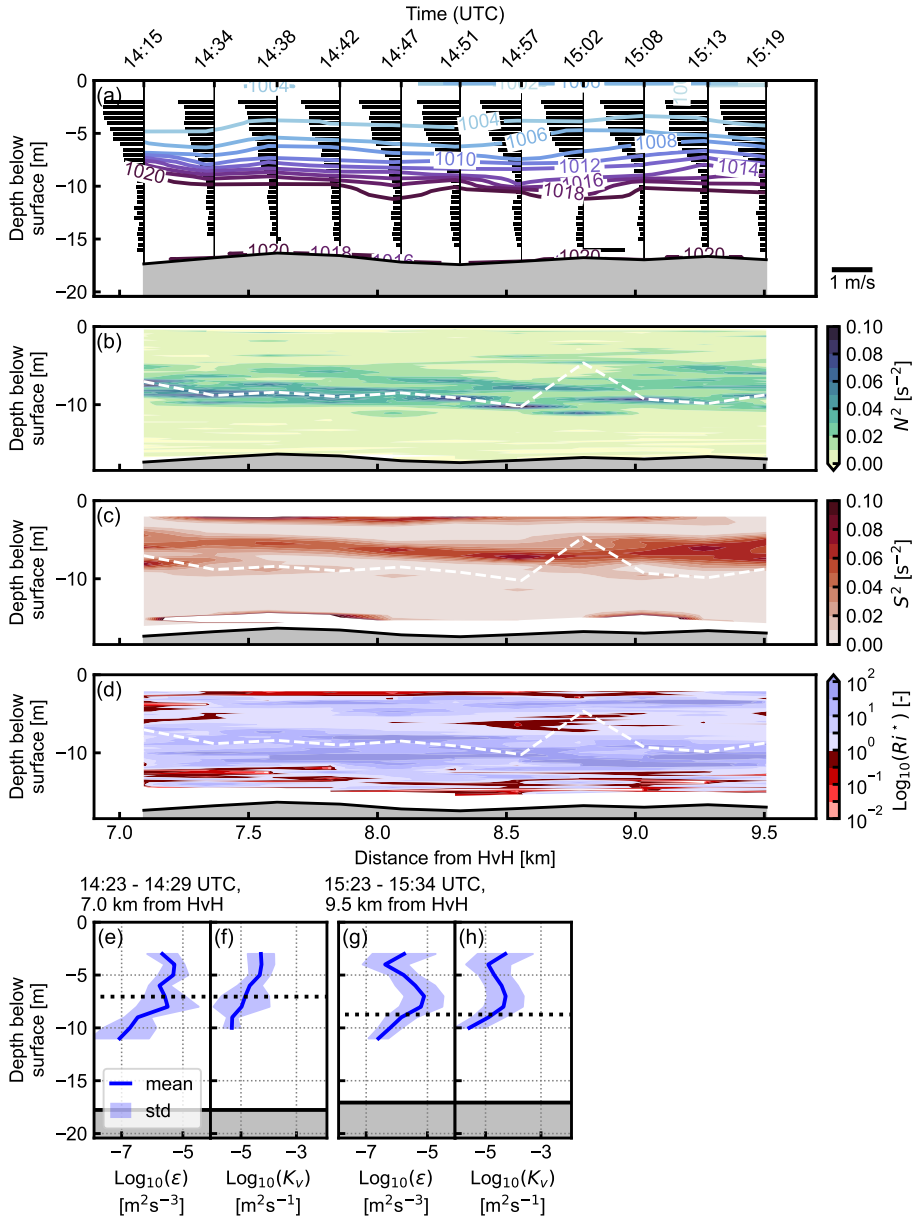


**Figure 2.5:** (a) Internal flow structure (along-channel velocity and density), (b) buoyancy frequency  $N^2$ , (c) velocity shear squared  $S^2$ , (d) dimensionless gradient Richardson number  $Ri^* = \frac{Ri}{0.25}$ , (e-h) MicroCTD profiles of TKE dissipation rates and diffusivity rate along the section between 14:15 and 15:19 UTC (beginning of ebb tide), on October 1<sup>st</sup>, 2021. The white dashed line indicates the pycnocline depth, defined as the maximum gradient in  $N^2$ . The x-axis indicates kilometres from Hoek van Holland (sea side).

0.08 and  $0.10 \text{ s}^{-2}$ ), indicating turbulence damping at the pycnocline. Turbulence observations below the pycnocline were unfortunately not available for this phase of the tide.

The profile of  $K_v$  aligns with the observations of  $Ri$  (Fig. 2.4d). The strong shear above the pycnocline, combined with a weaker stratification than at the pycnocline, were responsible for  $Ri < 0.25$  in the upper layer. Towards the pycnocline,  $N^2$  increased (Fig. 2.4b). Therefore, the highest values of  $Ri > 1$  were found around the pycnocline.

During the progressing ebb tide in October 2021 (Fig. 2.5), flow velocities increased throughout the water column while the overall stratification pattern persisted. The velocity and stratification structure were similar to that observed during high water slack and the onset of ebb tide, but with higher flow velocities at all depths (compare Figure 2.4a and Figure 2.5a). Consequently, the strongest velocity shear within this transect was concentrated in a narrow band approximately 1–2 m above the pycnocline, with values ranging from  $0.06$  to  $0.09 \text{ s}^{-2}$ . This elevated shear resulted from a pronounced increase in ebb velocities within the upper layer relative to the preceding transect, while velocities just below the pycnocline were around  $0.1 \text{ ms}^{-1}$ , leading to enhanced vertical velocity gradients.

Observations of turbulence and mixing showed evidence of shear-driven generation of turbulence above the pycnocline, indicated by a maximum TKE dissipation rate at 5 meters depth for 7.0 km from the mouth (Fig. 2.5e-f) and at 7 meters depth at 9.5 km from the mouth (Fig. 2.5g-h). The associated values of  $\varepsilon$  and  $K_v$  are  $10^{-5} \text{ m}^2 \text{ s}^{-3}$  and  $10^{-4} \text{ m}^2 \text{ s}^{-1}$ , respectively, similar to the values observed at the beginning of the ebb tide. Below this maximum, turbulence was damped by the pycnocline and values of  $\varepsilon$  and  $K_v$  decreased by about two orders of magnitude. This aligned with the observed values of  $Ri$ . There were patches with  $Ri < 0.25$  in the upper layer, while the pycnocline itself was stable with  $Ri > 1$  (Fig. 2.5d).

### Partially mixed ebb tide July 2022

During the partially mixed ebb tide in July 2022 (Fig. 2.6), the estuary exhibited pronounced spatial variability in stratification and shear. Observations captured a transition from a well-mixed bottom layer overlain by a stratified surface layer to a stratified bottom layer with a stratified surface layer (Fig. 2.6a). Stratified regions were associated with elevated velocity shear, with  $S^2 > 0.01 \text{ s}^{-2}$ , compared to less stratified regions where  $S^2 < 0.01 \text{ s}^{-2}$  and  $N^2 < 0.02 \text{ s}^{-2}$  (Fig. 2.6b and c). The strongest shear was observed around the pycnocline, reaching values of  $S^2 = 0.06\text{--}0.07 \text{ s}^{-2}$  at approximately 8.5 km from Hoek van Holland and between 8 and 10 m depth (Fig. 2.6c). Additional regions of elevated shear ( $S^2 > 0.08 \text{ s}^{-2}$ ) occurred locally near the surface and close to the bed. The observations of maximum shear around the pycnocline indicate that this shear is predominantly internally generated, arising from vertical shear within the flow rather than from bottom friction alone.

The MicroCTD profiles showed pronounced spatial variability across the transect (Fig. 2.6e–j), consistent with the observed horizontal variation in stratification. In the first profile, eddy diffusivity values were lowest above the pycnocline (located at approximately 6 m depth), with  $K_v \approx 10^{-5} \text{ m}^2 \text{ s}^{-1}$ , and increased below the pycnocline to values of up to  $K_v \approx 10^{-4} \text{ m}^2 \text{ s}^{-1}$  at around 11 m depth (Fig. 2.6e, f). Locations of enhanced turbulence and diffusivity consistently aligned with regions of elevated velocity shear within the domain covered by the MicroCTD profiles. In the region of strongest mid-depth shear, TKE dissipation rates and mixing intensified markedly, with  $\varepsilon$  reaching values of approximately  $10^{-4} \text{ m}^2 \text{ s}^{-3}$  and  $K_v$  increasing to about  $10^{-3} \text{ m}^2 \text{ s}^{-1}$  at around 8 m depth (Fig. 2.6i, j). The vertical extent of this enhanced mixing was largely confined to the region of elevated shear.

This region of maximum mid-depth shear also coincided with values of  $Ri < 0.25$ , indicating a potential for shear-driven mixing at approximately 8.5 km from Hoek van Holland between 8 and 10 m depth (Fig. 2.6d). Additional regions with  $Ri < 0.25$  and elevated shear were observed closer to the surface between 6.5 and 11 km from Hoek van Holland.

As the ebb tide progressed on the July 2022 survey (Fig. 2.7), the bottom layer was characterised by low velocities and the strongest stratification, while the upper layer exhibited higher velocities and weaker stratification (Fig. 2.7a). Velocity shear was highest in the bottom layer, with  $S^2$  values ranging from 0.01 to  $0.06 \text{ s}^{-2}$ , while the upper layer generally exhibited weaker shear, with  $S^2 < 0.01 \text{ s}^{-2}$ . In contrast, the surface layer was characterised by higher velocities and weaker stratification, yet velocity shear remained low.

Despite the elevated shear near the bed, eddy diffusivity profiles generally show larger values above the pycnocline than below it (Fig. 2.7e–j), which is unexpected based on the observed shear distribution. Although the MicroCTD profiles do not extend to the bed, the first two profiles exhibit a local maximum in diffusivity just below the pycnocline (Fig. 2.7e–h). Overall, diffusivity values during this transect were relatively low compared to other observations that day, with typical values of  $K_v \approx 10^{-5} \text{ m}^2 \text{ s}^{-1}$ . An exception occurs at 5 km, the very beginning of the transect, around 5 meter depth, there is a maximum of  $K_v \approx 10^{-4} \text{ m}^2 \text{ s}^{-1}$ , but the origin of this turbulence maximum is unclear from the ADCP and CTD measurements (Fig. 2.7e–f). Conditions earlier than captured by our observations might have contributed to the generation of mixing here.

The  $Ri$  values are generally above 0.25, consistent with the overall weak turbulence levels. Notably, the diffusivity maximum observed at 5 km does not coincide with regions of  $Ri < 0.25$ , suggesting that this local enhancement in mixing is not directly associated with shear instability during the measurement period.

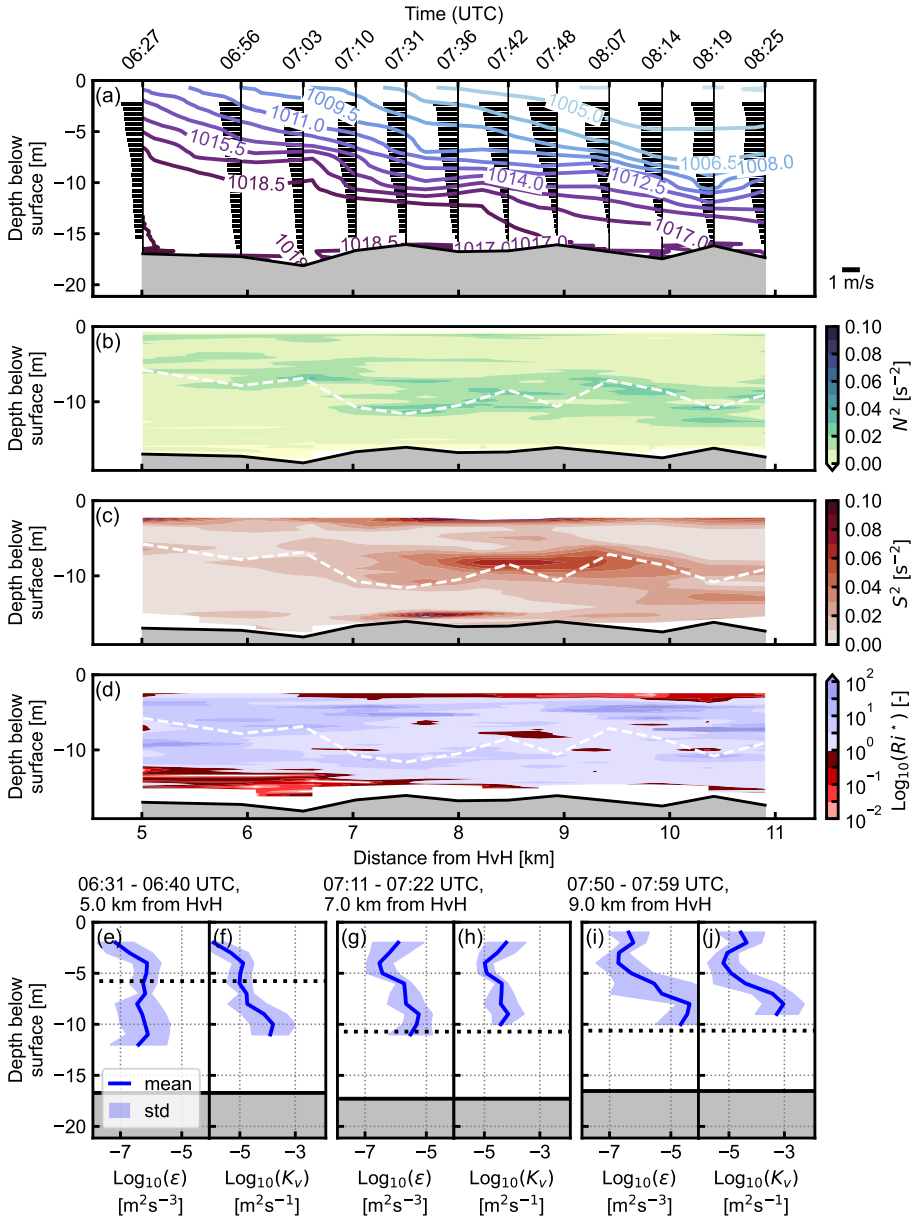


**Figure 2.6:** (a) Internal flow structure (along-channel velocity and density), (b) buoyancy frequency  $N^2$ , (c) velocity shear squared  $S^2$ , (d) dimensionless gradient Richardson number  $Ri^* = \frac{Ri}{0.25}$ , (e-j) MicroCTD profiles of TKE dissipation rates and diffusivity rate along the section between 6:27 and 8:25 UTC (beginning of ebb tide), on July 15, 2022. The white dashed line indicates the pycnocline depth, defined as the maximum gradient in  $N^2$ . The x-axis indicates kilometres from Hoek van Holland (sea side).

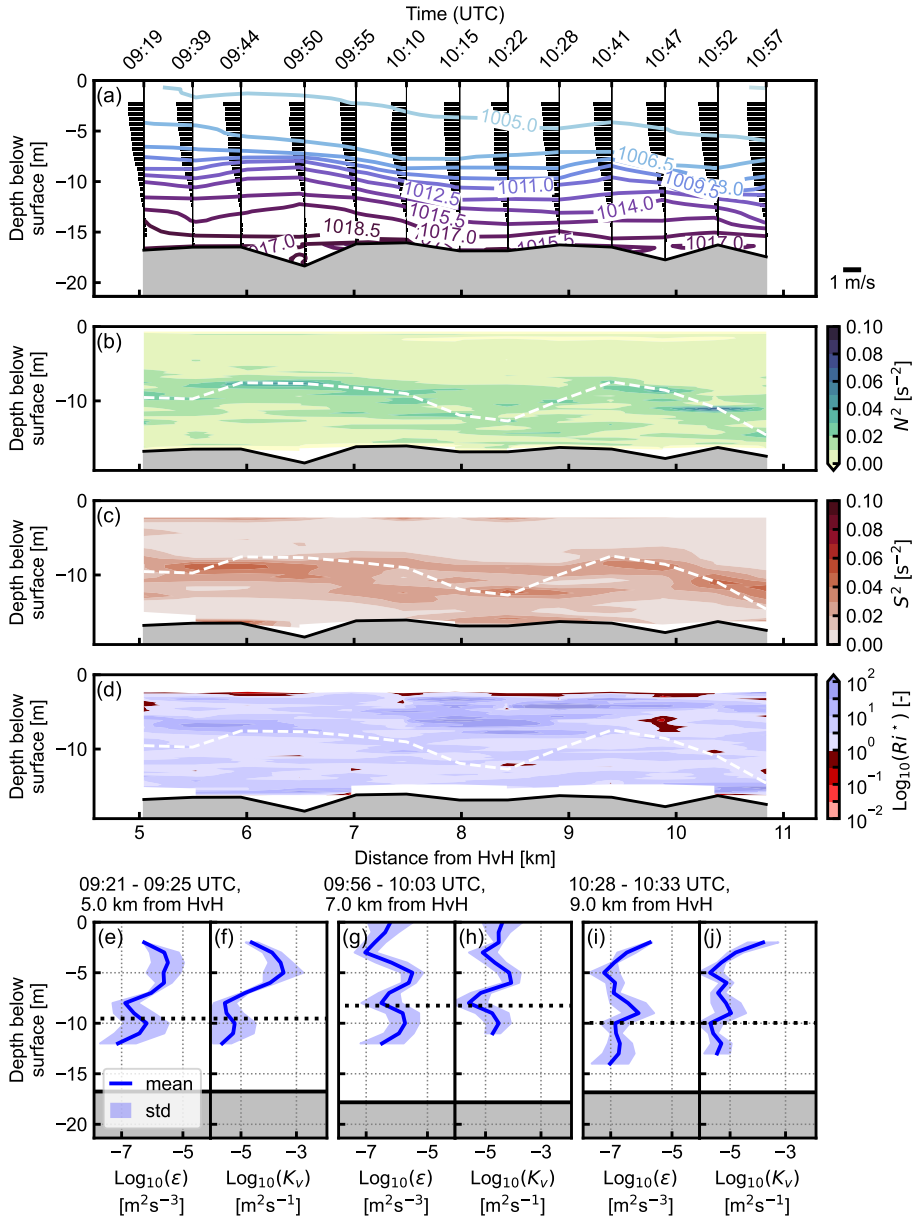


**Figure 2.7:** (a) Internal flow structure (along-channel velocity and density), (b) buoyancy frequency  $N^2$ , (c) velocity shear squared  $S^2$ , (d) dimensionless gradient Richardson number  $Ri^* = \frac{Ri}{0.25}$ , (e-j) MicroCTD profiles of TKE dissipation rates and diffusivity rate along the section between 9:19 and 10:58 UTC (ebb tide), on July 15, 2022. The white dashed line indicates the pycnocline depth, defined as the maximum gradient in  $N^2$ . The x-axis indicates kilometres from Hoek van Holland (sea side).

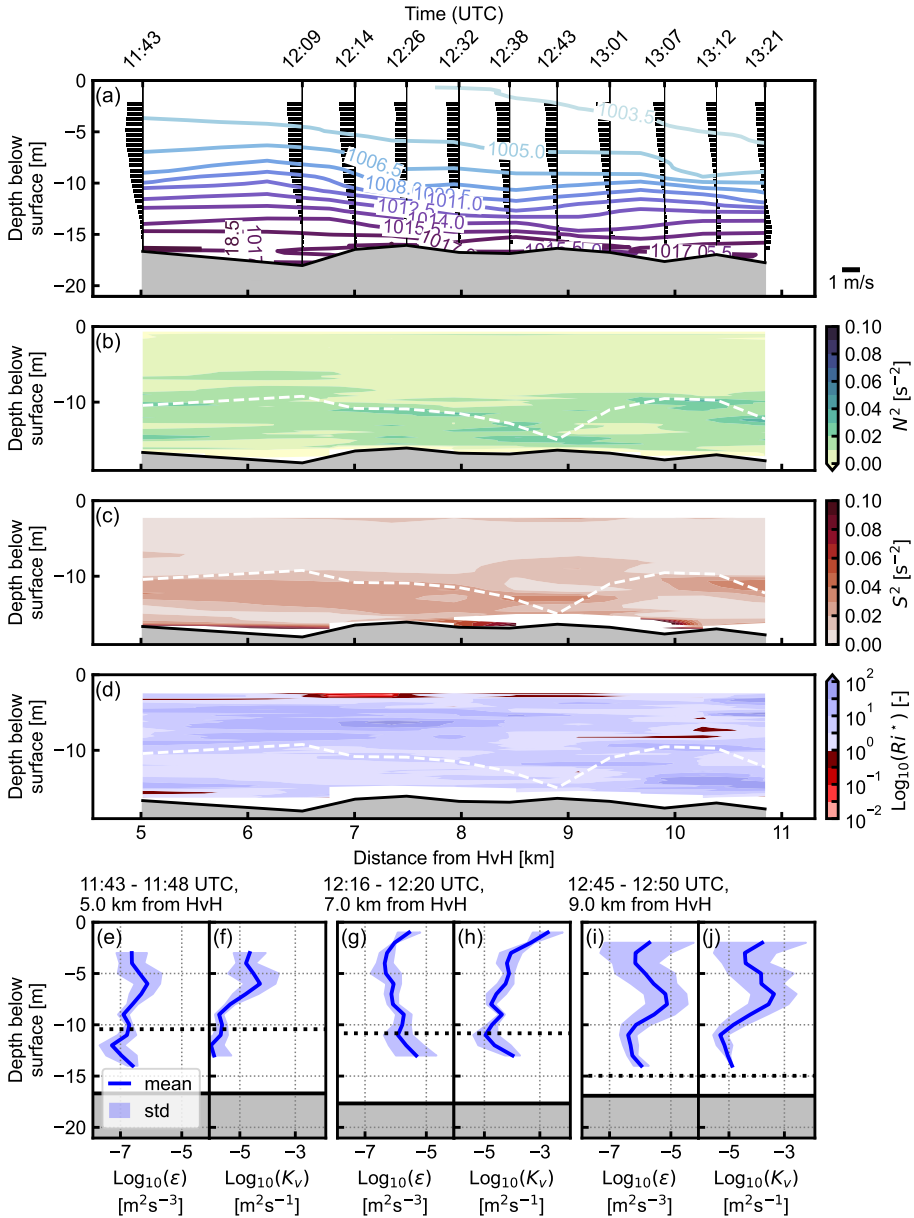


**Figure 2.8:** (a) Internal flow structure (along-channel velocity and density), (b) buoyancy frequency  $N^2$ , (c) velocity shear squared  $S^2$ , (d) dimensionless gradient Richardson number  $Ri^* = \frac{Ri}{0.25}$ , (e-j) MicroCTD profiles of TKE dissipation rates and diffusivity rate along the section between 11:43 and 13:21 UTC (ebb and slack tide), on July 15, 2022. The white dashed line indicates the pycnocline depth, defined as the maximum gradient in  $N^2$ . The x-axis indicates kilometres from Hoek van Holland (sea side).

### Partially mixed ebb to low water slack July 2022

During the final stages of ebb tide and the transition to low water slack in July 2022, stratification and shear weakened throughout most of the transect. This period exhibited the lowest observed density of approximately  $1003.5 \text{ kg m}^{-3}$  (Fig. 2.8a), accompanied by the weakest stratification of the July 2022 survey, with maximum  $N^2$  values of about  $0.05 \text{ s}^{-2}$  in the lower layer (Fig. 2.8b).

Velocity shear along this transect was weaker than during earlier stages of the ebb tide and was primarily confined to the stratified bottom layer, where maximum values of  $S^2$  reached approximately  $0.04 \text{ s}^{-2}$  (Fig. 2.8c).

Microstructure observations (Fig. 2.8e–j) indicated generally weak mixing throughout most of the transect, particularly within the stratified lower layer, where eddy diffusivity values ranged from approximately  $10^{-6}$  to  $10^{-4} \text{ m}^2 \text{ s}^{-1}$ .

Consistent with these weak turbulence levels, the gradient Richardson number exceeded 0.25 across most of the transect. Localised exceptions were observed at approximately 7 km from Hoek van Holland, where enhanced near-surface turbulence coincided with a region of low  $Ri$ , and at around 9 km, where elevated turbulence at approximately 7 m depth corresponded to  $Ri \approx 0.25$ .

### 2.4.2 Parameterisations

Table 2.1 presents the calibrated values of the constants  $c_1$ – $c_7$  in Equations 2.5–2.8, obtained by fitting the parameterisations to the full dataset.

**Table 2.1:** Calibrated values of constants in the turbulence parameterisations.

Constant	Value	Unit	Parameterisation
$c_1$	$1.65 \cdot 10^{-4}$	$\text{m}^2 \text{ s}^{-1}$	MA
$c_2$	$4.0 \cdot 10^{-3}$	$\text{m}^2 \text{ s}^{-1}$	PP
$c_3$	$4.6 \cdot 10^{-5}$	$\text{m}^2 \text{ s}^{-1}$	PP
$c_4$	0	$\text{m}^2 \text{ s}^{-1}$	PP
$c_5$	$2.6 \cdot 10^{-4}$	-	LB
$c_6$	$4.0 \cdot 10^{-5}$	-	PK
$c_7$	1.7	-	PK

Examples of profiles of  $Ri$  and  $K_v$  from parameterisations and observations as a function of depth are shown in Figure 2.9. Figure 2.9a and b show a situation where  $Ri$  had a minimum around  $z = -4 \text{ m}$ , and increased towards the surface and the bed, while  $K_v$  indicated the opposite pattern: it attained a maximum around  $z = -4 \text{ m}$ , and decreased above and below it.

Some agreement was observed between the observations and the parameterisations (e.g.  $R^2 = 0.53$  for MA). However,  $K_v$  was underestimated around  $z = -10 \text{ m}$ , especially for LB. Figure 2.9c and d display a measurement where  $Ri$  varied only slightly over the observed vertical range, remaining between 0 and

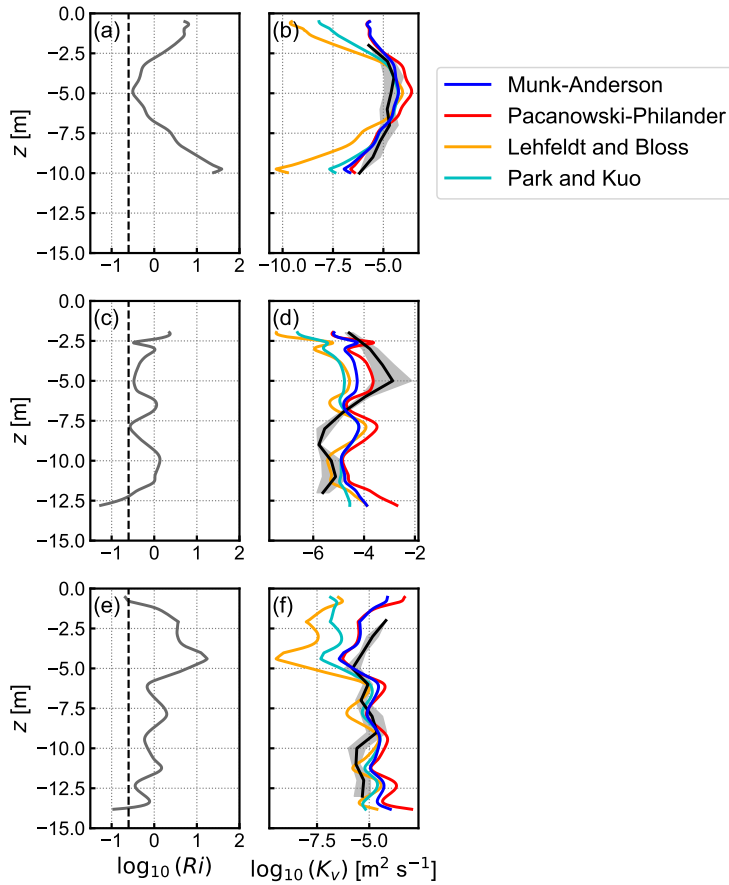


**Figure 2.9:** (a) Richardson number  $Ri$  as a function of depth, based on velocity observations from the ADCP and density observations from the MicroCTD. Observations taken on 13:36 - 13:50 October 1, 2021. (b) Estimated vertical eddy diffusivity  $K_v$ , from the MicroCTD observations (in black) as function of depth. The grey shaded area indicates one standard deviation. Observations taken on 13:36 - 13:50 October 1, 2021. The coloured lines indicate the values of  $K_v$  from the different parameterisations. (c)-(d) As (a)-(b), but for 09:21 - 09:25 July 15, 2022. (e)-(f) As (a)-(b), but for 10:28-10:33 July 15, 2022.

2.5. Here,  $K_v$  had a strong vertical gradient, and decreased three orders of magnitude from  $z = -5$  m to  $z = -9$  m. This pattern was not reflected in the vertical variation of  $Ri$ , and as a result, the parameterisations failed to capture this behaviour, instead producing a fairly constant profile of  $K_v$  in the vertical, outside the range of one standard deviation from the measurements. In Figure 2.9e,  $Ri$  had a maximum around  $z = -4.5$  m, but fluctuated around  $\log_{10}(Ri) = 0$  below  $z = -6$  m. The observed  $K_v$  decreased between  $z = -2$  m and  $z = -5$  m, and fluctuated around  $10^{-5} \text{ m}^2 \text{ s}^{-1}$  below  $z = -5$  m. The MA and PP parameterisations captured this entire pattern, while LB and PK underestimated  $K_v$  in the upper

layer.

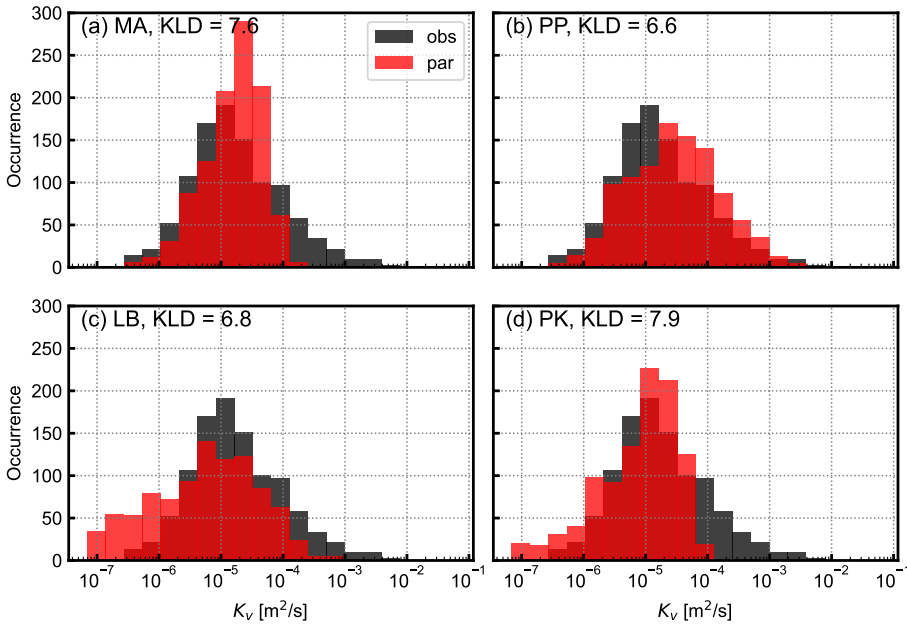


**Figure 2.10:** (a) Histogram of the estimated  $K_v$  of all casts (in black), and the corresponding values from the Munk and Anderson (1948) parameterisation (in red). (b)-(d) As (a), but for  $K_v$  calculated with the Pacanowski and Philander (1981), Lehfeldt and Bloss (1988) and Park and Kuo (1993) parameterisations, respectively.

To give insight into the comparison of the statistical properties of  $K_v$ , histograms of observed and parametrised  $K_v$  are shown in Figure 2.10. The best statistical agreement for  $K_v$  was found with the Pacanowski and Philander (1981) parameterisation, which resolved the full range of  $K_v$  well, in contrast to the other parameterisations that failed to represent the high  $K_v$  values. The MA parameterisation overpredicted the occurrence of the median  $K_v$  (approximately  $5 \cdot 10^{-4} \text{ m}^2 \text{ s}^{-1}$ ), while the LB and PK parameterisations predicted low  $K_v$  values too frequently.

When binning the results in bins of 1 meter (Figs. A.2-A.5), it is visible that the parameterisations which only use  $Ri$  as input (MA and PP) overestimated  $K_v$  in the lower 6 meter of the water column: the median of the observations at  $z = -10 \text{ m}$  is  $9.3 \cdot 10^{-6} \text{ m}^2 \text{ s}^{-1}$ , but this value was  $2.2 \cdot 10^{-5} \text{ m}^2 \text{ s}^{-1}$  for MA and  $4.0 \cdot 10^{-5} \text{ m}^2 \text{ s}^{-1}$  for PP. On the other hand, the parameterisations which use the Rossby and Montgomery (1935) formulation for vertical mixing in the unstratified situation (LB and PK) resolved the lower part better but underestimated  $K_v$  above  $z = -5 \text{ m}$ : median values at  $z = -3 \text{ m}$  were  $1.5 \cdot 10^{-5} \text{ m}^2 \text{ s}^{-1}$  for observations but  $1.4 \cdot 10^{-6} \text{ m}^2 \text{ s}^{-1}$  for LB and  $2.4 \cdot 10^{-6} \text{ m}^2 \text{ s}^{-1}$  for PK. When considering the full depth range where observations were available, there was no improvement in terms of

representing the statistics of  $K_v$  by applying the Rossby and Montgomery (1935) formulation.

## 2

## 2.5 Discussion

In this chapter, we presented results from two surveys in the Rotterdam Waterway measuring turbulence characteristics, flow structure and stratification. We observed a stable stratification throughout the tidal cycle, in contrast to many other estuaries such as the Fraser River (Geyer and Farmer, 1989), the Merrimack River (Ralston et al., 2010), and the Connecticut River (Geyer et al., 2010) estuaries. In those estuaries, the salinity structure typically breaks down on the late ebb tide. This difference may be explained by the considerable depth of the Rotterdam Waterway. Similar to other urbanised deltas, for example the Duwamish River Estuary (McKeon et al., 2021), the Rotterdam Waterway is over-deepened to accommodate ship traffic. This may result in the inability of the bottom boundary layer turbulence to influence mixing at the interface.

The novel aspect of this chapter, for the Rotterdam Waterway, is the inclusion of direct turbulence measurements that cover a substantial fraction of the water column and generally exhibit minima in TKE dissipation rate and turbulent diffusivity at the pycnocline, indicating turbulence damping consistent with an overall stable pycnocline ( $Ri > 1$ ). This is in line with observations of  $Ri$  by de Nijs et al. (2011). However, they did not have turbulence measurements to confirm this. Furthermore, de Nijs et al. (2011) showed higher rates of  $K_v$  estimated from Munk and Anderson (1948) than the values that we found throughout the tidal cycle. Maximum values of  $K_v$  were observed during flood tides, and were confined below the pycnocline. The pycnocline height rises over the course of the flood tide due to advection, which led to increasing maximum  $K_v$  values due to a growing bottom boundary layer. This difference might be attributed to the lack of near-bed turbulence measurements or to the different methods applied. Despite the lack of turbulent measurements below the pycnocline during flood tide, the low  $Ri$  values suggest this was still the case during our survey in 2021.

Most turbulence observations in stratified or salt wedge estuaries like the Merrimack River estuary and the Connecticut River estuary focused on the ebb tide (e.g., Geyer et al., 2008; Scully et al., 2011; Holleman et al., 2016). The reason is that most mixing in those estuaries takes place on the ebb tide, with a consequential breakdown of the salinity structure. During the ebb tide, strong shear can develop, Geyer et al. (2008) and Holleman et al. (2016) identified an initial intermittent intense mixing at the beginning of ebb, and more homogeneous shear-induced mixing during mid-ebb. Our measurements of 2022 also showed the strongest shear at the beginning of ebb tide, but despite the decreasing shear, high values of TKE dissipation rates were still visible during the late ebb. Geyer et al. (2017) conducted turbulence measurements throughout the tidal cycle, where the Richardson numbers have a median of roughly 0.25 during ebb, but values of

$Ri > 0.25$  during flood tide. We also showed strong shear development during the flood tide, due to the presence of mid-depth jets, however, the  $Ri$ -values at the pycnocline stayed above 0.25.

We observed values of TKE dissipation rates of around  $\varepsilon \approx 10^{-6} - 10^{-5} \text{ m}^2 \text{ s}^{-3}$ . This is one to two orders of magnitude lower than values observed in shear instabilities in the Connecticut River estuary. In the braid mixing zones values of up to  $6.8 \cdot 10^{-4} \text{ m}^2 \text{ s}^{-3}$  were observed (Geyer et al., 2010). In the core and downstream regions of the braids, those values were lower (Geyer et al., 2010), but generally still higher than the TKE dissipation rates observed in the Rotterdam Waterway. Also values of  $\varepsilon$  in the Merrimack reached up to  $1.4 \cdot 10^{-4} \text{ m}^2 \text{ s}^{-3}$  (Geyer et al., 2008). The reason for this difference remains speculative. Both studies employed highly sophisticated instrumentation, allowing them to resolve turbulent structures at much finer spatial and temporal scales than was possible in our study. This difference may partly account for the differences in the observed turbulence values. Furthermore, the Rotterdam Waterway is strongly stratified due to its large water depth, in contrast to the aforementioned estuaries, where the salt wedge breaks down due to strong shear at the pycnocline.

The comparison between observed and parameterised  $K_v$  shows differences exceeding up to  $\mathcal{O}(10^4)$  between individual profiles (Fig. 2.9), but the statistical properties are better represented (Fig. 2.10). First, flow features with smaller spatial scales than those taken into account in our method to obtain  $Ri$ , like internal waves and shear instability, are not explicitly taken into account in the parameterisations. However, these features, which may generate turbulence (Pietrzak et al., 1990, 1991; Kranenburg et al., 1991; Geyer et al., 2010), were observed during our surveys (Fig. A.6). Second, the considered parameterisations assume that the strength of the vertical mixing depends on local flow properties. However, turbulence history and turbulence generated outside the local flow can contribute to vertical mixing (Scully et al., 2011) and may violate this assumption. Third, the calculation of  $K_v$  from observations is based on certain assumptions, which may not all hold under all considered circumstances. An important assumption is a constant mixing efficiency  $\Gamma = 0.2$ . It is well-known that this value varies in nature (Holleman et al., 2016). However, an estimation of  $\Gamma$  by the Tjernstrom parameterisation (Tjernström, 1993; Huguenard et al., 2015), showed that  $\Gamma$  was nearly constant around 0.2.

The parameterisations developed for the ocean (MA and PP) perform better close to the surface and at mid-depth than close to the bottom. This is because they do not properly account for the influence of the bottom in estuaries, which limits the size of turbulent eddies that can develop. In estuaries, a larger portion of the water depth is boundary-limited than in the open ocean. This suppresses turbulence, causing MA and PP to overestimate the value of  $K_v$  in the bottom layer. LB and PK take this effect of the relative water depth into account and therefore show better agreement close to the bottom than MA and PP. However, near the surface, these parameterisations tend to underestimate  $K_v$ , suggesting that the effect of the surface on turbulence is not properly accounted for. This

is probably because LB and PK consider a parabolic shape function for turbulent diffusivity, while Basdurak et al. (2023) showed that other shape functions may be more appropriate to account for the effect of surface boundary layer entrainment. Shape functions in parameterisations can potentially improve their performance, but hereby careful selection of an appropriate shape function is essential.

When considering the full-depth range, the statistical disagreement between the observations and the parameterisations is not better for LB and PK, despite being more sophisticated. This may however be due to the fact that the majority of the observations are in the upper half of the water column, which creates a bias in performance towards parameterisations that resolve this depth range properly. Extending the dataset by additional observations, especially close to the bottom, would help better constrain the performance of the parameterisations.

Both the dataset of the surveys and the results of the performance of the parameterisations are useful for the validation and improvement of salt intrusion models. From the Richardson number in a complex numerical model, the associated vertical diffusivity can be estimated using the parameterisations, which can be compared to the output of the second-order turbulence closure. Differences between the statistical properties of those two can subsequently be analysed to gain insight into the performance of the turbulence model. In idealised models, the parameterisations could be used as a turbulence closure, for example in models as those presented in McCarthy (1993) and Chen and de Swart (2016). Including a dependence of  $K_v$  on  $Ri$  in these models has the potential to increase the understanding of salinity dynamics, which can be gained from them. This study shows that a stochastic representation of  $K_v$ , based on the parameterisations, is the most promising. For salt intrusion in estuaries, representing turbulence as a stochastic process is a rather new concept, but studies in other fields have shown added value of this approach (Arenas-López and Badaoui, 2020; Sanchez et al., 2016; Freire and Chamecki, 2018; Bauer et al., 2020).

## 2.6 Conclusions

A dataset containing observations of salinity, flow and turbulence was collected in the Rotterdam Waterway. Analysis of these data shows that the salt wedge remains stable throughout the tidal cycle. The highest values of velocity shear and density stratification frequently coincided within the transect, indicating that stratification suppresses vertical mixing and promotes shear at the pycnocline. In contrast, regions of weak stratification exhibit reduced shear, highlighting the dominant role of stratification in governing turbulence and flow structure in the Rotterdam Waterway.

Around mid-depth, both turbulence damping by stratification and turbulence generation by sheared flow were observed. Turbulence levels were generally higher during ebb tide than during flood tide, consistent with enhanced shear during

ebb.

During the stratified conditions (October 2021), velocity shear exceeded  $0.06 \text{ s}^{-2}$  in every transect, but the turbulence was dampened by the stratification, and mixing rates were characterised by  $K_v \approx 10^{-5} - 10^{-4} \text{ m}^2 \text{ s}^{-1}$ . During the partially mixed conditions (July 2022), velocity shear remained below  $0.06 \text{ s}^{-2}$  on the later stages of ebb tide, but higher diffusivity rates of  $K_v \approx 10^{-4} - 10^{-3} \text{ m}^2 \text{ s}^{-1}$  occurred at mid-depth episodically, because the associated stratification was lower than during the 2022 survey. Regions with  $Ri < 0.25$ , indicative for the potential of mixing, were mostly confined to the bottom layer and near the surface, with occasional small patches occurring around the pycnocline, consistent with a generally stable pycnocline.

Among the tested parameterisations, Pacanowski and Philander (1981) best reproduces the statistical relationship between  $Ri$  and vertical eddy diffusivity, supporting its use for representing vertical mixing under stratified estuarine conditions. The other investigated parameterisations fail to reproduce the largest values of the vertical mixing.



# 3

## Observations of estuarine salt intrusion dynamics during a prolonged drought event in the Rhine-Meuse Delta

### Key Points

- On a weekly timescale the river discharge is the best predictor for salt intrusion length.
- Variations of salt intrusion length on a timescale of a few days are driven by coastal set-up.
- Treating distributary side branches separately is crucial to incorporate the importance of downstream salinity variability.

---

This chapter has been published as:

Wegman, T. M., Pietrzak, J. D., Horner-Devine, A. R., Dijkstra, H. A., & Ralston, D. K. (2024). Observations of estuarine salt intrusion dynamics during a prolonged drought event in the Rhine-Meuse Delta. *Journal of Geophysical Research: Oceans*, 129, e2024JC021655. doi:10.1029/2024JC021655.

The measurement data is available in the repository of 4TU.ResearchData, with doi:10.1029/2024JC021655.

## Abstract

Salt intrusion poses a global threat to estuaries and deltas, exacerbated by climate change, drought, and sea level rise. This observational study investigates the impact of river discharge, wind, and tidal variations on salt intrusion in a branching river delta during drought. The complexity and spatial extent of deltas make comprehensive measurements challenging and rare. In this chapter, we present a 17-week data set of a historic drought in the Rhine-Meuse Delta, capturing dynamics in a multiple-channel system in a wide range of conditions. Key characteristics of this low-lying delta are its branching channel network and complicated, human-controlled discharge. Despite the system's complexity, we found that the subtidal salt intrusion length, defined by the 2 PSU isohaline ( $L_2$ ), follows a power law relationship with Rhine River discharge ( $L_2 \propto Q_R^{-0.35 \pm 0.03}$ ). Subtidal water level variations contribute to short-term variations in intrusion length, shifting the limit of salt intrusion upstream and downstream with a distance similar to the tidal excursion length. This can be attributed to the up-estuary transport of seawater, caused by the estuary adjusting to variations in water levels at its mouth. However, spring-neap variation in the tidal range does not alter the subtidal salt intrusion length. Side branches exhibit distinct dynamics from the main river, and their most important control is the downstream salinity. We show that treating the side branches separately is crucial to incorporate the highly variable downstream boundary condition, and may apply in other deltas or complex estuaries.

### 3.1 Introduction

Estuaries connect saline sea waters and fresh river waters, creating unique coastal systems. Estuaries are vital for many people globally, as they usually house many inhabitants and industrial activities. When saline seawater is advected far inland, it intrudes into what are normally freshwater regions. This can cause major problems, increasing the stress on the freshwater supply for industry, agriculture, and drinking water. The extent to which saline waters enter the estuary, referred to as the salt intrusion length, is influenced by the estuary's geometry and forcing conditions. Due to variations in forcings such as river discharge, tides, winds, and mean sea level, the salt intrusion length can vary significantly within the estuary (MacCready and Geyer, 2010).

Due to a changing climate, delta regions may experience an intensification of salt intrusion, attributed to rising mean sea levels, a decrease in low flow river discharge (Kay et al., 2018; Lee et al., 2024), or a combination of both. In future discharge projections, the occurrence of extreme salt intrusion events in many European estuaries is expected to increase by a factor of five by the end of the 21<sup>st</sup> century (Lee et al., 2024). Similar trends are anticipated globally, for example, in the Mekong Delta (Eslami et al., 2019, 2021b), the Yangtze Estuary (Dai et al., 2011), the Bengal Delta (Sherin et al., 2020), and the Pearl River Estuary (Liu et al., 2019; Hong et al., 2020). Besides the effects of climate change, direct anthropogenic drivers leading to sediment starvation, and deeper channels, can exacerbate salt intrusion (Eslami et al., 2019, 2021a).

The salinity distribution in an estuary can be described by the balance between salt export by advection due to river discharge, and salt import by the baroclinically driven exchange flow and dispersion processes by the tides (e.g., Hansen and Rattray, 1965; Chatwin, 1976; MacCready, 2004). To evaluate the impact of forcing conditions such as river discharge, winds, and the spring-neap tidal cycle on salt intrusion, it is useful to examine the subtidal response of an estuary because those forcing conditions act on timescales longer than a single tidal cycle (Jay, 2010).

The estuarine response time varies seasonally with discharge and has been examined by, for example, Monismith et al. (2002), Chawla et al. (2008), Ralston et al. (2010), McKeon et al. (2021), and Cook et al. (2023). Salt intrusion length depends strongly on the amount of discharge, where this relationship becomes stronger as discharge increases (Abood, 1974; Ralston et al., 2010; Cook et al., 2023). The sensitivity of the salt intrusion to spring-neap variation in tides can exhibit seasonal differences because it depends, among other factors, on the response time of the estuary. The response time depends on the river flow and length of the estuary (MacCready, 2007; Lerczak et al., 2009), so during droughts the response time may be long compared to the spring-neap cycle. For example, the salt intrusion length in the Hudson River Estuary becomes insensitive to the spring-neap cycle during droughts, because the response time is 10 times larger than during moderate flow and thus much longer than the spring-neap

cycle (Bowen and Geyer, 2003; Lerczak et al., 2009).

Besides the discharge and tides, winds can also influence the salt intrusion length. Winds can induce subtidal water level fluctuations, influencing the barotropic pressure gradient between the ocean and the estuary. Large up-estuary volume fluxes can be generated due to these variations in the subtidal water level. These can be in the order of magnitude of the river runoff (Wong and Valle-Levinson, 2002; Ralston et al., 2008; de Nijs et al., 2008), and thereby affect salinity concentrations throughout the estuary (de Nijs et al., 2008; Li and Li, 2011; Manca et al., 2014; Perales-Valdivia et al., 2018; Zhu et al., 2020; Eslami et al., 2021a; Cook et al., 2023).

The focus area of this study is the Dutch Rhine-Meuse Delta, a large, urbanised river delta with a branching channel network. Compared to single-channel estuaries, these systems include a more complex discharge distribution, different channel geometries, abrupt depth changes, and more complex tidal phase differences (Hill and Souza, 2006; Alebregtse and de Swart, 2016; Cox et al., 2021). This could introduce additional processes relevant to salt intrusion dynamics. For instance, the mixing of water masses in side channels, which is similar to tidal trapping and may lead to tidal dispersion, as described by e.g., Stacey et al. (2001) and MacVean and Stacey (2011). This can be a dominant term in multichannel estuaries, as shown for the Coos estuary by Conroy et al. (2020), and it can be further enhanced by exchange flow between side-channels and the main channel (Garcia et al., 2022). Additionally, reversals in along-channel salinity gradients can occur at channel junctions (Conroy et al., 2020), which can lead to subtidal along-channel flow convergence (e.g., Warner et al., 2002; MacVean and Stacey, 2011). Furthermore, different responses to forcing for different branches could arise. Eslami et al. (2021a) showed for the Mekong Delta that the stratified branches have a clear spring-neap variability in stratification and salt flux, while some well-mixed channels do not exhibit this response.

High-resolution numerical models provide valuable insights into detailed estuarine dynamics, but only if they are well validated. Field observations are essential for validating these models and understanding the key dynamics of estuarine systems. In deltaic systems or multichannel systems, it is particularly challenging to obtain a data set that captures the spatial and temporal extent required to obtain a deep understanding of the salt intrusion dynamics. Analytical approaches aim to simplify systems to a core set of dynamics, making it easier to study the responses to forcing variability and comparisons among different systems. Analytical modelling studies of salt wedge dynamics date back more than half a century (e.g., Schijf and Schönfeld, 1953) and remain an active area of research (e.g., Poggioli and Horner-Devine, 2015). However, observations that capture the spatial and temporal variability of salt wedge dynamics are rare, especially during the extreme conditions when they are most impactful.

The Rhine-Meuse Delta Estuary is the only permanently open connection between the Rhine and Meuse rivers and the North Sea, characterised as a salt wedge estuary (de Nijs et al., 2011). The Rhine-Meuse Delta is densely populated and

intensively used for agriculture and industry. The most downstream section of the estuary, the Rotterdam Waterway, is the approach channel to Europe's largest harbour (Port of Rotterdam), and undergoes regular dredging for shipping. It is extensively managed by the government and regional water boards, to ensure an adequate freshwater distribution for all stakeholders.

Here, we examine salt intrusion length variations in this heavily engineered delta, focusing on extremely low river discharge conditions. We analyse a data set from the Rhine-Meuse Delta Estuary collected during the severe drought of 2022, featuring the lowest ever recorded Rhine discharge. We investigate the dominant forcing mechanisms driving salt intrusion in a salt wedge estuary experiencing drought, and examine how this differs in two upstream side branches.

In section 3.2, we first describe the theory of the subtidal salt balance. In section 3.3, we describe the observational measurement campaign. In section 3.4, we explain how the subtidal salt intrusion length depends on the observed river discharge, winds, and tides. In sections 3.5 and 3.6, we discuss the results and present the conclusions.

## 3.2 Subtidal salt balance theory

The subtidal salt balance discussed in this section assumes small salinity variations with depth, which applies to partially-mixed and well-mixed estuaries. However, the Rhine-Meuse Delta is a salt wedge estuary, but the upstream branches are partially to well-mixed, which makes this approach applicable to this study. Other salt wedge estuaries have also experienced well-mixed regions during low discharge (e.g., Merrimack River Estuary in Ralston et al. (2010)).

A solution for salt intrusion length  $L_s$  can be found in the balance for a partially-mixed estuary by considering the depth-averaged and tidally averaged, salt conservation balance (Hansen and Rattray, 1965; MacCready, 2004). We can express this as a volume-integrated salt budget when the balance is integrated between the estuary mouth ( $x = 0$ ) and the salt intrusion limit ( $x = L_s$ ), where  $x$  is the distance from the estuary mouth (MacCready, 2004):

$$\frac{1}{A} \left[ \underbrace{\int_0^{L_s} A \frac{\partial \bar{s}}{\partial t} dx + A(L_s) \bar{s}(L_s, t) \frac{dL_s}{dt}}_{s_1} \right] = \underbrace{-\bar{u}\bar{s}}_{s_2} - \underbrace{\overline{u's'}}_{s_3} + \underbrace{K_h \frac{\partial \bar{s}}{\partial x}}_{s_4}. \quad (3.1)$$

Here, the velocity  $u$  and salinity  $s$  distribution are split into a depth-averaged and a depth-varying component,  $u = \bar{u}(T, x) + u'(T, x, z)$  and  $s = \bar{s}(T, x) + s'(T, x, z)$ , where  $T$  denotes the slowly varying timescale longer than the tidal period.  $A$  is the cross-sectional area of the estuary, and  $K_h$  is the along-channel diffusion coefficient. The term  $s_1$  represents the total salt storage tendency over the control volume. It consists of (i) temporal changes in the depth-averaged salinity within the existing salt wedge and (ii) a boundary term proportional to the propagation speed of the salt intrusion limit  $\frac{dL_s}{dt}$ . Under quasi-steady conditions ( $\frac{\partial \bar{s}}{\partial t} \approx 0$ ),  $s_1$

therefore reduces to a term solely proportional to  $\frac{dL_s}{dt}$ . The left hand side of the equation is balanced by  $s_2$ ,  $s_3$ , and  $s_4$ . Here,  $s_2$  is advection by river flow,  $s_3$  is transport by exchange flow, and  $s_4$  is salt import by tidal dispersion.

In terms of understanding salt intrusion length, we also examine how the speed of the intrusion is affected by different mechanisms. This intrusion speed is relevant on shorter timescales (e.g. a few days). A steady-state solution for the salt intrusion length  $L_s$  can be found for  $s_1 = 0$ . This holds for a timescale long enough to average over the shorter-term fluctuations.

A steady-state solution for the salt intrusion length  $L_s$  as a function of river discharge  $Q_R$  can be found in the form  $L_s \propto Q_R^{-n}$ . Estuaries dominated by exchange flow have an exponent of  $n = \frac{1}{3}$ , which assumes a dependency of  $K_h$  on the along-channel salinity gradient (Hansen and Rattray, 1965; MacCready, 1999; Monismith et al., 2002). For estuaries dominated by tidal dispersion, it is assumed that there is no  $K_h$  dependency on the along-channel salinity gradient, resulting in an exponent of  $n = 1$  (Monismith et al., 2002). Salt wedge estuaries have values around  $n = 2$ , based on the arrested salt wedge theory (Schijf and Schönfeld, 1953; Geyer and Ralston, 2011).

The dependence of salt intrusion length on the tidal range and winds can be illustrated by the salt fluxes described in Equation 3.1. The spring-neap response of an estuary depends on the dominant salt flux mechanisms. Stronger tides weaken the exchange flow and stratification and thus reduce the steady salt flux (e.g., Ralston et al., 2008; Geyer et al., 2020), and vice versa. Increasing tidal range also causes greater tidal dispersion, thereby the landward salt flux could be increased (Ralston et al., 2010). In many estuaries, along-estuary wind can either enhance or reduce the exchange flow (Hansen and Rattray, 1965; Geyer, 1997; Scully et al., 2005), where down-estuary wind enhances the estuarine circulation, promoting up-estuary salt transport, and vice versa.

### 3.3 Observations

#### 3.3.1 The Rhine-Meuse Delta

The Rhine-Meuse Delta Estuary is a salt wedge estuary (de Nijs et al., 2011) in the Netherlands. The Rhine River enters the Netherlands at Lobith (Fig. 3.1a), and it enters the domain of the field measurements in the branches which are named Lek and Boven-Merwede. The Meuse enters the Netherlands in the southeast, and is also indicated in Figure 3.1a.

The main branch of the system is the Rotterdam Waterway, which discharges into the North Sea. The most downstream junction branches into the Old Meuse (south) and the New Meuse (north). The New Meuse carries roughly 1/3 of the total Rotterdam Waterway discharge for a low discharge scenario (Cox et al., 2021), see Figure 3.1a. The New Meuse has branches to the Hollandsche IJssel at 36 km upstream of the mouth and to the Lek at 41 km of the mouth. These side branches,

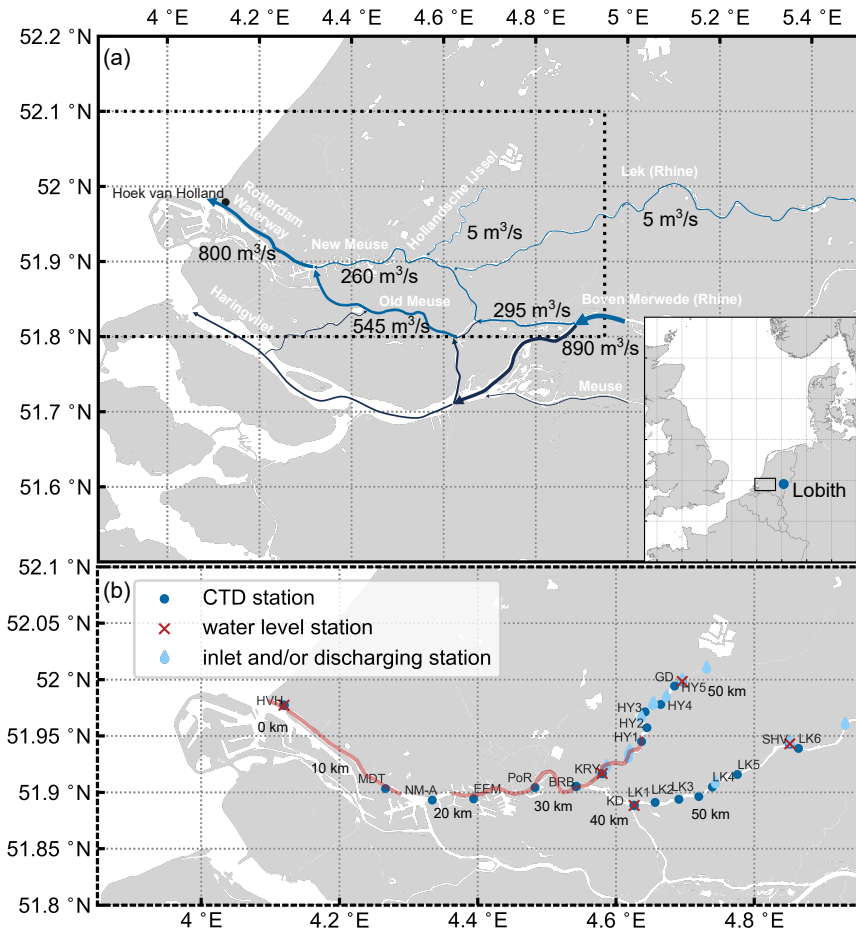


**Figure 3.1:** (a) Overview of the Rhine-Meuse Delta, and its location within Europe. For the relevant branches, the names and approximate discharges are indicated. The arrows scale with the discharges ( $\text{m}^3 \text{s}^{-1}$ ) based on a low Rhine River discharge scenario ( $Q_R < 1000 \text{ m}^3 \text{s}^{-1}$  at Lobith) of Cox et al. (2021). (b) An overview of the measurement locations, where conductivity, temperature, and depth (CTD) sensors in the estuary are indicated with dots (•). Stations of Rijkswaterstaat (Dutch Ministry of Infrastructure and Water Management) are sensors fixed to a reference: Hoek van Holland (HVH), Brienoordbrug (BRB), Krimpen aan den IJssel (KRY), and Kinderdijk (KD). In the Lek (LK), six sensors were deployed 1 m below the water surface, and in the Hollandsche IJssel (HY), five sensors were deployed 1 m above the river bed. Red crosses (×) indicate water level stations. The red lines indicate the two ship transects.

which both have low discharge from upstream during low discharge scenarios, are particularly vulnerable to salt intrusion. Figure 3.1a gives an overview of the estimated discharges for a low discharge scenario of the most important branches, based on 1D numerical simulations (Cox et al., 2021).

The entire Dutch river system is regularly dredged to maintain the navigation depth. The stretch of roughly 25 km of the waterway has a navigation depth of about  $-17$  m NAP (Normaal Amsterdams Peil). Upstream of the major harbour basins, the river is shallower and the depths decrease from  $-14$  m NAP to  $-5$  m NAP. The Hollandsche IJssel is a dammed-off river branch with a length of 20 km, an average water depth from  $-4$  to  $-4.5$  m NAP, and a channel width of 50-100 m (Rijkswaterstaat, 2024a). The Lek is part of the Rhine River and has a weir (Hagestein) at 42 km from its mouth (not shown in Figure 3.1). The average water depth and channel width of the Lek are  $-5.3$  m NAP and 180-330 m respectively (Rijkswaterstaat, 2024b). Water level and salinity data are monitored at the mouths of both branches, Krimpen a/d IJssel and Kinderdijk (KRY and KD, indicated by red crosses in Figure 3.1b). The total discharge through the branches depends on the upstream inputs (Hagestein for the Lek, Gouda (GD) for Hollandsche IJssel) and several water extraction locations along the branches (blue droplets in Figure 3.1b). Hereafter, the total discharge through those branches is therefore referred to as controlled discharge.

### 3.3.2 Instrumentation

We measure the salinity based on Conductivity, Temperature, Depth (CTD) sensors monitoring at 20 locations in the Rhine-Meuse Delta Estuary from 22 June to 19 October 2022. Most of these monitoring stations are permanent or seasonal stations of Rijkswaterstaat (Dutch Ministry of Infrastructure and Water Management), and three stations were installed for the purpose of this study.

We installed CTD sensors at the top and the bottom of the water column at four locations within the estuary. The sensors were attached to a fixed point on a quay wall at the Port of Rotterdam (PoR), and to a buoy at NM-A, and Eemhaven (EEM). Temporary sensors were also installed on a floating platform during the Maasdeltatunnel (MDT) construction by the BAAK consortium. Rijkswaterstaat deployed a salinity monitoring net in two rivers branching off the main channel: the Hollandsche IJssel (HY) and the Lek (LK). In the Lek, six sensors were installed 1 m below the water surface, and in the Hollandsche IJssel, five sensors were placed 1 m above the river bed. These depths were chosen because the water column is usually well-mixed in those branches, which was confirmed in our observations (e.g. Figure 3.3b). The remaining salinity data were retrieved from permanent measurement stations of Rijkswaterstaat, including Hoek van Holland (HVH), Brienoordbrug (BRB), Krimpen a/d IJssel (KI), and Kinderdijk (KD). The BRB station also has a 45-year time series, which is used to evaluate the drought of 2022 in terms of the historical record. All sensors and their locations are summarised in Table 3.1. Furthermore, two ship surveys were conducted to

gain insight into the along-channel salinity structure. During those surveys, we took vertical CTD casts in the thalweg every 1,000 m. The first survey was on the 1<sup>st</sup> of August in the Rotterdam Waterway. The second survey was partially in the New Meuse and the Hollandsche IJssel on the 4<sup>th</sup> of August.

The Rhine River discharge data at Lobith (Dutch reference location, see Figure 3.1a) were retrieved from the Rijkswaterstaat database, as well as the water level and astronomical tide at HVH. To obtain the set-up at HVH, the water level is filtered with a low-pass Godin filter (Godin, 1972). This filter is obtained by subsequently taking the convolution of two running means of 24 hours, and the convolution of this triangular filter with a running mean length of 25 hours. Data on wind speed, wind direction, and atmospheric pressure at HVH were retrieved from the Royal Dutch Meteorological Office (KNMI). The controlled discharges in the branches are a combination of discharge records of Rijkswaterstaat and waterboards.

To define the drought, we set a percentile threshold of 10% of the climatological discharge to identify a 'severe drought', based on NOAA's National Weather Service and methods (Hammond et al., 2022). We took a variable drought metric, the percentile threshold for every day of the year, based on a climatological baseline period of the years 1992-2021. We compare a 5-day means of the 2022 data against these thresholds.

### 3.3.3 Estimation of the salt intrusion length

To estimate the salt intrusion length ( $L_2$ ), defined here as the location of the 2 PSU isohaline, we use the near-bottom salinity sensors from the estuary. The salinity between the two sensors where the threshold value of 2 PSU is found is linearly interpolated to derive the salt intrusion length. The main channel (Rotterdam Waterway and New Meuse) branches off into the Hollandsche IJssel and the Lek, so a salinity intrusion length can be defined for each branch. For simplicity, the salt intrusion length in the Lek ( $L_2$ ) will be used in the main analysis. In the analysis of the side branches, we chose the 0.3 PSU isohaline, because the 2 PSU isohaline does not reach the branches often. These two different intrusion limits are defined to make a distinction between the side branches and the main system. In this study we only consider the Rhine discharge and not the Meuse discharge, because the contribution of the Meuse waters, which discharge into the North Sea through the Rotterdam Waterway is small compared to the Rhine River discharge. Lobith is chosen as a discharge reference because it represents the total Dutch Rhine discharge and an important reference location with a long-term record. To evaluate the effect of forcing conditions on the salt intrusion length, first, the time series at a frequency of 10 minutes, are shifted in time to obtain the highest correlation between the compared quantities. This step is taken to account for the travel time of the forcing into the estuary and a lag between the forcing and the salt intrusion response. Most lags were between 5 hours and 11 hours, and 10 days for the lag between salinity at BRB and salt intrusion length in the HY.

**Table 3.1:** Overview of measurement stations within the estuary.

Station	Distance from mouth [km]	Branch	Parameter
HVH	0	main	salinity (3 depths) water level
MDT	13.2	main	salinity (2 depths)
NM-A	18	main	salinity (2 depths)
EEM	22.2	main	salinity (2 depths)
PoR	28.5	main	salinity (2 depths)
BRB	35	main	salinity (2 depths)
KIJ	37	Hollandsche IJssel	salinity (2 depths) water level
HY1	44	Hollandsche IJssel	salinity (1 depth)
HY2	45.5	Hollandsche IJssel	salinity (1 depth)
HY3	48	Hollandsche IJssel	salinity (1 depth)
HY4	49.7	Hollandsche IJssel	salinity (1 depth)
HY5	52	Hollandsche IJssel	salinity (1 depth)
GD	52.5	Hollandsche IJssel	water level discharge
KD	41.2	Lek	salinity (1 depth) water level
LK1	43.3	Lek	salinity (1 depth)
LK2	45.8	Lek	salinity (1 depth)
LK3	47.8	Lek	salinity (1 depth)
LK5	52.2	Lek	salinity (1 depth)
LK6	79.5	Lek	salinity (1 depth)
SHV	78.5	Lek	water level
Hagestein	83	Lek	water level discharge

Hereafter, all time series are tidally averaged, to obtain one datapoint per tidal cycle.

## 3.4 Results

### 3.4.1 Forcing conditions

The forcing conditions during the study period are shown in Figure 3.2. The Rhine River discharge at Lobith  $Q_R$  varied between approximately 670 and 2100  $\text{m}^3 \text{s}^{-1}$  during the measurement period (Fig. 3.2a). In mid-August, we observed the lowest discharge in the 121 years of monitoring data, 673  $\text{m}^3 \text{s}^{-1}$  (yellow dot in Figure 3.2a). We can define this as a severe drought (below 10<sup>th</sup> percentile)

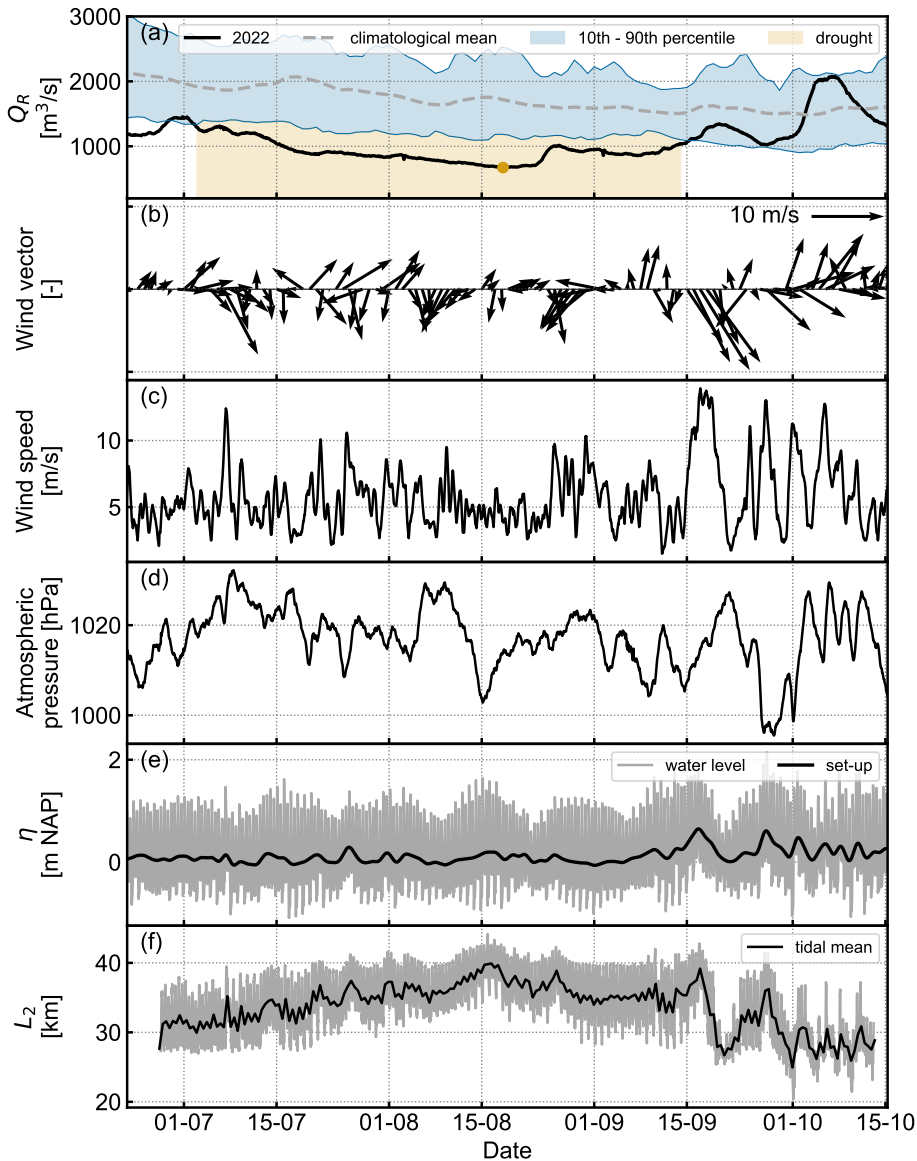


**Figure 3.2:** Forcing conditions and salt intrusion length between 13 June and 25 October 2022, including (a) the Rhine River discharge  $Q_R$ , showing the mean and 10<sup>th</sup>-90<sup>th</sup> percentile range for the climatological period (1992-2021) and period of severe drought, (b) the wind vector, (c) wind speed, and (e) atmospheric pressure at sea level at Hoek van Holland, (f) the measured water level  $\eta$  and calculated set-up ( $\langle \eta \rangle$ ) at Hoek van Holland, and (g) the salt intrusion length  $L_2$  in the Lek, defined as the 2 PSU isohaline.

that lasted for 75 days, highlighted by the yellow shaded area in Figure 3.2a.

Wind speeds were mainly low and moderate (between 3 and 8 m s<sup>-1</sup>) between June and August. In September and October, there were more frequent occurrences of winds above 10 m s<sup>-1</sup> (Fig. 3.2b), leading to set-up and set-down at the coast (Fig. 3.2d). Onshore winds (northwesterly) can drive an immediate coastal set-up, and a subsequent set-down when the wind relaxes. Along-shore winds can be upwelling-favourable (northeasterly), leading to set-down or downwelling-favourable (southwesterly), resulting in set-up.

There is no clear relationship between tidal range and salt intrusion length. However, there is a clear relation between the spring neap tidal cycle and stratification (expressed as buoyancy frequency  $N^2$ ) at the salinity stations along the estuary. Figure B.2 in Appendix B shows a stronger stratification a few days after neap tide, and a weaker stratification a few days after spring tide.

### 3.4.2 Stratification structure

The stratification of the estuary at the beginning of August 2022 is shown in Figure 3.3, based on ship-borne CTD measurements (see ship tracks in Figure 3.1b). Figure 3.3a shows the stratification in the Rotterdam Waterway, and Figure 3.3b shows the stratification in the New Meuse (22 km to 36 km from Hoek van Holland) and the Hollandsche IJssel (36 km to 42 km from Hoek van Holland). In the deeper, overdredged part of the estuary, there is a strongly stratified salt wedge. In the shallow Hollandsche IJssel side branch, the salinity structure is more well-mixed, and the horizontal salinity gradient is weaker than in the Rotterdam Waterway and the New Meuse.

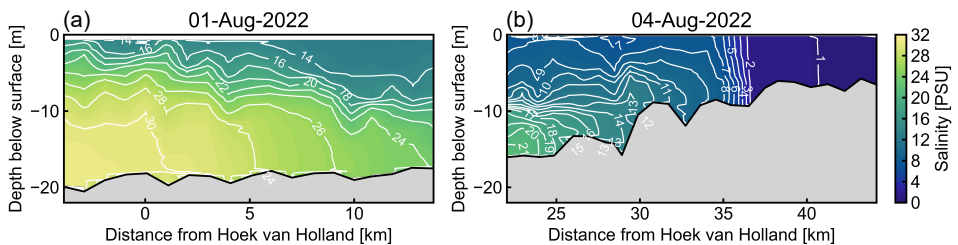


**Figure 3.3:** Along-channel salinity structure on flood tide (a) in the Rotterdam Waterway on the 1<sup>st</sup> of August 2022 and (b) in the New Meuse (22 km to 36 km) and Hollandsche IJssel (36 km to 42 km) on the 4<sup>th</sup> of August 2022

### 3.4.3 Salt intrusion length

Figure 3.2e shows the evolution of the salt intrusion length in the Lek ( $L_2$ ), defined as the location of the 2 PSU isohaline. The mean tidal variability is 8.5 km, and the greatest intrusion length was 44.2 km. This occurred on 16 August during a period of very low Rhine discharge of about 700 m<sup>3</sup> s<sup>-1</sup>, during a spring

tide when there was a small set-up at the coast (Fig. 3.2d). At this time the tidally averaged intrusion length was 39.9 km. The second largest salt intrusion event occurred in mid-September and had a tidally averaged length of 39.2 km. During this second event, the river discharge was larger than mid-August. However, there had been a prolonged north-westerly wind, leading to an increased wind set-up at the coast (Figs. 3.2b-d). The set-down afterwards also rapidly decreased the salt intrusion length. More events will be examined in section 3.4.5. During the period of low discharge without major set-up events, for example, between the 6<sup>th</sup> and the 15<sup>th</sup> of August, the landward propagation of the salt front was approximately 0.86 km/day. For the most extreme set-up event, the upstream propagation speed was 4.32 km/day.

### 3.4.4 The role of river discharge

The relation between the 5-day mean of the Rhine River discharge and the 5-day mean of the salt intrusion length  $L_2$  is shown in Figure 3.4a. Following a power law relation between river discharge  $Q_R$  and salt intrusion length  $L_2 \propto Q_R^{-n}$ , the observed values give the best fit for  $n = 0.35 \pm 0.03$ . This is larger than values found for other salt wedge estuaries, e.g.  $n = 0.2$  in the Duwamish River Estuary (McKeon et al., 2021) and  $n = 0.19$  in the Merrimack River Estuary (Ralston et al., 2010) for low discharge. For 5-day means, the Rhine River discharge explains  $88 \pm 5\%$  of the variance in intrusion length, but only  $69 \pm 3\%$  of the variance for tidal means. Most of the outliers of the tidal means can be explained by variability due to coastal set-up. The dependence of anomalies in the discharge relationship on coastal set-up is shown in Figure B.1b of Appendix B. Storm surge events act on a timescale of 1.5 to 6 days, which are mostly averaged out by a 5-day mean. The dependence of salt intrusion on coastal set-up is further discussed in section 3.4.5.

We show the salinity at Brienoordbrug and the Rhine River discharge between 1978 and 2022 for the summer months June, July, and August (JJA) in Figure 3.4b. The data points of the field campaign of 2022 are represented by blue circles. Most of the data points of 2022 are located in the yellow-shaded area, representing high salinity and low discharge, defined as severe drought conditions or worse ( $Q_R < 1180 \text{ m}^3 \text{ s}^{-1}$ , below 10<sup>th</sup> percentile). There is no power law dependence in the high discharge tail ( $Q_R > 2000 \text{ m}^3 \text{ s}^{-1}$ ). For high discharges, the salinity at Brienoordbrug reaches the background chloride concentration of the fresh river water, and the salt intrusion length does not reach beyond the observation point. This background salinity concentration  $s$  is dependent on the amount of discharge with  $s = a/Q_R + b$  (van der Weijden and Middelburg, 1989), where  $a$  is the chloride load and  $b$  the base chloride concentration, i.e. a constant background concentration. For the summer months between 1992 and 2022 we found  $s_{Lobith} = 100.58 \cdot Q_{Lobith}^{-1} + 0.094$ , indicated by the dashed line in Figure 3.4b. To show how exceptional the salinity levels recorded in 2022 were, we ranked the 5-day average salinity concentration since 1978 and found that 35 of

the top 100 records occurred in 2022.

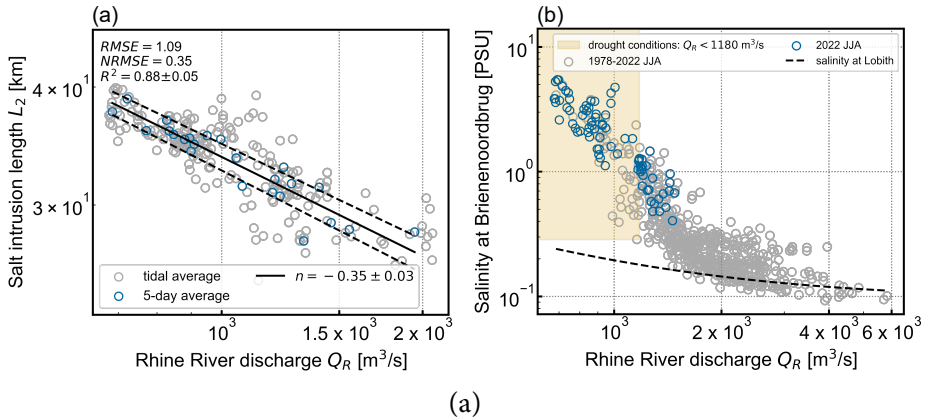


**Figure 3.4:** Discharge dependence of salinity, (a) Rhine River discharge  $Q_R$  versus salt intrusion length  $L_2$  for 5-day averaged values in blue and tidal averages in grey, the solid black line indicates the least-squares power law fit and the dashed lines indicate this fit  $\pm RMSE$ , and (b) Rhine River discharge  $Q_R$  versus salinity at Brienenoordbrug, 35 kilometres from the mouth between 1978 and 2022 for 5-day averaged values of the summer months (June, July, August). The yellow shaded area highlights severe droughts and worse (below 10<sup>th</sup> percentile), the dashed line indicates the calculated river salinity concentration at Lobith based on the discharge.

### 3.4.5 The role of wind and atmospheric forcing

Atmospheric forcing drives changes in atmospheric pressure, local wind, and remote wind. Variations in coastal set-up can be driven by changes in wind conditions and atmospheric pressure (Fig. 3.2). Atmospheric pressure drives variations in water level due to the inverted barometric effect (Wunsch and Stammer, 1997; Dangendorf et al., 2014). To evaluate the influence of coastal set-up on salt intrusion, we consider the subtidal water level at Hoek van Holland.

Estuaries are most susceptible to salt intrusion during periods of low discharge, and the corresponding dependency for the Rhine-Meuse Delta is shown in Figure 3.4a. The coastal set-up can cause perturbations landward or seaward from the expected location for a given discharge, as shown by the tidal averages in Figure 3.4a. Because the effect of coastal set-up on salt intrusion occurs over timescales of a few days, its importance is best shown by its influence on the speed of the intrusion ( $s_1$  in Equation 3.1). Figure 3.5 shows the dependence of the salinity intrusion speed  $\frac{dL_2}{dt}$  ( $\text{m s}^{-1}$ ) on the rate of change of the subtidal water level at the mouth  $\frac{d(\eta)}{dt}$  ( $\text{m s}^{-1}$ ). Here, positive intrusion speed represents landward movement. The gradients were based on low-pass filtered time series with time steps of 10 minutes. There is a strong correlation between those quantities, especially for increasing coastal set-up. The intrusion speed correlates with the rate of change of set-up, because those variations in coastal set-up can drive a

volume flux of ocean water up-estuary, as the water levels in the estuary adjust to the offshore water level Wong and Valle-Levinson (2002). These results indicate that the set-up is not a general predictor of the salt intrusion length but drives changes in the salt intrusion length on shorter timescales (1.5 to 6 days).

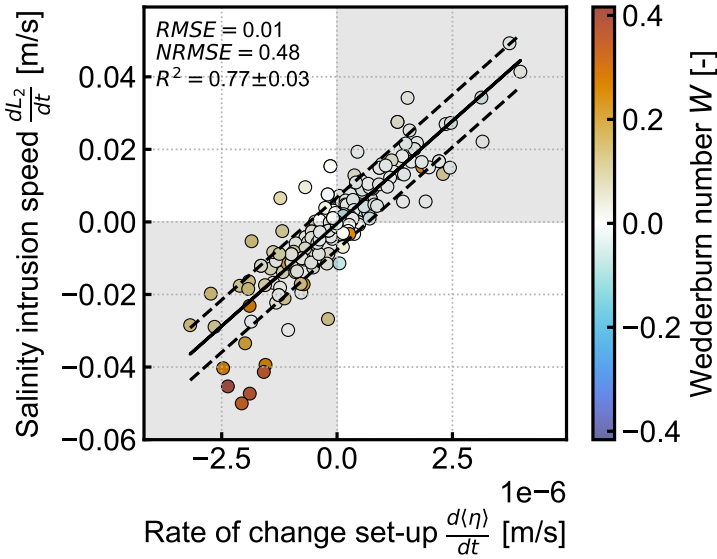


**Figure 3.5:** Coastal set-up dependence of salt intrusion length, showing the tidally averaged rate of change of subtidal water level at Hoek van Holland  $\frac{d(\eta)}{dt}$  versus salinity intrusion speed  $\frac{dL_2}{dt}$ , the black line indicates the least squares linear fit and the dashed lines indicate this fit  $\pm RMSE$ , the colours indicate the dimensionless Wedderburn number  $W$ , see Equation 3.2.

To describe the effect of local, along-estuary (northeasterly) winds on salt intrusion we evaluate the Wedderburn number  $W$ , a dimensionless number, defined as the ratio between the along-channel wind stress and the along-channel baroclinic pressure gradient (Geyer, 1997)

$$W = \frac{\tau_w L}{\Delta \rho g h^2}, \quad (3.2)$$

with along-channel wind stress (up-estuary is taken positive here)  $\tau_w$ , salt intrusion length  $L$ , the density difference between the mouth and the location of the salt intrusion limit  $\Delta \rho$ , gravitational acceleration  $g$ , and depth of the surface layer  $h$ . Wind stress can be estimated by  $\tau_w = C_d \rho_a U_{10} |U_{10}|$ , with the wind speed 10 metres above the surface  $U_{10}$ , the density of air  $\rho_a = 1.2 \text{ kg m}^{-3}$ , and the dimensionless drag coefficient  $C_d = 0.0015$  (Wilson, 1960). By means of the ship surveys, we estimated the surface layer depth to be 8 metres (Fig. 3.3a).

We found the primary driver of salt intrusion related to wind to be  $\frac{d(\eta)}{dt}$ , therefore coloured the dots in Figure 3.5 by their value of  $W$ . The outliers below the

RMSE in the relation between  $\frac{dL_2}{dt}$  and  $\frac{d\langle\eta\rangle}{dt}$  (Fig. 3.5) are associated with the highest values of  $W \approx 0.4$ , and correspond to a decreasing mean water level. These outliers correspond to the wind events on the 17<sup>th</sup> of September and the 27<sup>th</sup> of September (see the first two yellow highlighted events in Figure 3.6). For high  $W$ , the transport by estuarine circulation is reduced, which could result in a faster retreat of the salt intrusion, than the rate of change that is predicted by the fit of the data, based on the occurring set-down.

## 3

We further analyse the relation between  $L_2$  and  $\langle\eta\rangle$  by selecting the wind events above 0.15 m NAP (Fig. 3.6a and b). Those set-up events are indicated with blue dots for the maxima and green dots for minima in the set-up time series (Fig. 3.6a) and salt intrusion length time series (Fig. 3.6b). The maximum time lag between the maxima in set-up and salt intrusion length is 25 hours, and the mean is approximately 9 hours. Within one event,  $L_2$  can move up to 6.2 km upstream and up to 12.5 km downstream. This movement is approximately equal to the tidal excursion length, which is estimated to be 8.5 km. In most of the events, the increase in salt intrusion length during the set-up differs from the retreat in salt intrusion length during the set-down. In 11 of the 13 cases, the larger increase in salt intrusion than the decrease in salt intrusion corresponds to a larger set-up than set-down subtidal water level change, and vice versa. During these events  $L_2$  reaches a maximum event-averaged speed of  $0.086 \text{ m s}^{-1}$ , which is roughly twice the average freshwater flow speed in the New Meuse in summer.

We examine representative wind and set-up-driven salt intrusion events that occurred between the 17<sup>th</sup> of September and 10<sup>th</sup> October; these are highlighted in yellow in Figure 3.6. Two days of persistent strong onshore (northwesterly) winds preceded the salt intrusion event on September 17<sup>th</sup> (Figs. 3.6c-h). During these days, the coastal set-up at Hoek van Holland increased to 0.65 metres above NAP. The time lag between the maximum intrusion event of 39.2 km and the maximum set-up was approximately 4 hours. The intrusion length before the event was about 35.0 km. After the peak water levels and peak salt intrusion length, the subsequent set-down drove a downstream propagation of the salt front of 12.6 km, so it became shorter than before the intrusion event, namely 26.7 km. This relatively large decrease in intrusion length during the set-down can be explained by the strong up-estuary (also onshore) wind speed. These days had the largest observed Wedderburn number values (red dots in Figure 3.5), which indicates that the salt import by the gravitation circulation decreased during these days. Furthermore, the Rhine River discharge increased during this event as well.

In October, we observed a series of salt intrusion events driven by coastal set-up. The time series in Figure 3.6e and f show that fluctuations in wind speed and atmospheric pressure are in phase with the coastal set-up. The wind speed has a positive correlation and the atmospheric pressure has a negative correlation with set-up. Figure 3.6d shows that most of the time we observed direct onshore (northwesterly) winds or downwelling (southwesterly) winds. Both onshore and downwelling winds can drive a set-up at the coast. The longest tidally averaged intrusion length was 36.6 km and the maximum set-up was 0.64 m. The time lag

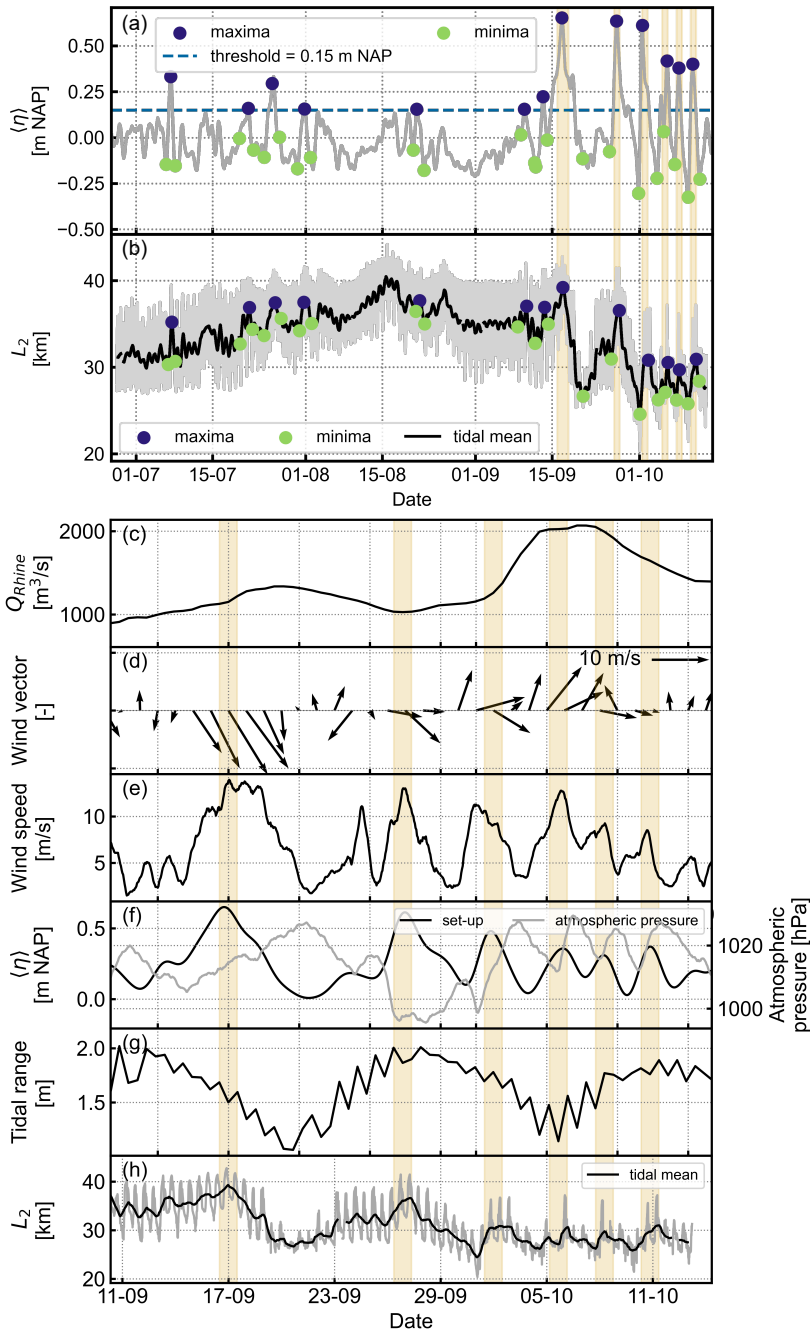


**Figure 3.6:** Overview of the selected coastal set-up events, including (a) coastal set-up at Hoek van Holland ( $\eta$ ), (b) salt intrusion length  $L_2$ . The yellow highlighted events are zoomed in upon with additional parameters. (c) Rhine River discharge  $Q_{Rhine}$ , (d) the daily mean wind vector, (e)  $\langle \eta \rangle$  and atmospheric pressure at Hoek van Holland, (f) the tidal range at Hoek van Holland, and (g)  $L_2$ . The yellow areas highlight 48 hours around the maximum set-up.

between the set-up peaks and salt intrusion peaks varied from 2 to 26 hours.

### 3.4.6 Side branches

In this section, the Lek and the Hollandsche IJssel, are studied in more detail, because the dynamics in those branches differ from the main river stem (Kranenburg et al., 2022). Those differences are mainly caused by their geometry and because local water management has a bigger impact. They can be thought of as subestuaries within the larger delta channel network.

As a result of the difference in length between the two branches, tidal flows in the branches have a different phasing with respect to flow velocity to the New Meuse. The Hollandsche IJssel is shorter than the Lek and has a standing tidal wave, whereas the main channel and the Lek have a propagating tidal wave. Figure 3.7c shows that the water level at Gouda and KRY are in phase, which indicates a standing wave. Contrastingly, the phase difference between water levels at KRY and SHV indicates a propagating tidal wave in the Lek (Fig. 3.7a). The main channel has a phase difference in flow velocity of  $55^\circ$  with the Hollandsche IJssel and  $31^\circ$  with the Lek (de Wilde, 2024). As a result, the Hollandsche IJssel has ebb flow for a long time when the main channel is flooding.

To further evaluate the difference in dynamics, we look at the evolution of the tidally averaged salinity contours together with the discharge through the branch, the set-up at Hoek van Holland, and the Rhine River discharge for the two different river branches in Figure 3.8 and 3.9. The discharge through the branches is human-controlled and consists of a summation of inlets and discharging stations. At those stations, freshwater can be extracted from or discharged into the branch. Figure 3.8b and 3.9b indicate whether there is a net extraction ( $Q_{branch} < 0 \text{ m}^3 \text{ s}^{-1}$ ) or a net discharge ( $Q_{branch} > 0 \text{ m}^3 \text{ s}^{-1}$ ) in the branch.

The longest tidally averaged intrusion lengths  $L_{0,3}$  in the two branches were observed in different months. In the Lek, an intrusion length  $L_{0,3}$  of 48.6 km occurred on the 17<sup>th</sup> of August. In the Hollandsche IJssel, a salt intrusion length of 50.5 km was observed a month later, on the 24<sup>th</sup> of September.

In the Lek,  $L_{0,3}$  follows a temporal pattern closely related to the salinity at its mouth (41 km), see Figure 3.8. Roughly between 7<sup>th</sup> and 15<sup>th</sup> August, there is a net negative discharge, the set-up at Hoek van Holland is slightly decreasing, and the Rhine River discharge is decreasing. This results in increasing salinities in the Lek, where a peak is reached on August 17<sup>th</sup>. On August 15<sup>th</sup>, the weir at Hagestein (upstream control of the Lek) was opened to flush out saline water from the branch. This increased net discharge ( $Q_{Lek} > 0 \text{ m}^3 \text{ s}^{-1}$ ), combined with a slight set-down, which decreases salinity at the Lek mouth, reduced the salt intrusion length. Later, we also observe a strong response of the salt intrusion in the branch to the set-up at Hoek van Holland. The clearest examples occur around 17<sup>th</sup> and 26<sup>th</sup> September when the Rhine discharge is still around  $1,000 \text{ m}^3 \text{ s}^{-1}$ .

Interestingly,  $L_{0,3}$  of the Hollandsche IJssel shows less correlation with the salinity at the mouth of the branch. The low salinity limit does not follow a sim-

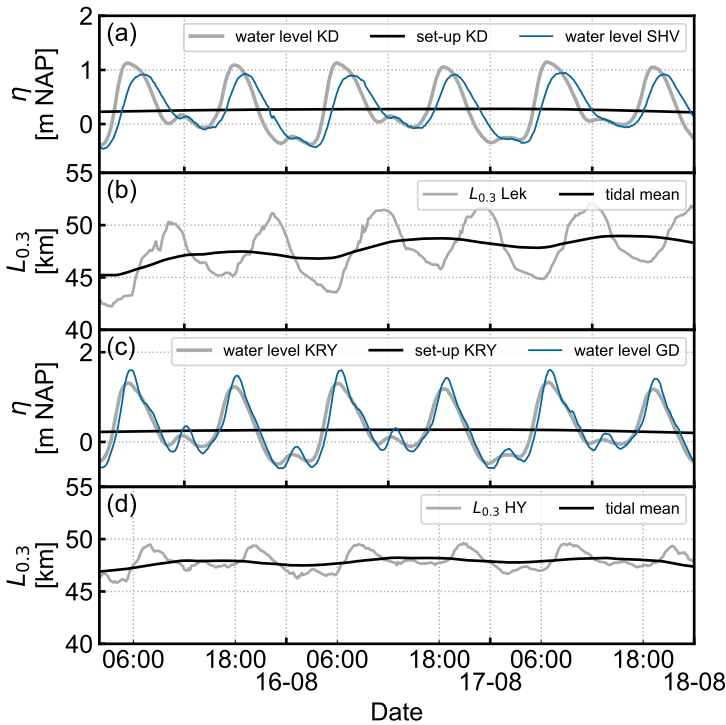


**Figure 3.7:** The time series of (a,c) water level  $\eta$  at the mouth and upstream control of the river branch, and (b,d) salt intrusion length  $L_{0.3}$ . Here panels (a,b) correspond to the Lek branch, and panels (c,d) to the Hollandsche IJssel branch.

ilar pattern as the salinity at the mouth of the branch (36 km). The value of  $L_{0.3}$  remains between 46 and 48 km from 14<sup>th</sup> August up to the 17<sup>th</sup> of September. Between 6<sup>th</sup> and 10<sup>th</sup> of September, there is a slight increase in discharge through the branch, with a corresponding decrease in salt intrusion length. This decrease in  $L_{0.3}$  is followed by an increase due to the set-up event around the 16<sup>th</sup> of September.  $L_2$ , which is located around the mouth of the Hollandsche IJssel during this period, propagates upstream and downstream with the corresponding set-up and set-down. However, there is no strong response of  $L_{0.3}$  to the set-down. The reduction in salinity intrusion length  $L_{0.3}$  started only after September 26<sup>th</sup>, coinciding with a significant increase in discharge from the Hollandsche IJssel. This increase in discharge coincides with a strong set-up at Hoek van Holland, which eventually flushes out all salinity above 0.3 PSU on the subsequent set-down. The set-up events in October, associated with up-estuary salt transport, drive  $L_{0.3}$  into the branch again. However, there are no major intrusions anymore, since the Rhine discharge has started to increase again.

The difference in the evolution of  $L_{0.3}$  between the two branches is caused by the tidal phase difference between the two branches. The Hollandsche IJssel has

an earlier flow reversal; therefore, there is ebb flow in the branch while the New Meuse is at the end of flood tide, with corresponding high salinity concentrations. This is shown in Figure 3.7b and d by the small intratidal variability in salt intrusion length compared to the Lek. Once the Hollandsche IJssel becomes saline, the salt concentrations stay in the branch for a relatively long time (Fig. 3.9a).

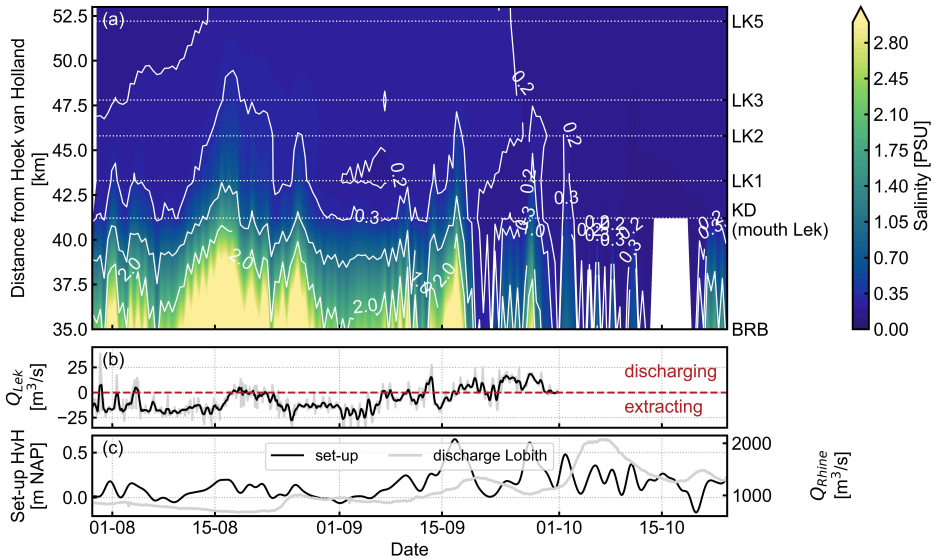


**Figure 3.8:** (a) Salinity contours in the New Meuse and Lek, between salinity stations BRB and LK5. The salinity values are interpolated between the stations, whose locations are indicated by white dotted lines. (b) Discharge through the Lek  $Q_{Lek}$ , where positive values represent a net freshwater discharge on the Lek and negative values net extractions from the Lek. (c) Set-up ( $\eta$ ) at Hoek van Holland and Rhine River discharge  $Q_{Rhine}$ .

Unlike in the main branch, the salt intrusion length in the side branches is most strongly correlated with downstream salinity in the main stem, which is at Brienenoordbrug (35 km) (Fig. 3.10), rather than discharge through the branch (Fig. B.3 in Appendix B). Here, we evaluated 3-day averages for salinity and salt intrusion, to consider the estimated average response times. The estimated response times  $T_{ADJ} = \frac{1}{2} \frac{L_b}{\bar{u}}$  (MacCready, 2007; Lerczak et al., 2009) for the Lek branch was 3 to 4 days, and for the Hollandsche IJssel it was 15 days. The stronger dependence on downstream salinity than other factors is due to a combination of significant salinity changes at the downstream boundary and a weak horizontal salinity gradient in the branches. At Brienenoordbrug the tidal average salinity varies between 0 and 6 PSU, so the salinity varies over more than an order of magnitude, whereas the salinity at the mouth of the main system is expected to vary with only roughly 10% (Lee and Lwiza, 2008; Schloen et al., 2017; Salcedo-Castro et al., 2023). When the downstream salinity increases, the horizontal salinity gradient increases, and the tidal dispersion term also increases. We consider the downstream salinity as a separate forcing because the side branches are decou-

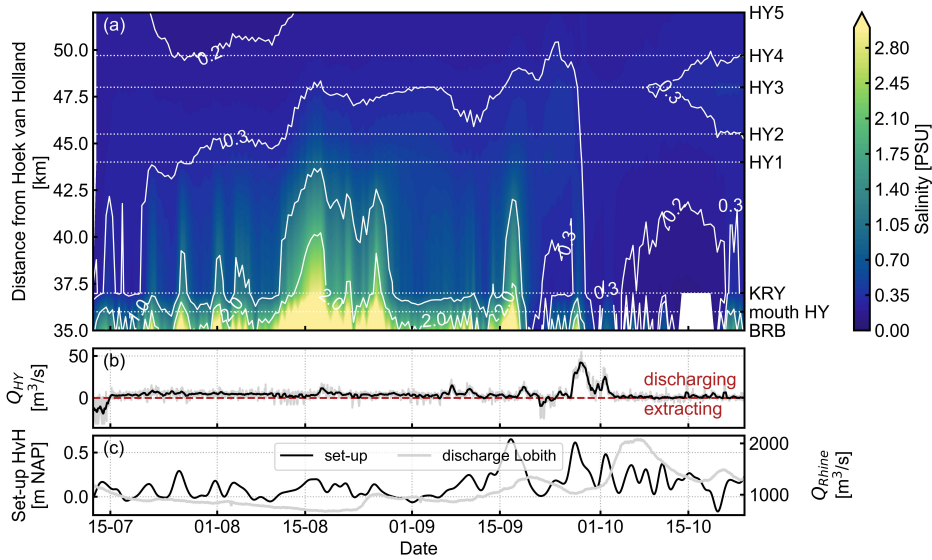


**Figure 3.9:** (a) Salinity contours in the New Meuse and Hollandsche IJssel, between salinity stations BRB and HY5. The salinity values are interpolated between the stations, whose locations are indicated by white dotted lines. (b) Discharge through the Hollandsche IJssel  $Q_{HY}$ , where positive values represent a net freshwater discharge on the Hollandsche IJssel (HY), and negative values represent net extractions from the Hollandsche IJssel. (c) Set-up  $\langle \eta \rangle$  at Hoek van Holland and Rhine River discharge  $Q_{Rhine}$ .

pled from this downstream end; they have different tidal phasing and discharge compared to the main branch.

However, two other important forcing mechanisms act on shorter timescales, thus influencing the salinity intrusion speed. For the Hollandsche IJssel, the net discharge through the branch explains 49% of the variance and is a good predictor for the rate of change of salt intrusion (Fig. 3.11b). In the Lek, the rate of change of salt intrusion is more dependent on the rate of change of set-up at the mouth (Figs. 3.11a and c), which explains 60% of the variance. The relation between salt intrusion speed and discharge in the Lek (Fig. 3.11a) contains many outliers, where the high outliers correspond to a strongly increasing subtidal water level and the low outliers correspond to a strongly decreasing subtidal water level. Similarly, in the relation between the rate of change of set-up and the salinity intrusion speed of the Hollandsche IJssel, the high outliers correspond to low net discharges in the Hollandsche IJssel, and low outliers to high net discharges. The effect of the discharge can be explained by 'sucking and flushing', where the saline water is sucked in during periods of negative discharge (lower left shaded area in Figure 3.11a and b), and flushed out for positive net discharges (upper right shaded area in Figure 3.11a and b). Here the rate of change of salinity intrusion speed scales with the freshwater flow velocity  $u_R$  as  $\frac{dL}{dt} \propto -Q_{branch}/A$ , with the cross-sectional area of the river  $A$ . This relation was confirmed for the

Hollandsche IJssel for another period as well (Kuijper, 2016). We can explain this relation by looking at the balance of the terms by considering the depth-averaged, width-averaged, tidally averaged, salt conservation balance (Equation 3.1), which we introduced in section 3.2.

The observed balance between the unsteadiness term and advection by river discharge can hold when changes in river discharge have a negligible effect on the exchange flow term. In this case, the exchange flow term  $s_3$  should become negligible relative to the diffusion term  $s_4$  and the balance in Equation 3.1 then reduces to an advection-diffusion equation. When  $s_4 \ll s_2$ , the scaling between discharge and salt intrusion length is only found in terms  $s_1$  and  $s_2$ , which gives  $\frac{dL}{dt} \propto -\frac{Q}{A}$ . Due to the occurrence of negative discharges,  $s_2$  can be both positive and negative in the side branches. Therefore, the balance between  $s_1$  and  $s_2$  can hold here for a longer time than regular estuaries, where  $s_2$  only results in salt export by river flow.

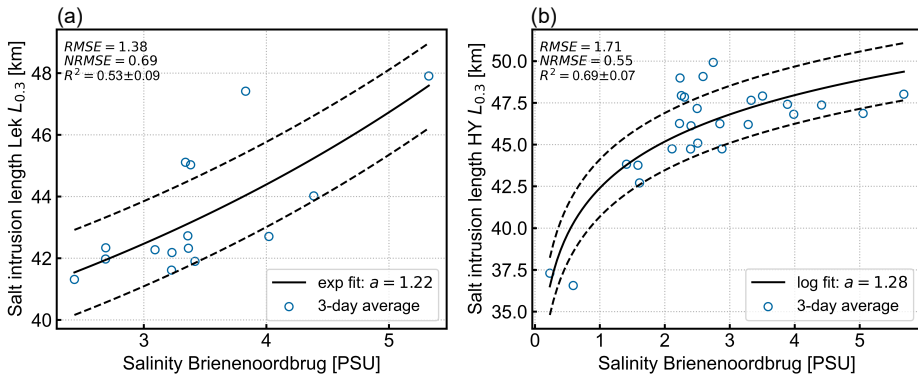


**Figure 3.10:** Salt intrusion length  $L_{0.3}$  versus salinity at the nearest downstream station, Brienoordbrug, 35 km from Hoek van Holland for 3-day averages (a) in the Lek and (b) in the Hollandsche IJssel (HY). The black line indicates the empirical least-squares fit and the dashed lines  $\pm RMSE$  of this fit.

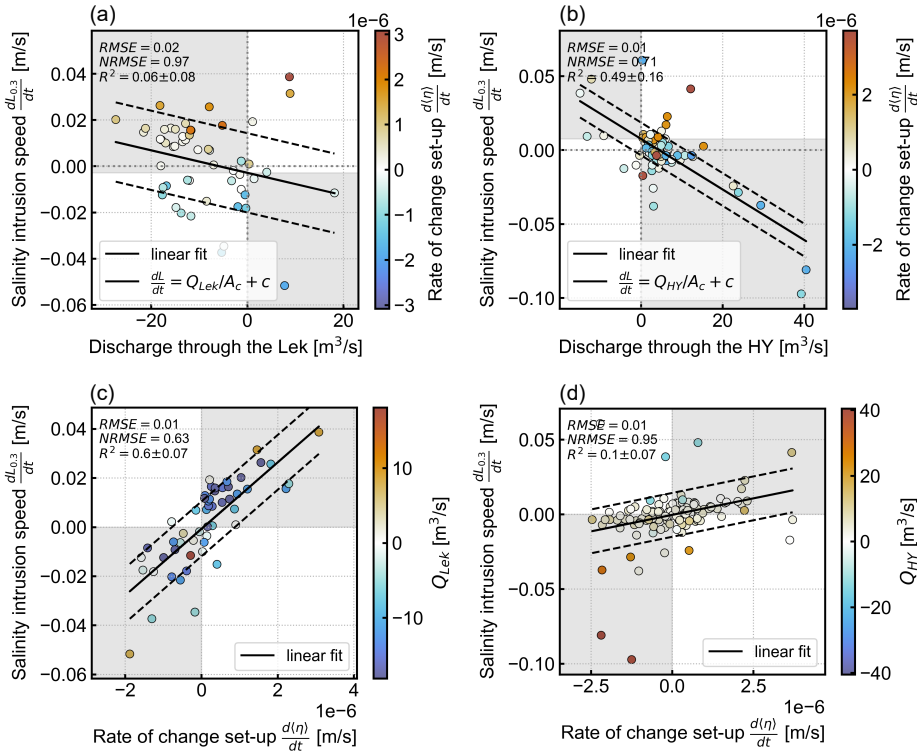


**Figure 3.11:** Salinity intrusion speed of  $L_{0,3}$  versus discharge through the mouth of the river branch  $Q_{branch}$  (a, b) and on rate of change of set-up  $\frac{d(\eta)}{dt}$  (c, d) in the Lek branch (left column) and Hollandsche IJssel branch (right column). In (a) and (b) the colours of the dots indicate the rate of change of set-up at Hoek van Holland. In (c) and (d) the colours of the dots indicate the discharge through the branch. The black lines indicate the least-squares linear fit and the dashed lines this fit  $\pm RMSE$ . The gray areas represent the offset from zero salinity intrusion speed.

### 3.5 Discussion

We studied salt intrusion during low discharge conditions, when estuaries are most susceptible to salt intrusion events. The Rhine-Meuse Delta shows a power law relation between salt intrusion length and discharge for 5-day averages. On shorter timescales (e.g. a couple of tidal cycles), coastal set-up drives fluctuations comparable to the tidal excursion length. However, tides do not appear to affect the subtidal salt intrusion. Conversely, in the side branches with a human-controlled discharge, the primary driver of the salt intrusion length was downstream salinity. This is different from most estuaries studied because ocean salinity at the estuary mouth is usually relatively constant. On shorter timescales, shown by the dependence on salinity intrusion speed, the coastal set-up and discharge played a role in determining salt intrusion dynamics.

Here, we show a power law relation between salt intrusion length and discharge with an exponent of  $n = 0.35 \pm 0.03$ . Close values can be found for both salt wedge estuaries, for example, the Merrimack and the Duwamish  $n \approx 0.2$  (Ralston et al., 2010; McKeon et al., 2021) and partially to well-mixed estuaries, for instance, the Delaware Bay and Hudson River estuary  $n \approx 0.3 - 0.4$  (Cook et al., 2023; Abood, 1974). Theoretical models predict exponents of  $n = 1/3$  for estuaries dominated by exchange flow (e.g., Hansen and Rattray, 1965; MacCready, 2004),  $n = 1$  for estuaries dominated by tidal salt fluxes (MacCready, 2007; Lerczak et al., 2009), and  $n = 2$  for arrested salt wedges (Schijf and Schönfeld, 1953). However, results from field observations often differ due to factors like unsteadiness and the presence of branching channel networks (Conroy et al., 2020), and along-estuary bathymetry variation (Ralston et al., 2008). Furthermore, Poggioli and Horner-Devine (2015) showed that a sloping bottom and channel convergence reduced the expected exponent for salt wedge estuaries. This exponent highlights the sensitivity of the estuary to changes in river discharge and the relative importance of other processes. In the Rhine-Meuse Delta, the observed value suggests that additional factors, such as unsteadiness from coastal set-up and the complex channel system, also play a significant role.

Unlike the main system, the relation between salt intrusion in the side branches and their discharge does not follow a power law. In the side branches, there is no steady-state balance with the discharge, but discharge drives variations on shorter timescales, which impacts the salinity intrusion speed. The salt balance is dominated by unsteadiness and advection, which means the relation between salt intrusion and discharge is described by  $\frac{dL_{0.3}}{dt} \propto -\frac{Q}{A}$ . This holds when the exchange flow term ( $s_3$  in Equation 3.1) is small. In the side branches, the exchange flow is expected to be weak, because the horizontal salinity gradient  $\frac{\partial \bar{s}}{\partial x}$  is weak, as there is a weak vertical stratification, and the side branches are shallower than the main system (Fig. 3.3). The unsteadiness term is expected to be relatively important here because there are many sudden changes in discharge. The sudden changes in discharges in the branches happen because they are determined by extraction locations, rather than a natural river basin source, as in the main branch. For unmanaged estuaries, this balance cannot hold for a long time because sudden increases in discharge would flush out most of the saline waters. In this highly managed system, this balance can persist for a longer time, because the river advection can become a source of salt import, due to the negative discharges.

Another difference between the main branch and the side branches was the importance of downstream salinity variation for salt intrusion length in the side branches. This importance could be attributed to the small salinity gradient in these regions, along with the potential importance of the tidal dispersion and advection terms relative to the estuarine exchange term. When the salinity at the mouth of the side branches doubles, the along-channel salinity gradient, and subsequently, the tidal dispersion flux double. We assume this is one of the dominant terms; therefore, the intrusion length responds strongly. For most estuaries, the variability in salinity at the mouth, due to upwelling or seasonal trends is rela-

tively minor, generally within a few PSU (around 5-10% of an approximate of 30 PSU) (Lee and Lwiza, 2008; Schloen et al., 2017; Salcedo-Castro et al., 2023). In contrast, the branches of the estuary experience much greater salinity variation, often exceeding 100% relative to their mean values. Consequently, regular changes in sea salinity could not impact the horizontal salinity gradient, and subsequent change in salt intrusion length as much as they can in the side branches. For multiple-channel systems, however, the ocean boundary can be more variable, due to the presence of several freshwater sources (e.g., Zhang et al., 2012; Korotenko et al., 2014).

Similar to many observations in estuaries (e.g., Wong and Garvine, 1984; de Nijs et al., 2008; Zhu et al., 2020; Eslami et al., 2021a; Cook et al., 2023), we found a strong relation between coastal set-up and salinity in the estuary. Wong and Valle-Levinson (2002) showed that the up-estuary volume flux  $Q_{in}$  associated with the changing subtidal water level can be estimated by  $Q_{in} = \frac{\partial \langle \eta \rangle}{\partial t} A_s$  in Chesapeake Bay. Here,  $\langle \eta \rangle$  is the subtidal water level and  $A_s$  is the surface area of the estuary. We showed that the rate of change of the salt intrusion length also scales with  $\frac{\partial \langle \eta \rangle}{\partial t}$  in the Rhine-Meuse Delta Estuary. This strong response to salt intrusion suggests the presence of a strong landward salt transport during coastal set-up events, which was seen in some numerical studies of the Rhine-Meuse Delta (Cox et al., 2021; Kranenburg et al., 2022).

While the effect of coastal set-up on salt intrusion is evident throughout the measurement campaign, the influence of along-estuary winds is only clear for the highest observed Wedderburn numbers around 0.4, which occurred during two wind events. Along-estuary winds were found to be important in several estuaries (Geyer, 1997; Scully et al., 2005; Cook et al., 2023). In deeper systems like the Delaware River Estuary (Cook et al., 2023) and the Rhine-Meuse Delta Estuary, high wind speeds are necessary to generate a response, as opposed to the shallow estuaries in Waquoit Bay, Cape Cod, described by Geyer (1997).

Similar to our observations in the Rotterdam Waterway, many estuaries have a distinct spring-neap variation in stratification (e.g., Lewis and Lewis, 1983; Stacey et al., 2001; Jay and Dungan Smith, 1990; Bowen and Geyer, 2003; Giddings et al., 2011), as well as a spring-neap variability in the strength of gravitation circulation (Eslami et al., 2021a). This variability could be attributed to the amount of mixing (Geyer et al., 2000; Lerczak et al., 2006). However, no correlation was found between the tidal range and salt intrusion length in the Rhine-Meuse Delta Estuary. This could be due to a large response time that increases during low river discharge, as was observed in the Hudson River Estuary (Bowen and Geyer, 2003; Lerczak et al., 2009). The estimated response times for the main system and the Lek branch are 3 to 4 days, and for the Hollandsche IJssel, it was approximately 15 days. With these response timescales, it is possible that the salt intrusion length cannot fully adjust to the changing tidal velocities within a spring-neap cycle. Another explanation could be that both the salt flux due to estuarine circulation and the salt flux by tidal dispersion processes vary on a fortnightly timescale. Fluxes by estuarine exchange flow are expected to be at a maximum around neap tides

and a minimum around spring tides, whereas it is the other way around for the tidal dispersion processes. If the salt fluxes from these mechanisms are of similar magnitude, their net effect on the total salt flux and the resulting spring-neap variations in salt intrusion length will be negligible. This is consistent with a recent numerical study of this system by Huismans et al. (2024).

In the Rhine-Meuse Delta, we observed that discharge is a dominant control of the salt intrusion, both in the main system and the side branches. The power law relation holds best for salinity and discharge values of timescales longer than a single tidal cycle, especially 5-day averages. Set-up, which acts on a shorter timescale is not described in such a balance. However, during drought, elevated salinity levels for a few days can have an impact on freshwater availability. Results of the Rhine-Meuse Delta indicate that adjusting the advection term  $\bar{u}\bar{s}$  by substituting  $\bar{u} = (Q_R + Q_{in}) / A$ , similar to Ralston et al. (2008), could be relevant for predictions based on MacCready (2004). This indicates that estuaries with a large surface area  $A_s$  are particularly susceptible to coastal set-up-driven salt intrusion. Gerritsma et al. (2025) showed that water levels in the semi-enclosed Haringvliet also adjust by water that flows through the Rotterdam Waterway, which contributes to the Rhine-Meuse estuary's susceptibility to coastal set-up variations.

River deltas are characterised by a branching channel network with varying channel geometries and bathymetries. This results in a heterogeneous distribution of river discharge and introduces tidal phasing, which are both of major importance for estuarine dynamics. Urban deltas are even more complex because they can exhibit more abrupt depth changes due to dredging activities and independent discharges resulting from flow management. This can lead to very different dynamics in the various branches of the estuary, where different balances dominate. This shows that when studying an integrated operational system for short-term emergency measures during droughts, it is important to be aware that not all branches within the system respond identically to forcing. Through first-order statistical analyses, we showed that treating the side branches separately is crucial in this complex urban delta. While the variability in the downstream salinity boundary is usually not considered in estuaries, we showed the importance of considering this parameter. Treating branches separately is a method to incorporate the downstream boundary condition variability, and may be applied in other deltas or complex estuaries.

### 3.6 Conclusions

Using an extensive data set we analysed salt intrusion in the Rhine-Meuse Delta during extremely low discharge conditions. Here, the salt intrusion length  $L_2$  follows a strong power law relation with the river discharge with  $Q_R^{-0.35 \pm 0.03}$ . Coastal set-up modifies this dependence on river discharge, where positive anomalies correspond to set-up, and negative anomalies to set-down. This can be at-

tributed to the up-estuary transport of seawater, which results from the estuary's adjustment to changing water levels at its mouth. The tidal range does not correlate with salt intrusion length. However, there is a relation between tidal range and stratification, which increases during neap tides and decreases during spring tides.

We showed that the overall system dynamics still behave like a simple system, but the side branches must be understood independently. River discharge and coastal set-up determine the overall response of the system, which is relevant because the salinity at the mouth of the upstream branches is the primary predictor for salt intrusion length. Additionally, the localised system dynamics, driven by set-up and discharge through each branch are important, and can differ per branch. Although we have shown that salinity at the mouth mainly drives the salinity intrusion, the relationship to discharge differs significantly from the main branch. A necessary next step is to obtain a more detailed understanding of the behaviour of the individual branches.

Understanding salt intrusion dynamics is important in a changing climate. This data set, collected during a severe drought, is crucial for understanding estuaries for which a decreasing discharge and increasing salt intrusion is projected (Lee et al., 2024). Besides the important role of discharge, we show that the coastal set-up can drive major fluctuations in salinity intrusion on shorter timescales. Importantly, this means that while discharge is critical for predicting the potential for salinity at upriver locations, coastal set-up may be most important for generating the most severe events during a low discharge period. The dynamics in the side branches can be very different from the main river branch; this indicates that potential different dynamics in side branches have to be well understood and validated to perform high-resolution predictions.



# 4

## Influences of tides and winds on estuarine inflow conditions

### Key points

- Variations in near-field bottom salinity and the estuarine inflow are driven by mid-field plume mixing.
- Upwelling- and downwelling-favourable winds cause plume advection, while they do not significantly affect near-field bottom salinity.
- Near-field bottom salinity correlates with salinity stations in the downstream section of the estuary and along-estuary salinity gradient.

## Abstract

This chapter investigates how wind and tides modulate flow and salinity near a river mouth, setting the dynamic seaward boundary for estuarine salt intrusion. Using near-field observations from the Rhine–Meuse plume, we focus on the lower layer that determines the salinity of the estuarine inflow. Near-field bottom salinity variability is primarily governed by tidal amplitude, with a 2.5-day lag, suggesting that tidal mixing of plume waters into the lower layer in the mid-field governs the lower-layer salinity variation in the near-field. Analogous to estuarine mixing controlling outflow salinity, plume mixing determines the salinity of inflowing waters. While wind-driven mixing has a minimal overall effect, isolated high-wind events (winds exceeding  $10 \text{ m s}^{-1}$ ) show a decrease in bottom salinity. Wind-driven transport by upwelling- and downwelling-favourable wind shows no statistically significant impact on bottom salinity, but it does alter the near-field velocity. Onshore winds affect salinity in the estuary due to coastal set-up and associated advection. Near-field bottom salinity correlates with salinity up to 27 km into the estuary, with diminishing influence upstream where river discharge dominates, suggesting that near-field conditions modulate the along-estuary salinity gradient and the exchange flow. Our results support a conceptual picture of the processes influencing the lower-layer salinity at the river mouth and, thus, the seaward boundary condition for estuarine salinity intrusion. Fresh river water is exported in the plume, mixed into the lower layer, and partly returned to the mouth, where it sets the inflow salinity. Strong cross-shore tidal straining in the Rhine River plume causes this returning freshwater to overshoot the mouth, creating a more complex return pathway compared to less strongly strained systems.

## 4.1 Introduction

Understanding and predicting salt intrusion is critical for managing freshwater resources in estuarine regions. During dry periods, saline water can extend upstream into regions that are usually fresh. This threatens freshwater availability for drinking water production, agriculture, and industry. When freshwater demand is close to available supply in densely populated deltas, changes in salinity intrusion on the order of kilometres can have significant societal and ecological impacts.

Salt intrusion into estuaries is governed by a combination of internal estuarine processes and external oceanic and riverine forcing. Winds, tides, and river discharge influence oceanic salinity, water levels, and net flow at the river mouth. These three variables represent the dynamical boundary conditions of the coupled estuary–coastal system, hereafter referred to as the estuarine inflow conditions.

However, growing evidence suggests that interactions between the coastal and river plume dynamics and the estuary can significantly influence estuarine dynamics (e.g., Hickey et al., 2002; Giddings and MacCready, 2017; Ralston et al., 2024). While decades of study have sought to understand the fate of river water discharged into the coastal ocean (e.g., Garvine, 1995; Simpson and Souza, 1995; Fong and Geyer, 2001; Nash et al., 2009; Horner-Devine et al., 2015) much less is known about the processes governing the inflow of saline water into estuaries (Brasseale and MacCready, 2021, 2025). Below, we summarise the prior work that considers how wind and tide influence the estuarine inflow conditions, and how these conditions influence salt intrusion.

Ocean salinity serves as a crucial boundary condition that sets the potential for salt intrusion (Schijf and Schönfeld, 1953; Poggioli and Horner-Devine, 2015). Using an idealised two-layer model, Poggioli and Horner-Devine (2015) found that the salinity at the mouth of the estuary affected the subsequent salt intrusion back into the estuary. Long-term observations in Chesapeake Bay have also shown that bottom salinity in the Bay is influenced by the shelf-slope water, which can be sourced from cold and fresh Labrador Sea waters or warm and saline Gulf Stream waters (Lee and Lwiza, 2008). Hence, understanding the processes that set the offshore salinity is important for understanding salt intrusion.

In addition to ocean salinity, subtidal fluctuations in coastal sea level have been shown to modulate salt intrusion length significantly. Elevated offshore water levels can enhance landward transport of saline water, while lower sea levels suppress it. This influence of subtidal sea level variability has been demonstrated through both observations and modelling studies (Wong and Valle-Levinson, 2002; de Nijs et al., 2008; Ralston et al., 2008; Manca et al., 2014; Perales-Valdivia et al., 2018; Zhu et al., 2020; Cook et al., 2023; Gerritsma et al., 2025).

Wind forcing on the continental shelf can also drive substantial changes in estuarine circulation and salinity structure. Observations from Willapa Bay, a small

estuary adjacent to a narrow and steep continental shelf, indicate that coastal upwelling and downwelling events play a key role in modifying the estuarine boundary conditions and, consequently, the horizontal density gradients (Hickey et al., 2002). Similarly, in the Columbia River estuary, field measurements have shown that variations in salt intrusion can occur in response to wind-driven upwelling and downwelling, largely through changes in ocean salinity and stratification (Chawla et al., 2008). This was further substantiated with a numerical modelling study by Brasseale and MacCready (2025), which showed that upwelling-favourable winds led to inflow of denser and deeper inflow sources. Giddings and MacCready (2017) demonstrated that upwelling winds strengthen estuarine exchange flow, whereas downwelling winds can weaken or even reverse it. These effects are primarily due to variations in both baroclinic and barotropic pressure gradients.

Alongshore winds, which induce cross-shore Ekman transport, are known to influence plume structure and propagation (Fong et al., 1997; Fong and Geyer, 2001; Lentz, 2004; Whitney and Garvine, 2005). These plume dynamics can influence estuarine salinity. For example, studies of the Columbia River plume have shown that under downwelling-favourable winds, the plume is pushed against the coast and low-salinity water can advect into adjacent systems such as Willapa Bay, Grays Harbor, and the Strait of Juan de Fuca (Hickey and Banas, 2003). Winds have further been shown to influence the formation and maintenance of salt plugs (Juarez et al., 2020, 2022).

Because the direction of the alongshore wind controls both the propagation and structure of the river plume, it also regulates the extent to which remnants of the previous plume are transported back into the estuary during the subsequent tidal cycle. Furthermore, a study of the Mobile Bay plume showed that the ambient salinity changes due to alongshore winds influence the buoyancy anomaly by altering salinity in the estuary and offshore, which enhances the Ekman-induced transport of the plume for upwelling winds. In contrast, downwelling winds reduce the buoyancy anomaly (Ralston et al., 2024).

The "near-field region", defined here as the coastal area within  $\sim 10$  km of the river mouth, encompasses both the surface river plume and the underlying saline water column that serves as the source for estuarine inflow. While previous studies have focused primarily on the surface plume dynamics, understanding the full water column in this region is essential for characterising the source conditions of saline inflow.

The "near-field plume" is the near-surface layer of freshwater that has just discharged from the estuary. It is characterised by jet-like plume expansion, often supercritical, experiences rapid mixing, and generates tidally varying frontal features (Horner-Devine et al., 2015). Turbulent kinetic energy dissipation rates are observed to be as high as  $10^{-4}$  to  $10^{-3}$   $\text{m}^2 \text{s}^{-3}$  (MacDonald and Geyer, 2004; MacDonald et al., 2007; McCabe et al., 2008; Kilcher et al., 2012). In the mid-field region, depending on the plume's dynamics (Garvine, 1995), the energetic freshwater jet that dominates the near-field can transform into a coastal current under

the increasing influence of Earth's rotation, which typically deflects the plume in the downcoast direction (Horner-Devine et al., 2015).

The saline bottom water in the near-field region forms the primary source for estuarine inflow, we refer to this salinity as  $s_0$  in the remainder of this chapter. Particle pathways in an idealised model, investigated by Brasseale and MacCready (2021) showed that more than half of particles released in the plume recirculate and make their way back into the estuary with a narrow mouth. The presented particle paths indicate that particles travel away from the mouth in the plume, mix down into the lower layer, and can thereby be transported back into the estuary at depth. The near-field river plume and the estuary are dynamically connected, where estuarine mixing rates are indicative of the salinity of the outflowing plume at the surface (Nash et al., 2009).

Many plume-estuary interactions have been studied on narrow, deep shelves, where dynamics differ from those on shallow, wide shelves like the North Sea. The Rhine River plume is located in this shelf sea, where bottom friction and tides play a major role (e.g., Visser et al., 1994; Simpson, 1997; de Boer et al., 2006; Rijnsburger et al., 2018). While friction is important, the plume is not consistently bottom attached like other plume systems considered to be shallow (Garvine, 1995). Cross-shore tidal straining creates a dynamic coupling between the surface plume waters and bottom saline waters that feed into the estuary (Simpson, 1997), in contrast with deeper systems such as the Columbia River plume. We use the Rhine-Meuse Delta estuary and its associated river plume as a case study to investigate the plume-estuary connection in a shelf sea.

The dominant intratidal pattern in the mid-field and far-field of the Rhine River plume is characterised by alternating patterns of stratification and mixing over a tidal cycle, referred to as Strain-Induced Periodic Stratification (Simpson et al., 1990; Visser et al., 1994; Simpson and Souza, 1995). This pattern results in counter-rotating tidal ellipses in the upper and lower layers under stratified conditions, which become rectilinear for well-mixed spring tide conditions (Souza and Simpson, 1996; de Boer et al., 2006).

Studies on the Rhine River plume are in line with the expected response to downwelling-favourable and upwelling-favourable winds, as described in earlier studies (e.g., Fong and Geyer, 2001). Downwelling winds push the plume towards the coast, which causes the plume to thicken, while upwelling winds detach it from the coast and the plume thins (Keyzer, 2025). These wind conditions also influence the propagation speed of tidal plume fronts in the alongshore direction, which increases during downwelling-favourable winds (Rijnsburger et al., 2018).

Geraeds et al. (2025) used a realistic model to investigate the influence of coastal wind direction on the Rhine-Meuse Delta estuary. They showed that wind direction strongly controls estuarine exchange flow and its associated salt transport. Upwelling-favourable winds increase it and downwelling-favourable winds decrease it, in line with findings of Giddings and MacCready (2017).

Previous studies have linked ocean and plume dynamics to estuarine processes, with a focus on wind-driven upwelling and downwelling (e.g., Hickey

et al., 2002; Giddings and MacCready, 2017). However, bottom salinity has received less attention, especially in shallow shelf seas like the North Sea, where dynamics differ from those near the continental shelf.

Therefore, we pose the research question: what determines the estuarine inflow conditions? Specifically, we investigate how wind and tidal forcing influence flow and salinity near the river mouth, thereby modulating the offshore boundary condition for estuarine salt intrusion. We address this question using a unique set of field observations from the near-field Rhine River plume and the Rhine-Meuse Delta estuary, collected during a severe drought.

In section 4.2 we describe our dataset and methods, in section 4.3.1 we describe the forcing conditions, in section 4.3.2 we give a brief overview of the intratidal dynamics in the near-field region, in section 4.3.3 we explore how winds and tides influence the velocities and salinity, and in 4.3.5 we discuss how these changes in boundary conditions influence estuarine salinity. In section 4.4, we present a discussion and introduce a conceptual framework for estuarine inflow, followed by a summary of the conclusions in section 4.5.

## 4.2 Data and Methods

### 4.2.1 Study site

The Dutch Rhine-Meuse Delta Estuary is a salt wedge estuary (de Nijs et al., 2011), where upstream branches can be partially and well-mixed during drought conditions (Wegman et al., 2025). The Rhine-Meuse Delta (Fig. 4.1) is a heavily engineered delta, with Europe's largest harbour: the Port of Rotterdam. The Rhine River enters the measurement domain through the branches called the Lek and Boven-Merwede. The Meuse enters the domain in the southeast, as indicated in Figure 4.1a. The system's main branch is the Rotterdam Waterway, which discharges into the North Sea, forming the Rhine River plume, visible in the satellite image taken during the field campaign (Fig. 4.1a). The near-field River plume region is influenced by two manmade structures. First, the Maasvlakte 2, an offshore extension of the harbour. Second, a jetty north of the shipping channel.

### 4.2.2 Data collection

Field measurements were taken from 22 June to 19 October 2022, in the Rhine-Meuse Delta estuary and around the river mouth. A total of five mooring stations were deployed in the near-field region, with upward-looking Acoustic Doppler Current Profilers (ADCPs) and Conductivity, Temperature, Depth (CTD) sensors. Four moorings, N1, N2, S1, and S2, were present for the first 6 weeks, between 22 June and 10 August 2022. The mooring in the navigation channel, NAV, was present for an additional 11 weeks.

Furthermore, we used CTD data from six different locations within the es-

tuary, three of which were installed for this survey at NM-A buoy, Eemhaven, and the Port of Rotterdam (NMA, EEM, PoR). Sensors were also installed on a floating platform during the Maasdeltatunnel (MDT) construction. The remaining salinity data were retrieved from permanent measurement stations of Rijkswaterstaat, including Hoek van Holland (HVH) and Brienoordbrug (BRB). Figure 4.1 indicates the measurement locations.

Flow velocities were measured at all near-field mooring locations, with upward-looking Nortek Signature 1000 ADCPs, with a vertical binsize of 30 cm. The sampling frequency was 4 Hz (NAV, S2, N2) or 8 Hz (N1, S1) with burst of 6 minutes every 12 minutes. At NAV, the ADCP frame also contained one CTD sensor. A vertical mooring line was placed 1.2 km northeast of the ADCP, because of shipping restrictions. We call this adjacent mooring line NAV-b. Bottom salinities at the adjacent NAV and NAV-b moorings are strongly correlated ( $R = 0.96$ , Figure C.4a), so for the remainder of the analysis, we focus on the multiple depth measurements of salinity from NAV-b. At two other mooring stations (N2, S1), the ADCP frame also contained one CTD sensor. Unfortunately, the CTD at N2 collected no data for the entire period. For the vertical mooring lines (S2, N1, and NAV-b), we deployed arrays with five, four, and six CTD sensors, respectively. The uppermost CTD sensor was attached to a buoy at 1 m below the sea surface. The remaining sensors were evenly distributed over the mooring line. An overview of the settings at the different stations is given in Table 4.1. The locations of the six stations were chosen such that they formed a ring around the river mouth. Due to restrictions imposed by shipping, all measurement stations had to be near navigation buoys, and not all measurement stations contain a vertical CTD mooring line.

Data on wind speed, wind direction, and atmospheric pressure at HVH were retrieved from the Royal Dutch Meteorological Office (KNMI). The Rhine River discharge data at Lobith (Dutch reference location, see Figure 4.1a) were retrieved from the Rijkswaterstaat database, as well as the water level and astronomical tide at the mouth (HVH).

### 4.2.3 Data processing

#### Salinity data

Data affected by biofouling were manually removed or corrected based on comparison to neighbouring sensors where appropriate. The surface sensor at NAV had an offset from 14 July onwards, which we corrected using flood salinity values of two neighbouring surface sensors and T-S diagrams, see Appendix C.1 for details.

We interpolated and extrapolated data from the near-field CTD strings to obtain a continuous vertical salinity profile. We assumed that near-surface and near-bottom CTD measurements were representative of surface and bottom salinity, to extrapolate over the full water column. The salinity data were interpolated verti-

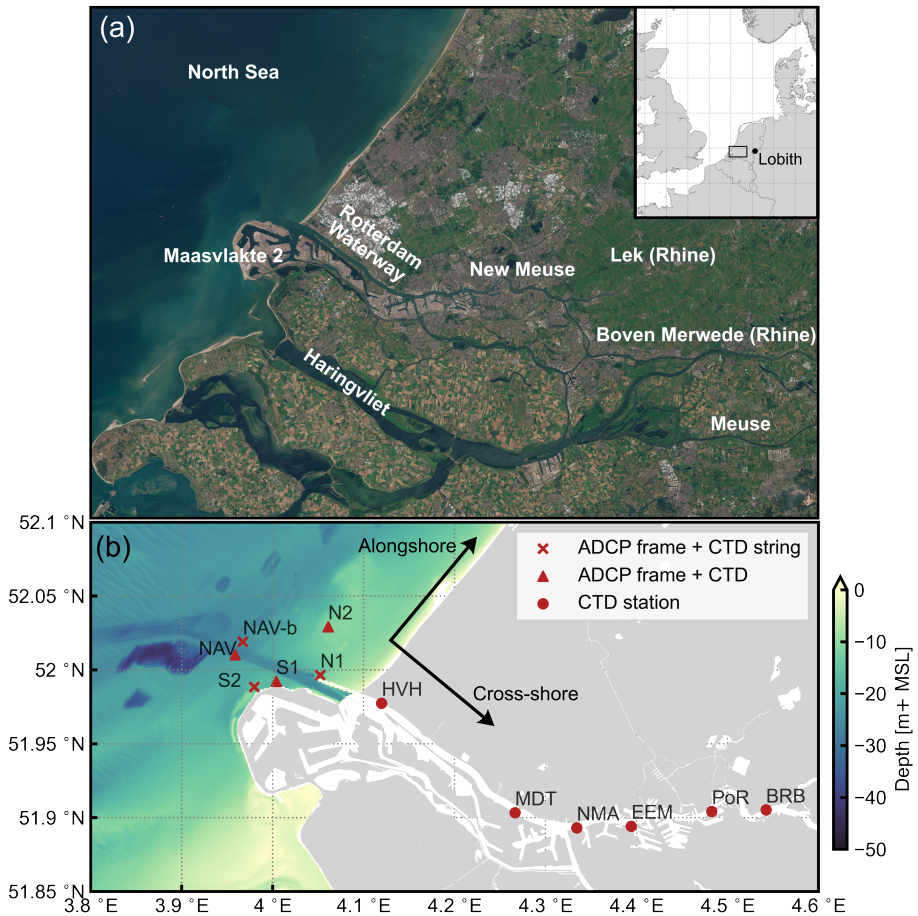


**Figure 4.1:** Map of Rhine-Meuse Delta estuary and corresponding near-field river plume region. (a) Sentinel image from 24 July 2022. (b) Bathymetry map, including the near-field measurement stations, and inland salinity stations at Hoek van Holland (HVH), Maasdelatunnel (MDT), Buoy NM-A (NMA), Eemhaven (EEM), the Port of Rotterdam (PoR), and Brienoordburg (BRB). Arrows indicate the reference frame for wind speed and flow velocities.

cally to the vertical coordinates of the ADCP data and re-indexed to the temporal resolution of the ADCP data (12 minutes).

**Table 4.1:** Overview of measurement stations in the near-field region and along the estuary.

Station name	Location	Set-up	Number of CTDs
NAV	near-field region	ADCP frame + CTD string	6
N1	near-field region	ADCP frame + CTD string	4
N2	near-field region	ADCP frame + 1 CTD	1
S1	near-field region	ADCP frame + 1 CTD	1
S2	near-field region	ADCP frame + CTD string	5
HVH (5 km)	estuary	CTD string + water level	3
MDT (18.2 km)	estuary	CTD string	2
NMA (23 km)	estuary	CTD string	2
EEM (27.2 km)	estuary	CTD string	2
PoR (33.5 km)	estuary	CTD string	2
BRB (40 km)	estuary	CTD string	2

### Velocity data

The raw ADCP data were filtered to remove outliers by applying a minimum broadband correlation threshold of 50 percent and a minimum amplitude threshold of 30 dB. Furthermore, the upper layer (18 percent of the total depth) was removed to eliminate data influenced by side lobe interference of the sea surface. The ADCPs operated in burst mode, collecting 6-minute bursts every 12 minutes. Each burst was averaged to obtain velocity data with a frequency of 12 minutes.

To replace the data near the surface, removed because of side-lobe interference, the velocity profiles were extrapolated with a parabolic function constrained to have zero shear at the surface. Additional NaN values in velocity data were also filled. For temporal gaps of a maximum of 60 minutes, data were filled by linearly interpolating in time, and remaining NaN values were interpolated vertically using an Akima interpolator. Finally, the velocity profiles were interpolated to a  $\sigma$ -coordinate system, which allows proper temporal averaging (Lerczak et al., 2006).

The horizontal velocity components (eastward and northward) were projected on axes rotated 42.5 degrees clockwise to obtain alongshore and cross-shore components. The alongshore direction is defined as positive towards the northeast, and the cross-shore direction is positive onshore. With this coordinate rotation,

flood-directed currents align with the positive alongshore and cross-shore directions, as indicated by the arrows in Figure 4.1b.

To distinguish between different flow mechanisms, we determine two components of velocity  $u(z, t)$  based on Lerczak et al. (2006), tidally and depth-averaged  $u_0$  and tidally averaged and depth-varying  $u_1(z)$ :

$$u_0 = \frac{1}{H_0} \left\langle \int_{-h}^{\eta} u(z, t) dz \right\rangle \quad (4.1)$$

$$u_1(z) = \left\langle \left( \frac{h + \eta(t)}{h} \right) u(z, t) \right\rangle - u_0 \quad (4.2)$$

Here,  $\eta(t)$  is the water level elevation,  $h$  is the local water depth, and  $H_0$  is the low-pass filtered water depth. The angled brackets  $\langle \cdot \rangle$  indicate a low-pass subtidal Godin filter (Godin, 1972). This filter is obtained by subsequently taking the convolution of two running means of 24 hours, and the convolution of this triangular filter with a running mean window of 25 hours.

The magnitude of the depth-averaged tidal velocity was computed as:

$$u_{tidal}(t) = \frac{1}{H_0} \int_{-h}^{\eta} U(z, t) dz. \quad (4.3)$$

where tidal velocity magnitude  $U = \sqrt{u_i^2 + u_j^2}$ , with  $u_i$  and  $u_j$  denoting the eastward and northward velocity components, respectively.

To estimate the importance of tidal mixing and buoyancy on estuarine outflow (Nash et al., 2009), we calculate the estuarine Richardson number  $Ri_E$  according to Fischer (1972):

$$Ri_E = g \frac{\Delta \rho}{\rho} \left( \frac{Q_R}{B u_{tidal}^3} \right) \quad (4.4)$$

Here,  $Q_R$  is the river discharge,  $B$  the channel width,  $u_{tidal}$  the depth-averaged tidal velocity (Eq. 4.3),  $g$  is the gravitational acceleration, and  $\frac{\Delta \rho}{\rho} = 0.025$  is the fractional density difference between fresh river and saline ocean water.

### Wind data

Wind speed data were projected onto axes rotated 42.5 degrees clockwise to obtain alongshore and cross-shore components, aligned with wind-driven downwelling and upwelling of the Rhine River plume. For the wind direction analysis, we identified onshore, upwelling-, and downwelling-favourable wind events based on the relevant wind direction  $\pm 10$  degrees, and a minimum wind speed of  $6 \text{ m s}^{-1}$ , based on 12-hour averaged values.

### 4.3 Results

We begin by examining the near-field region, going from overall behaviour to detailed responses to tidal and wind forcing, in order to link the estuarine inflow conditions to the estuary. Then we examine the NAV shipping-channel data and show how near-field dynamics—particularly lower-layer behaviour—govern the extent of inland salt intrusion.

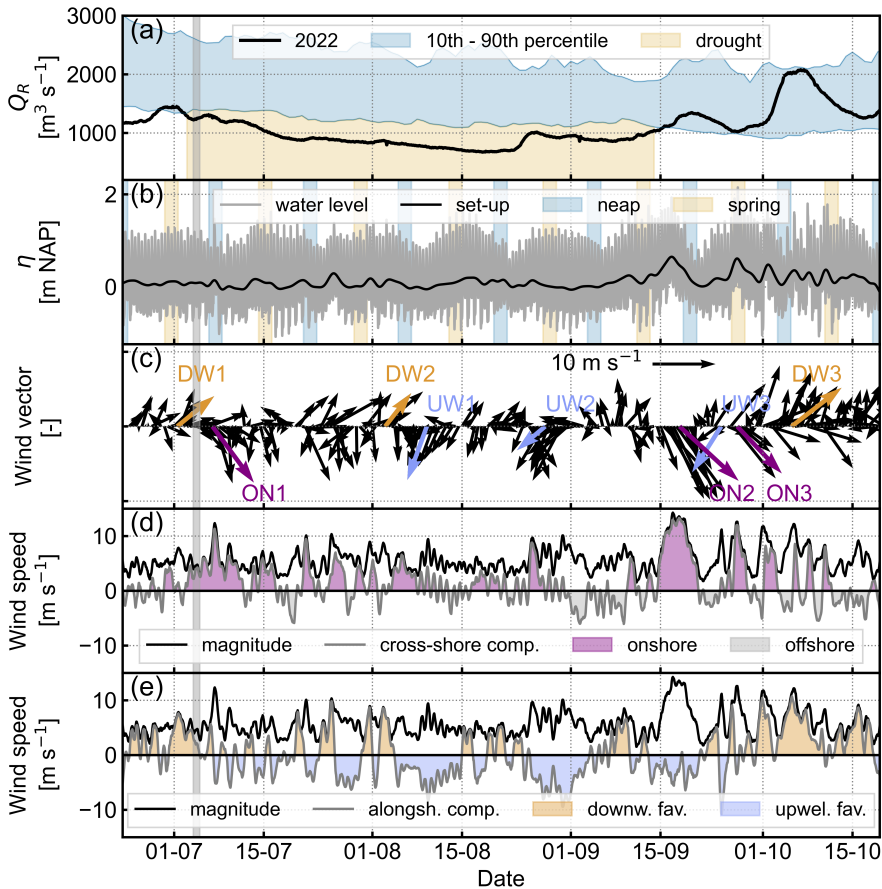


**Figure 4.2:** Forcing during the field campaign, including (a) the Rhine River discharge  $Q_R$ , showing the 10<sup>th</sup>-90<sup>th</sup> percentile range for the climatological period (1992-2021) and period of severe drought, (b) the measured water level  $\eta$  and calculated set-up  $\langle \eta \rangle$  at Hoek van Holland, with the spring-neap cycle highlighted, (c) wind vector at Hoek van Holland, (d) magnitude of the wind speed, with the cross-shore wind component highlighted, (e) magnitude of the wind speed, with the alongshore wind component highlighted. The grey highlight indicates the baseline period (4 July).

### 4.3.1 Forcing conditions

The forcing conditions during the study period are shown in Figure 4.2. During the measurements, the Rhine River discharge at Lobith ( $Q_R$ ) ranged from approximately 670 to 2100 m<sup>3</sup> s<sup>-1</sup> (Fig. 4.2a), with an annual average of 2178 m<sup>3</sup> s<sup>-1</sup> for reference. This range includes a 75-day period of severe drought, when discharge fell below the 10th percentile of the climatological record (Wegman et al., 2025), highlighted in yellow.

Wind speeds, measured 10 metres above the surface  $U_{10}$ , were mostly low to moderate (between 3 and 8 m s<sup>-1</sup>) from June to August. In September and October, stronger winds exceeding 10 m s<sup>-1</sup> occurred more frequently (Fig. 4.2c), leading to coastal set-up and set-down (Fig. 4.2b). Onshore (northwesterly) winds can drive an immediate coastal set-up, and a subsequent set-down when the wind relaxes, as can be seen in Figure 4.2b-d. The alongshore wind, upwelling-favourable (northeasterly) or downwelling-favourable (southwesterly) conditions have been indicated in Figure 4.2e.

We selected three downwelling-favourable wind (orange in Figure 4.2c), three upwelling-favourable wind (blue in Figure 4.2c), and three onshore wind events (purple in Figure 4.2c) for closer examination. We chose these instances because they were closest to the respective wind direction and highest wind speeds. Despite the shallowness of the system, earlier work in the Rhine River plume showed classic Ekman dynamics (Rijnsburger et al., 2018, 2021a).

### 4.3.2 Intratidal response of the near-field region

The near-field mooring measurements are interpreted within the existing conceptual picture of near- and mid-field plume dynamics in this region from prior studies. Previous studies (e.g., de Boer et al., 2006, 2008; Rijnsburger et al., 2021a) showed that flood tide around high water (HW) drives northeastward (down-coast) coastal flow, while ebb tide around low water (LW) generates southwestward (upcoast) flow, these tidal currents peak around high and low water. The new tidal plume front is typically ejected several hours after HW and is subsequently arrested near the mouth by the southward-flowing ebb tidal currents. The tidal plume front is ejected offshore and begins alongshore propagation, in a downcoast direction, after low water slack (LWS). In the mid-field, tidal straining induces counter-rotating tidal ellipses with anti-cyclonic rotation at the surface and cyclonic near the bed. A recent study on the influence of the offshore harbour extension shows that the recirculating flows in the near-field are dependent on the tidal and wind conditions, where the recirculating currents are strongest for neap tides, and vanish for storm conditions (Jakšić, 2021).

To characterise the dynamics in the near-field region, we selected a baseline period with moderate winds between spring and neap tides (4 July 2022). Tidal variations in salinity and velocity are shown in Figures 4.3 and 4.4. Near-surface and near-bottom salinity and velocity vectors during one tidal cycle are presented

in Figure 4.3b-e, with key tidal phases: HW, high water slack (HWS), two low waters (LW1 and LW2), and LWS, marked in Figure 4.3a. HWS and LWS are defined as the times when the depth-averaged velocity at NAV is zero.

The station closest to the mid-field (N2) shows flow patterns indicative of counter-rotating tidal ellipses (Figs. 4.3d, e), in line with literature. In the bottom layer, the velocity vectors move anti-clockwise (cyclonically) within the tidal cycle, while the surface layer has a clockwise rotation (anti-cyclonically). This is also seen in the vertical structure of the alongshore and cross-shore velocities (Figs. 4.4h, i). At HW and LW, there are instances when the entire water column is either flooding or ebbing. However, in the cross-shore velocities at HWS we observe onshore-directed velocities at the surface and offshore-directed velocities at depth, and the other way around on LWS, in line with Souza and Simpson (1996).

Station NAV, located offshore in the navigation channel and a key location to link the near-field to the estuary, captures the passage of the river plume. The cross-shore velocities have a strong landward current at depth, near HW, when the tide is flooding. Surface currents are offshore-directed most of the tidal cycle, except for flood velocities just before HW (Fig. 4.4c). The dominant tidal component is alongshore (Fig. 4.4b), where the velocities are in phase with the water level. The tidal plume front passes between LW1 and LWS (Fig. 4.4a), visible by the pulse of fresher surface water. This is preceded by a thicker layer of slightly saltier water around HWS, likely a remnant from the previous tidal cycle.

Stations N1, S1, and S2 show more rectilinear flow than stations NAV and N2, due to local bathymetric constraints (Figs. 4.3d, e). S1 and S2, influenced by Maasvlakte 2, are out of phase with the other stations, while N1 is likely influenced by the jetty immediately to its south. S2 shows stronger, ebb-dominant flows (Fig. 4.4e) and a more mixed, fresher water column compared to NAV (Fig. 4.4d). This rectilinear flow pattern is also evident from the alongshore and cross-shore velocity components; they are both relatively uniform over depth (Figs. 4.4e, f).

Surface salinity varies more than bottom salinity (Figs. 4.3b, c), because of the presence of the river plume in the top 5 – 10 m of the water column (Figs. 4.4a, d). At HWS, just before the plume's arrival, surface salinity is similar across N1, S2, and NAV. As the front passes N1 and NAV, surface salinity drops, which is seen later at S2 (just before LW2). Bottom salinity decreases slightly at N1 and S2, but not at NAV, likely due to differences in water depth. At shallower stations (N1 ~15m, S2 ~15m), the bottom sensor is closer to the plume than at the deeper station (NAV ~26m) (Figs. 4.4a, d).

The bottom velocity vectors indicate that saline waters entering the estuary predominantly originate from the upcoast direction (Fig. 4.3e). Bottom velocities are directed landward at NAV, S1, and S2 during LWS, and to a lesser extent during HW at S1 and S2. Between HW and LWS, the tidal currents at N2 and NAV are from upcoast (southwesterly) direction (Figs. 4.4b and h).

This pattern is further supported by the six-week time series (22 June–10 August), when all stations were operational. Flow from the upcoast quadrant is de-

defined as the alongshore component within  $\pm 45^\circ$ . Estuarine inflow is identified when velocities at both S1 and S2 are directed onshore. During these inflow periods, alongshore currents at NAV and N2 were oriented in the quadrant from upcoast direction 75% and 68% of the time, respectively. The deviation from 100% reflects the phase between LWS and HW, when currents at NAV and N2 are initially onshore before veering downcoast. By contrast, during alongshore ebb currents (between HWS and LWS) originating from the downcoast direction, estuarine inflow does not occur, and bottom waters bypass the estuary.

In summary, the patterns in intratidal flow and salinity dynamics in the near-field region highlight the spatial variability driven by the tides, plume behaviour, and the influence of engineered structures. However, an estuarine inflow pattern can be distinguished, which is explained by the interaction between the tidal variability and the influence of man-made structures, showing that saline water enters the estuary primarily from the upcoast direction. The stations near man-made structures (S2 and S1) exhibit flow patterns directed toward the estuary mouth on flood tide. In the shipping channel (NAV), alongshore tidal flow patterns are evident, and the cross-shore currents show the outflowing plume as negative velocities away from the estuary mouth. At station N2, counter-rotating tidal ellipses characteristic of mid-field dynamics are observed. This indicates that cross-shore tidal straining is also important in this part of the system, close to the mouth.

### 4.3.3 Near-field bottom salinity under the influence of tides and winds

#### Observations of near-field salinity

Here, we evaluate the near-field bottom salinity  $s_0$ , which represents the source of saline water to the estuary. Figure 4.5 presents time series of surface, subsurface, and bottom salinity at NAV together with forcing conditions. The near-bed salinity follows similar subtidal variations at all our near-field stations (Fig 4.5d). Strong correlations between bottom salinity at NAV and the other sensors support this spatial coherence:  $R = 0.93$  for S1 and  $R = 0.94$  for S2 (Fig. C.4). The correlation between bottom salinity at NAV and N1 is relatively low ( $R = 0.48$ ), probably due to the large difference in water depth and the location of N1, which is just around the jetty, as was discussed in section 4.3.2. The strong correlation of lower-layer salinity at multiple moorings within 6 km of the mouth indicates that NAV salinity is representative of the inflowing water mass ( $s_0$ ). Therefore, we focus on NAV for the remainder of the analysis, which has the longest time record of salinity.

Within our measurement period, we observed subtidal variations of 2.3 PSU at NAV (Fig. 4.5d). The bottom salinity tends to follow the spring-neap tidal cycle, generally decreasing after spring tides and increasing after neap tides (Figs. 4.5a and d). This results from enhanced plume mixing during spring tides, which drives more freshwater into the bottom layer and thereby reduces lower-layer

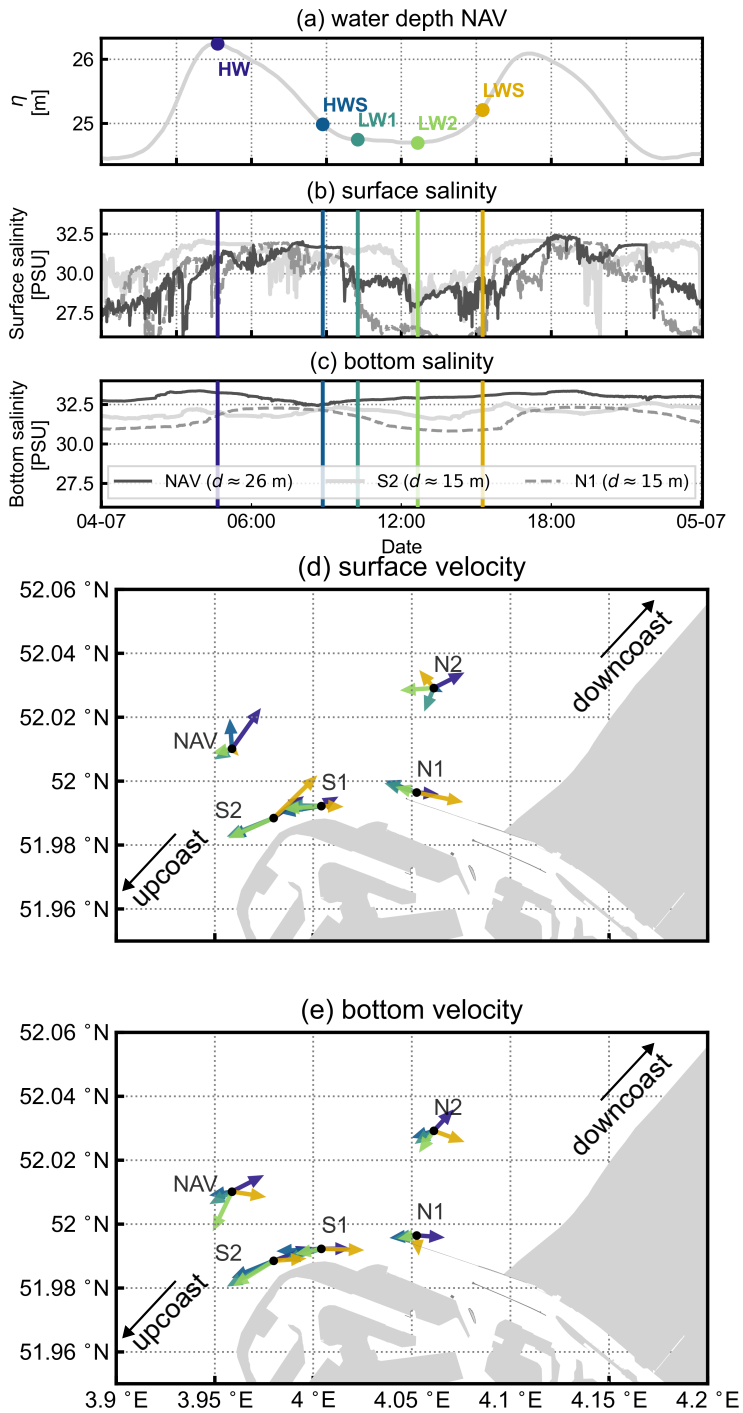


**Figure 4.3:** Water level, salinity, and velocity on 4th July 2022 (a) water level at NAV, (b) surface salinity, (c) bottom salinity, (d) surface velocity vectors, and (e) bottom velocity vectors. Different periods in the tidal cycle are indicated with colours as follows: HW (purple), HWS (blue), LW1 (dark green), LW2 (light green), and LWS (orange).

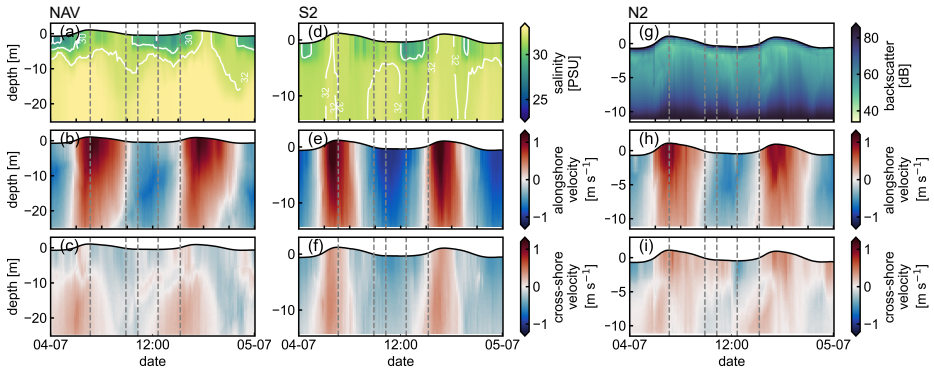


**Figure 4.4:** Salinity, alongshore, and cross-shore velocity, and backscatter between 4th and 5th July 2022 (a-c) at NAV, (d-f) at S2, (g-i) at N2. The depth is with respect to the mean water level.

4

salinity. Nevertheless, the spring–neap tidal cycle alone cannot account for all observed salinity variations. We observe a bottom salinity increase accompanying 6 out of 8 of the sampled neap tide periods and a decrease for 6 out of 8 of the sampled spring tide periods (Fig. 4.5d). On both occasions when the neap tide did not increase bottom salinity (7 July and 1 October, marked with red dashed lines in Fig. 4.5), that period also corresponded to an elevated wind event. We hypothesise that in these situations, the wind mixing may have been sufficient to counteract the salinity increase observed on the other neap tides. Similarly, on 22 June there is a relatively low bottom salinity at neap tides, which was preceded by a wind event on 18 June. Thus, while tides explain a large part of the observed variability, wind events also play an important role. We therefore first examine the relation with tides in more detail before turning to the influence of wind.

### Relation between bottom salinity and tides

The spectra of depth-averaged velocity and bottom salinity (Fig. 4.6) both show dominant M2 and M4 peaks, with increasing energy toward lower frequencies, and a peak near the spring–neap band. Velocity peaks at  $\sim 14.8$  days, while salinity peaks at a slightly higher frequency ( $\sim 14$  days). These spectra confirm a tidal influence on salinity, though they do not distinguish whether this is caused by advection or mixing by tidal currents.

To understand how changes in tidal forcing relate to salinity variation, we determined the time lag between low-passed tidal velocity (Fig. 4.5a) and low-passed bottom salinity (Fig. 4.5d). We found that a maximum Pearson correlation  $R$  occurs at a time lag of 2.5 days, whereas the strongest correlation with surface salinity is observed without any time lag (Fig. 4.7c). At zero lag, the correlation with surface salinity is positive, indicating that enhanced tidal mixing leads to an immediate increase in surface salinity. In contrast, the lower layer salinity  $s_0$  has a negative correlation with tidal velocities, meaning that increased tidal mixing

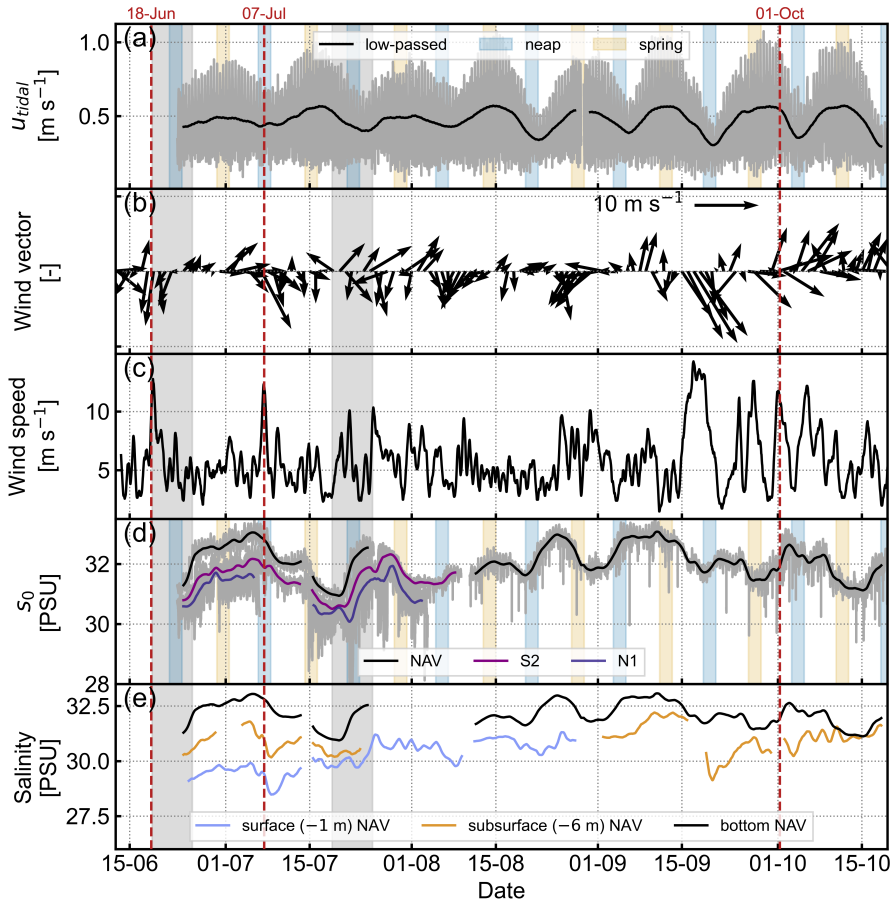


**Figure 4.5:** Forcing and near-field salinity. (a) tidal velocity at Hoek van Holland, with spring and neap tides highlighted, black line is the low-passed signal of the tidal velocities (b,c) wind vectors and speed at Hoek van Holland, (d) bottom salinity  $s_0$  at NAV, S2, and N1 (e) tidal mean salinity of the surface ( $-1$  m), subsurface ( $-6$  m), and bottom sensor at NAV. The red dashed lines indicate wind events just before neap tides, on 18 June, 7 July, and 1 October. The grey highlights indicate the periods shown in Figure 4.9 (two contrasting neap tides).

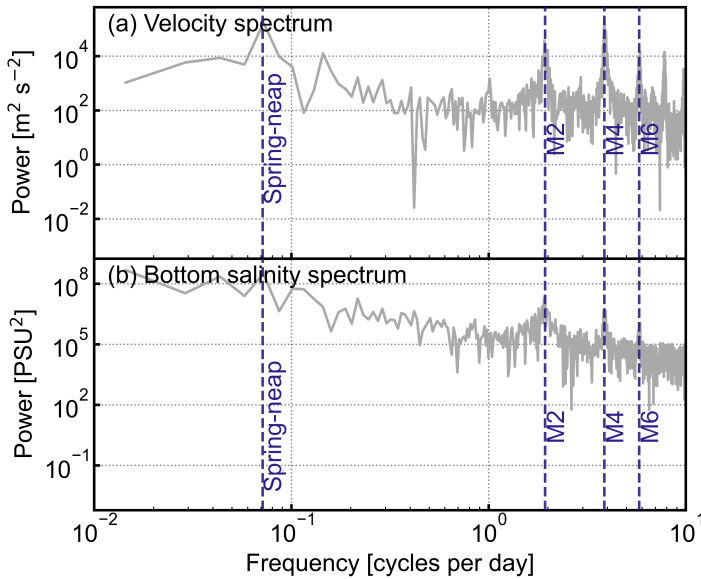


**Figure 4.6:** Power spectra of (a) depth-averaged velocity, and (b) bottom salinity at NAV for the period where continuous near-field bottom salinity measurements are available (between 10 August and 19 October).

leads to a delayed decrease in bottom salinity.

These results suggest that local mixing in the near-field region, which occurs every tidal cycle, is not the primary driver of bottom salinity variations. Instead, the observations suggest that the relevant mixing occurs over several tidal cycles, and probably over a larger spatial area, indicating that it takes several tidal cycles for plume waters to mix effectively down to the bottom layer, and to be transported back to the river mouth.

The relative influence of freshwater discharge and tidal mixing on the salinity of a river plume was investigated by Nash et al. (2009) for the Columbia River plume based on the estuarine Richardson number  $Ri_E$  (Eq. 4.4). In Figure 4.7b and c we compare the bottom and surface salinity with  $Ri_E$ . The surface salinity correlates with  $Ri_E$  ( $R = -0.50$ , Fig. 4.7a), which is expected given that the surface plume originates from the estuarine outflow (Nash et al., 2009). The bottom salinity, however, does not correlate with  $Ri_E$  (Fig. 4.7b).

Surface salinity is primarily governed by estuarine processes, such as river discharge and estuarine mixing, as reflected in its strong correlation with  $Ri_E$ . In contrast, bottom salinity shows no direct relationship with these estuarine drivers. Instead, bottom salinity varies with plume-induced mixing into the bottom layer, but with a temporal lag. This suggests that the surface memory of river discharge variability is lost over the spatial and temporal scales required for vertical mixing

to reach the bottom.

We hypothesise that estuarine inflow salinity is set by mixing processes on the shelf, in the same way that estuarine outflow salinity (plume salinity) is governed by mixing within the estuary. This could include mixing from tidal forcing (Simpson, 1997; de Boer et al., 2006), wind forcing (Rijnsburger et al., 2018; Flores et al., 2017), or internal wave breaking (Rijnsburger et al., 2021b). Here, we focus on mixing due to tidal and wind forcing. This hypothesis is examined further in the Discussion section.

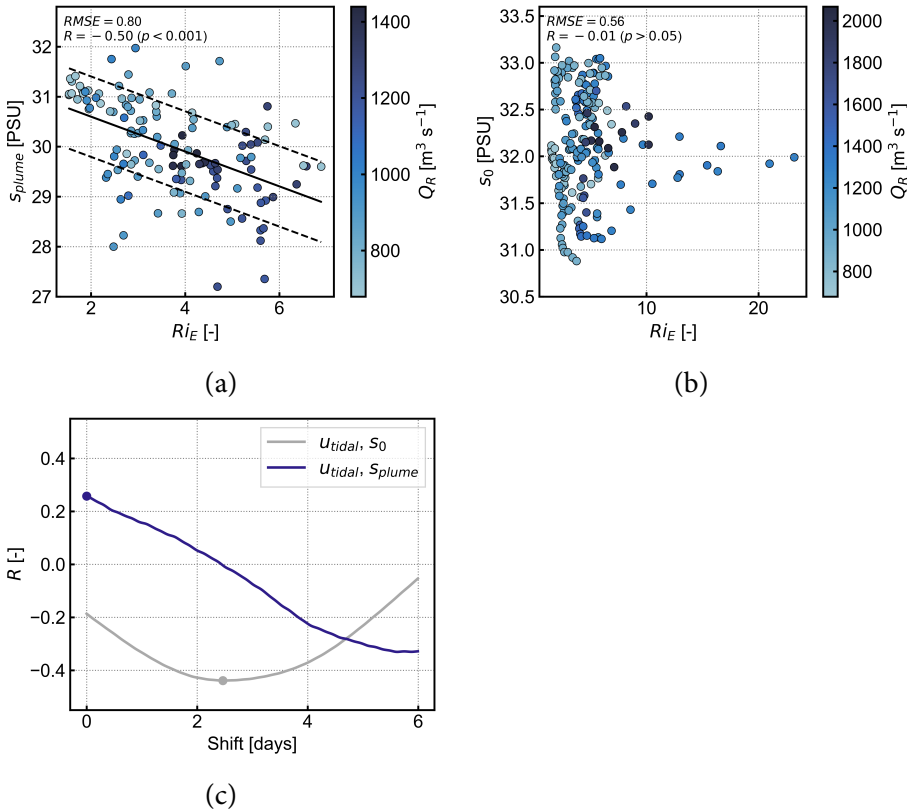


**Figure 4.7:** (a) estuarine Richardson number  $Ri_E$  vs surface salinity  $s_{plume}$ , (b) estuarine Richardson number  $Ri_E$  vs  $s_0$ , (c) Best correlations for time shifts for tidal velocity ( $u_{tidal}$ ) and surface ( $s_{plume}$ ) and bottom ( $s_0$ ) salinity at NAV. The solid black line indicates the least-squares linear fit and the dashed lines indicate this fit  $\pm RMSE$ .

To evaluate fortnightly variations in salinity and mixing, we compare tidally averaged bottom salinity (Fig. 4.5d) with tidal velocity (Fig. 4.5a, Eq. 4.3), using  $u_{tidal}^3$  as a proxy for tidal stirring (Simpson and Bowers, 1981). Figure 4.8 shows their relation with a 2.5-day lag. The correlation is particularly clear during drought conditions ( $Q_R < 1000$  m<sup>3</sup> s<sup>-1</sup>;  $R = -0.69$ ), indicated by the coloured subset, but weaker when including the full record ( $R = -0.46$ ), suggesting that

high tidal energy lowers near-field bottom salinity.

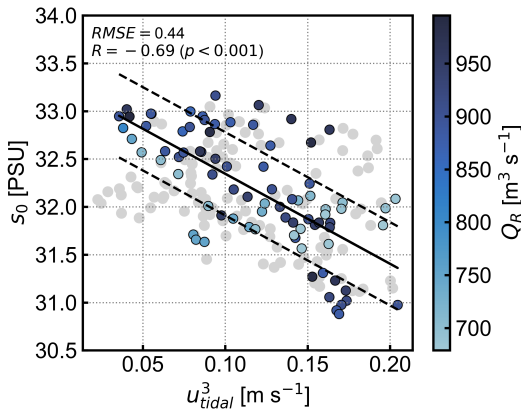


**Figure 4.8:**  $u_{tidal}^3 + 2.5$  days vs bottom salinity  $s_0$  at NAV. The datapoints represent tidal averages. The grey dots are a subset for high discharge ( $Q_R > 1000 \text{ m}^3 \text{ s}^{-1}$ ), the coloured dots for low discharge. The solid black line indicates the least-squares linear fit to the low discharge data and the dashed lines indicate this fit  $\pm RMSE$ .

### Relation between bottom salinity and winds

Wind forcing influences stratification in the Rhine River plume through advection, straining, and vertical mixing (e.g., Rijnsburger et al., 2018; Keyzer, 2025). The clearest impact on bottom salinity arises from wind-induced mixing following high wind speed events ( $U_{10} > 10 \text{ m s}^{-1}$ ), as illustrated by the highlighted periods in Figure 4.5, which we examine in more detail here.

Those selected events with wind speeds exceeding  $10 \text{ m s}^{-1}$  (red dashed lines in Fig. 4.5) were followed by decreasing bottom salinities, which might be attributed to wind mixing. In these examples, the bottom salinity decreases around neap tides, which is opposite to the response to neap tides during low winds. Those two exceptions occur after the wind speed exceeds  $10 \text{ m s}^{-1}$  on 7 July and 1 October. After 7 July, there is a constant decrease in bottom salinity until close to the next neap tide. After 1 October, a decrease starts on 3 October, 2 days after the wind event. At the beginning of our measurements, there was also a neap tide with relatively low bottom salinities, which occurred after wind speeds exceeding  $10 \text{ m s}^{-1}$  on 18 June.

On most neap tides, stratification strengthens and the lower layer gets saltier (e.g., Fig. 4.9f). To demonstrate the influence of wind forcing on  $s_0$ , we compare two neap tides with contrasting bottom salinities and stratification: 23 June and 22 July (Fig. 4.9). Tidal conditions were similar in both cases ( $u_{tidal} = 0.44 \text{ m s}^{-1}$ ), but antecedent wind forcing differed. In June, winds exceeding  $10 \text{ m s}^{-1}$  occurred four days before the observation, whereas in July no strong winds were recorded

during the four days preceding the tide (Figs. 4.9b, e). On 23 June (first grey highlighted period in Figure 4.5), the lower bottom salinity was relatively low (31.2 PSU) and the water column was well mixed. In contrast, on 22 July (the second grey highlighted period in Figure 4.5), the bottom layer salinity was higher (32.2 PSU) and more strongly stratified.

Although wind-driven mixing events can be identified, no statistically significant correlation was found between wind speed and bottom salinity across the range of lagged correlations tested. Nevertheless, the examples illustrate that, even under similar tidal conditions, bottom salinity can vary substantially depending on antecedent wind forcing. The observed time lag between wind events and the salinity response suggests that, as with tidal mixing, wind-induced mixing spans a temporal scale exceeding several tidal cycles, with its effects only later becoming evident near the estuarine boundary.

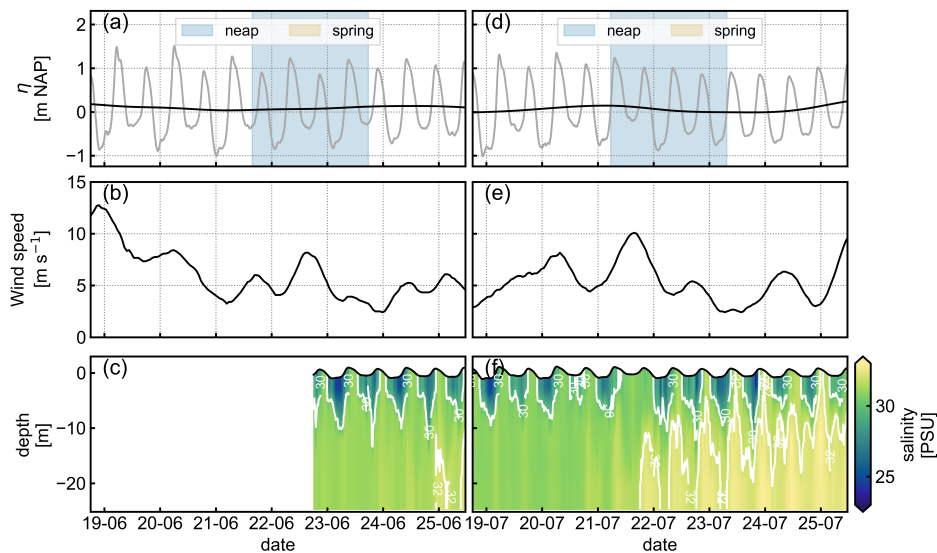


**Figure 4.9:** Two neap tides following contrasting wind conditions. The left panel shows the neap tide after a strong wind event (18–25 June), and the right panel shows a typical neap tide (18–25 July). Panels show (a,d) water level at HVH, (b,e) wind speed at HVH, and (c,f) vertical salinity distribution at NAV.

#### 4.3.4 Coastal set-up and subtidal velocities under the influence of wind

Wind can influence the river plume and salt intrusion into the estuary via coastal set-up and plume advection. Here, we show the influence of local wind on the subtidal water levels and alongshore and cross-shore plume advection, and salinity.

### Effect of wind on coastal set-up

The coastal set-up in the North Sea is mainly driven by large-scale meteorological forcing, especially wind stress. Atmospheric pressure also contributes through the inverse barometric effect, where high pressure lowers sea level and low pressure raises it (Weisse et al., 2012). Our observations confirm this mechanism, as indicated by a negative correlation between coastal set-up and atmospheric pressure ( $R = -0.56, p < 0.001$ ).

To evaluate the local wind contribution to coastal set-up at Hoek van Holland, the set-up signal is pressure-corrected for the effect of atmospheric pressure at Hoek van Holland. The pressure-corrected set-up is defined as:

$$\langle \eta \rangle_{pc} = \langle \eta \rangle - \Delta \langle \eta \rangle_{atm},$$

where  $\langle \eta \rangle$  is the low-pass filtered observed water level, and  $\Delta \langle \eta \rangle_{atm} = -\frac{(P-P_0)}{\rho_s g}$  accounts for the pressure-induced sea level change, where  $P$  is the observed atmospheric pressure at Hoek van Holland,  $P_0$  is the mean atmospheric pressure (reference), and  $\rho_s = 1025 \text{ kg m}^{-3}$  is the density of seawater.

The correlations between the set-up and local cross- and alongshore wind (Fig. 4.10) show that the cross-shore wind is more effective ( $R = 0.64$ ) in driving set-up than the alongshore wind ( $R = 0.14$ ). This aligns with expectations, as onshore winds (positive cross-shore direction) drive water accumulation against the coastline, thereby elevating local sea level and enhancing the coastal set-up. In contrast, alongshore winds may contribute to coastal sea level changes via Ekman transport. However, our observations (Fig. 4.10b) indicate that this mechanism does not significantly affect the water level at the mouth of the estuary.

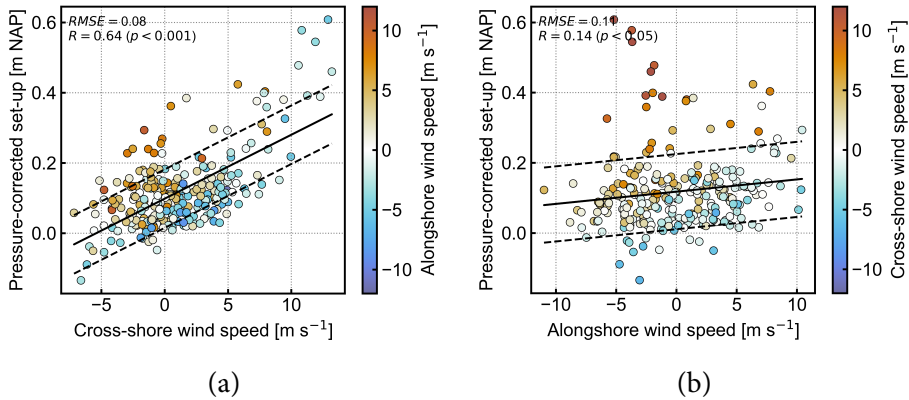


**Figure 4.10:** (a) Cross-shore wind speed vs pressure-corrected set-up, (b) Alongshore wind speed vs pressure-corrected set-up. The solid black lines indicate the least-squares linear fit and the dashed lines indicate this fit  $\pm RMSE$ .

**Table 4.2:** Selected wind conditions.

Date	Event	Wind direction [deg N]	Wind speed [m s <sup>-1</sup> ]	$\tau_{as}$ [Pa]	$\tau_{cs}$ [Pa]	$u_{plume,cs}$ [m s <sup>-1</sup> ]
2022-07-01	DW 1	230.0	7.8	0.10	0.00	0.08
2022-08-03	DW 2	217.5	6.8	0.08	0.00	0.06
2022-10-05	DW 3	232.5	11.9	0.18	0.01	0.12
2022-08-09	UW 1	51.7	9.3	-0.13	0.03	-0.11
2022-08-28	UW 2	51.7	6.2	-0.06	0.00	-0.05
2022-09-24	UW 3	36.7	8.9	-0.14	0.01	-0.12
2022-07-07	ON 1	320.8	11.6	-0.02	0.22	
2022-09-18	ON 2	312.5	13.0	0.00	0.29	
2022-09-27	ON 3	315.0	10.7	0.00	0.20	

### Effect of wind on subtidal velocities

Wind effects on subtidal velocities are examined for the events listed in Table 4.2 and highlighted in Figure 4.2c. Figure 4.11 shows tidally filtered velocity profiles at NAV at the end of the respective 12-hour wind forcing periods. Alongshore and cross-shore velocity profiles, their deviations from the temporal mean, and the cross-shore subtidal shear flow (defined as the deviation from the subtidal depth-averaged velocity) are analysed. These analyses provide insight into near-field-estuary exchange and the role of velocity structure at the boundary in modulating estuarine inflow.

Wind forcing is expected to increase velocities aligned with the wind direction. During upwelling and downwelling conditions, we would also expect a contribution of Ekman transport, 90 degrees to the right of the wind direction.

The downwelling-favourable wind event which occurred on 1 July (DW1, 225.5 degrees North), is characterised by the strongest alongshore flow velocity aligned with the wind direction (Fig. 4.11a), with a positive anomaly in the alongshore flow direction throughout the upper 4/5 of the water column (Fig. 4.11c). The subtidal alongshore velocity in the upper layer reaches about one-quarter of the typical tidal velocity ( $0.30 \text{ m s}^{-1}$  compared to  $1.2 \text{ m s}^{-1}$ ). This structure is representative of all other downwelling wind events (Fig. C.5). The cross-shore flow anomaly (Fig. 4.11d) is what we would expect for downwelling winds; onshore positive for Ekman response.

The event with upwelling-favourable winds occurred on 9 August (UW1, 42.5 degrees North) and had the oppositely directed subtidal alongshore velocities compared to the downwelling winds; the alongshore velocity and velocity anomaly were both negative over the entire water column (Figs. 4.11a, c) for the full water column. The cross-shore velocity in the upper layer is slightly smaller than the temporal mean, and the anomaly is negative. These patterns are consistent for the other upwelling events as well (Fig. C.5).

Overall, the cross-shore velocity anomalies during upwelling and downwelling events are consistent with Ekman dynamics in the upper layer: surface onshore-directed flow during downwelling-favourable winds and offshore-directed flow during upwelling-favourable winds. These observations are consistent with previous studies, which have also reported advection of the Rhine River plume by Ekman transport (Rijnsburger et al., 2018; Keyzer, 2025). While the plume responds strongly to Ekman dynamics at larger scales, the local water surface response near the river mouth is less sensitive.

We estimate depth-averaged cross-shore velocity within the plume  $u_{plume,cs}$ , assuming that the Ekman balance dominates the alongshore momentum equation following Fong et al. (1997) and Fong and Geyer (2001):

$$u_{plume,cs} = \frac{\tau_w}{\rho_s f h} \quad (4.5)$$

with wind shear stress  $\tau_w = C_d \rho_a U_{10} |U_{10}|$ , the density of air  $\rho_a = 1.2 \text{ kg m}^{-3}$ , and the dimensionless drag coefficient  $C_d = 0.0015$  (Wilson, 1960), seawater density  $\rho_s = 1025 \text{ kg m}^{-3}$ , Coriolis parameter  $f$ , and freshwater layer depth  $h$ . The depth  $h$  is estimated as the location where the alongshore velocity  $u_1 = 0$ , as shown in Figure 4.11e. The resulting magnitude of the estimated Ekman velocities ( $|u_{plume,cs}| \approx 0.05 - 0.12 \text{ m s}^{-1}$ , see final column of Table 4.2) are of the same order magnitude as the observed cross-shore velocity anomaly in the surface layer ( $0.02-0.11 \text{ m s}^{-1}$ , see Figure 4.11d and C.5). However, the difference between the estimated  $u_{plume,cs}$  for the different events is not consistent with the cross-shore velocity response. This is because the wind direction is never purely downwelling or purely upwelling; the cross-shore wind speed component varies between  $-1.5$  and  $+3.5 \text{ m s}^{-1}$  for the selected events.

Despite the clear response of the near-field velocity structure due to upwelling- and downwelling-favourable winds, we did not observe any signal of upwelled masses of saline water in the near-field. There is no statistically significant correlation between alongshore wind speed and bottom salinity, nor between these values only for the selected wind direction ( $\pm 10$  degrees of the alongshore direction). In contrast, near-field bottom salinity variability is correlated with tidal velocity, with a correlation coefficient of  $-0.69$  (section 4.3.3), indicating that tidal forcing dominates over wind forcing in controlling bottom salinity.

In contrast to the upwelling and downwelling cases, the onshore wind event (ON1, 312.5 degrees North) shows little response in the alongshore velocity (Figs. 4.11a, c). Onshore winds reduce the offshore-directed velocities in the upper layer, and they also reduce the onshore-directed velocities at depth. The response in the upper layer is consistent with the wind direction, against the vertical flow pattern of outflowing river water.

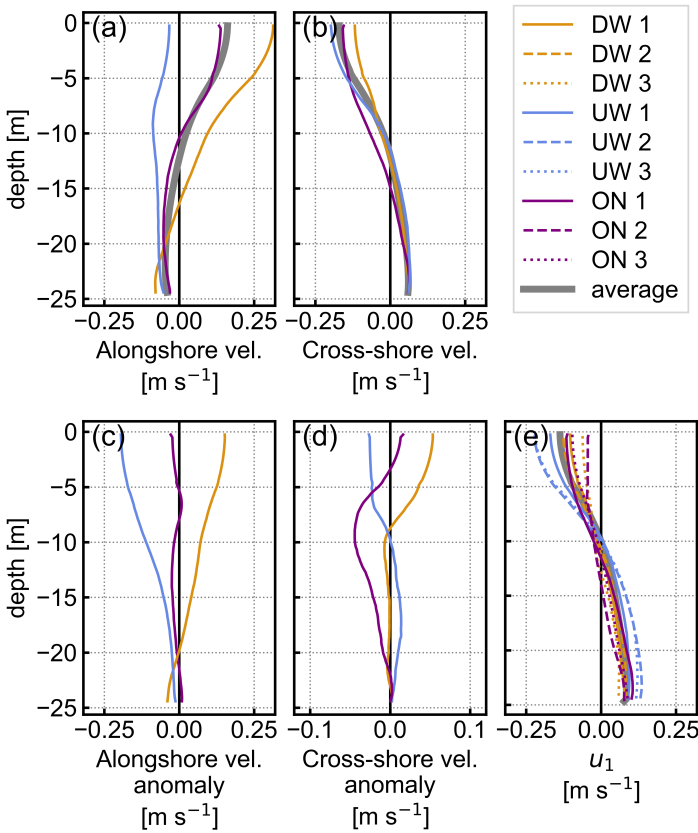


**Figure 4.11:** Velocity profiles at NAV for selected periods with upwelling-, downwelling-favourable, and onshore winds. Including tidally filtered (a) alongshore velocities and (b) cross-shore velocities, (c-d) the corresponding anomalies (difference between the temporal mean). e) Cross-shore subtidal shear flow  $u_1$  at NAV for the different wind conditions. The thick grey lines indicate the time average of alongshore velocity, cross-shore velocity, and  $u_1$ .

We evaluate the subtidal shear flow  $u_1$  because it provides insight into the exchange between the estuary and the plume (Fig. 4.11e). It is characterised by outflowing river plume water (negative) and inflowing saline water (positive), as can be seen by the intratidal flow patterns shown in Figure 4.4a and c. We evaluate the subtidal shear flow by subtracting the tidally-filtered depth-average  $u_0$  (Eq. 4.1) from the tidally-filtered depth-varying velocity, resulting in  $u_1$  (Eq. 4.2), as described in section 4.2. The flow profiles for all selected wind conditions are shown in Figure 4.11e. The profile of  $u_1$  shows an increase for upwelling and a decrease for downwelling velocities in the upper layer. Onshore winds decrease  $u_1$  at the surface and at depth. This could inhibit the exchange flow in the near-field region.

### 4.3.5 Relation between near-field salinity and estuarine salinity

To assess how river mouth variability influences estuarine salinity, we use a normalised metric that highlights anomalies relative to mean conditions. This reveals a propagating salinity signal throughout the estuary (Fig. 4.12).

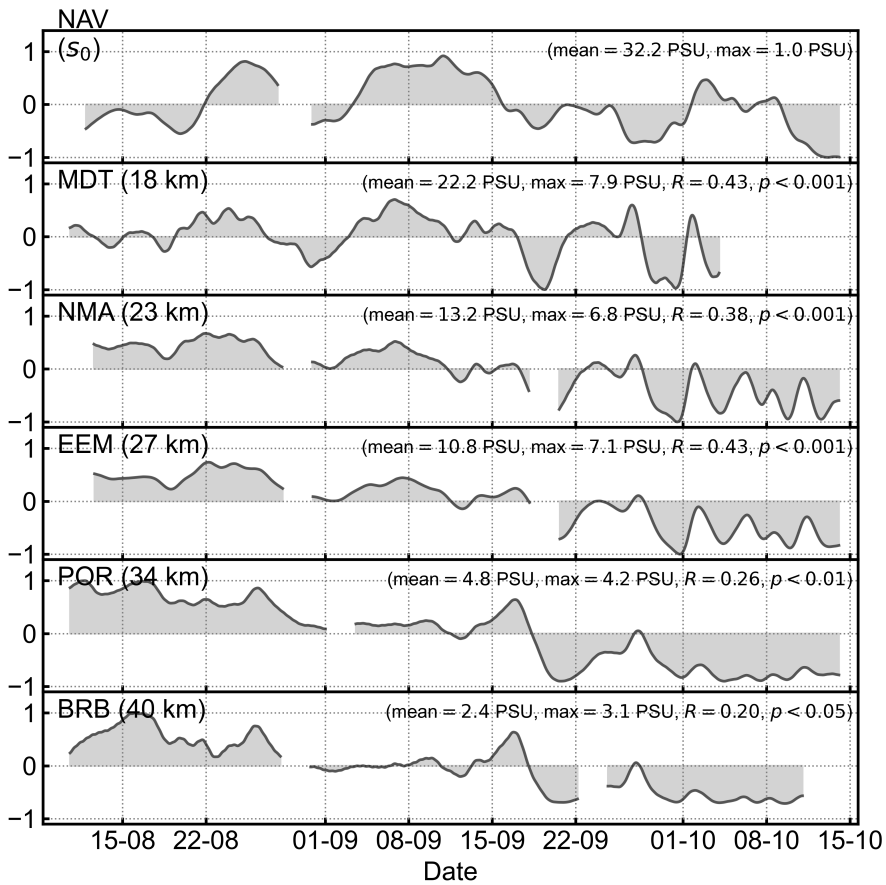
Based on Figure 4.12, we observe positive and negative salinity anomalies lasting 1-2 weeks that are coherent between NAV, MDT, NMA, and EEM stations. The two upstream stations, POR and BRB, show patterns in their anomalies that are similar to each other but differ from the downstream stations. Correlations with near-field salinity  $s_0$  are strongest at the stations closest to the mouth (MDT, NMA, EEM;  $R = 0.38\text{--}0.43$ ,  $p < 0.001$ , zero lag) and weakest at the farthest stations (POR at 33.5 km and BRB at 40 km;  $R < 0.3$ ,  $0.001 < p < 0.05$ ).

We also examine the correlation between salinity and the Rhine River discharge  $Q_R$ , to compare this to the influence of  $s_0$ . While the correlation with  $s_0$  increases downstream, the relative influence of  $Q_R$  decreases. The weakest correlation is observed with  $s_{MDT}$  ( $R = -0.23$ ,  $p < 0.01$ ; Fig. C.8). Salinity at the most upstream stations, POR and BRB (33.5 and 40 km inland, respectively), has a weak correlation with  $s_0$ , but a strong dependence on  $Q_R$  ( $R \approx -0.8$ ; Fig. C.8). This pattern may be attributed to the local water depth and distance from the mouth. Shallower stations experience higher discharge velocities ( $u_R = Q_R/A$ ), potentially strengthening the correlation. Farther upstream, there has been less mixing with saline water, so there is a fresher contribution from riverine water.

We further focus on the station closest to the mouth (MDT) to assess its role in salt intrusion and its potential co-dependence on tidal forcing. No significant correlation is found between MDT salinity and the unlagged tidal velocity. However, for the optimum time lag of 3.0 days, there is a correlation of  $R = -0.38$  (Fig. 4.13). In comparison, the highest correlation between  $s_0$  and  $s_{MDT}$  is 0.49, without any lag (Fig. 4.13). The negative correlations between tides and stratification (Chapter 3, Fig. B.2) suggest that the relation between  $s_{MDT}$  and  $u_{tidal}$  partly reflects spring-neap variability in mixing and stratification.

An important question is whether the relationship between  $s_0$  and estuarine salinity also influences the along-estuary salinity gradient, given its expected role in modulating the strength of the gravitational circulation. To evaluate whether variations in  $s_0$  correspond to variations in along-estuary density gradient, we estimate the horizontal salinity gradient based on differences in bottom salinity between MDT (18 km inland) and BRB (40 km), expressed as  $\Delta s_{MB}/\Delta x$ , as shown on the map in Figure 4.1. There is a correlation of  $R = 0.53$  between  $s_0$  and the horizontal salinity gradient  $\Delta s_{MB}/\Delta x$ , without any time lag (Fig. 4.13).

We observed significant correlations between  $s_0$  and estuarine salinity. However, we cannot be conclusive as to why. We further address this in the Discussion section.



(a)

**Figure 4.12:** Time series of low-passed near-field bottom salinity  $s_0$  (NAV station) and estuarine bottom salinity (MDT, NMA, EEM, POR, and BRB stations). Salinities are normalised as deviations from the mean, normalised by maximum salinity for every location. The mean salinity, and the maximum deviation from that mean are reported for all stations.

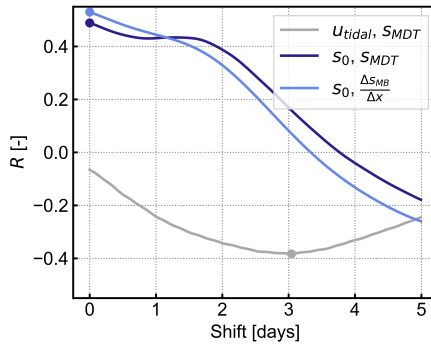


**Figure 4.13:** Best correlations for time shifts for the period shown in Figure 4.12. Correlations are reported for  $u_{tidal}$  and  $s_{MDT}$ ,  $s_0$  and  $s_{MDT}$ ,  $s_0$  and  $\frac{\Delta s_{MB}}{\Delta x}$ , where  $\Delta s_{MB}$  is the salinity difference between MDT (18 km inland) and BRB (40 km inland).

4

## 4.4 Discussion

The results show how the estuarine inflow conditions, set by parameters of the near-field region, vary due to the forcing of tides, winds, and atmospheric pressure. Here, we illustrate the conceptual picture of the salinity exchange between the near-field region and the estuary. Furthermore, we elaborate on how the changing boundary conditions might impact estuarine salinity and salt intrusion.

### 4.4.1 Conceptual picture: Freshwater re-entering the estuary

Tidal mixing decreases the near-field bottom salinity  $s_0$  with a time lag of 2.5 days between tidal velocities and the observed near-field salinity response (Fig. 4.8). This time lag suggests that freshwater from a newly ejected plume is not immediately mixed downward to the bottom within a single tidal cycle. While surface salinity in the near-field region reflects estuarine mixing and discharge, as captured by  $Ri_E$ , no corresponding relationship is found for bottom salinity. This suggests that the processes governing near-field bottom salinity are primarily driven by shelf dynamics rather than estuarine processes. Here, we propose a conceptual framework describing the mixing processes and transport pathways responsible for this delayed response, summarised in Figure 4.14.

In the near-field region, tidal mixing was reflected in the immediate increase of surface salinity with increasing tidal velocities. Previous studies in deeper systems have shown that the near-field mixing is characterised by positive entrainment due to the asymmetries in turbulent kinetic energy production between the fast-moving plume and the relatively stagnant ambient seawater (MacDonald and Geyer, 2004; McCabe et al., 2009). This leads to stronger salinity changes near the surface compared to the near-bottom, despite the high mixing rates.

With a scaling analysis, we investigate whether the near-field plume can mix

down to the bottom within a tidal cycle. Assuming a plume velocity of approximately  $1 \text{ m s}^{-1}$  and a distance of 6 km from the river mouth to the NAV mooring in the near-field, it would take roughly 6000 seconds (1.7 hours) for plume water to reach the observation point. For this water to mix vertically to the bottom (26 m depth) within that travel time, a vertical diffusivity of approximately  $K_v \approx H^2/T = 26^2/6000 = 0.1 \text{ m}^2 \text{ s}^{-1}$  would be required. At lift-off in the Fraser River plume MacDonald and Geyer (2004) estimate  $K_v \sim 4 \cdot 10^{-3} \text{ m}^2 \text{ s}^{-1}$  and in the Columbia River plume McCabe et al. (2009) found values around  $1 \cdot 10^{-2} \text{ m}^2 \text{ s}^{-1}$ . Thus, the diffusivity would need to be at least an order of magnitude greater than values observed in other systems for plume mixing to significantly affect bottom salinity at NAV within a single tidal cycle, which seems highly unlikely.

We observe a time lag of 2.5 days between  $u_{tidal}$  and  $s_0$  (Fig. 4.7c), which indicates the time lag is not caused by a single tidal excursion back and forth. With another scaling analysis, we infer the horizontal length scale associated with the plume mixing processes to influence  $s_0$ . Using estimates of vertical diffusivity from the mid-field plume ( $2 - 4 \cdot 10^{-3} \text{ m}^2 \text{ s}^{-1}$ , model data from Flores et al. (2020)) and a water column of 20 m depth, the mixing time scale would be 1.2-2.3 days. Assuming a subtidal bottom layer speed of order  $\sim 0.05 \text{ m s}^{-1}$ , based on the average subtidal alongshore flow at NAV and N2 (Figs. 4.11a and C.7a), water parcels could travel a net horizontal distance between 5 and 10 km in 1.2 to 2.3 days. The major axis tidal currents are shore parallel with an approximate excursion length of 15 km (Rijnsburger et al., 2021a), which means that the source water is presumably drawn from a region that extends 15 km up and down the coast, this region is mainly the mid-field region of the Rhine River plume. These results suggest that the inflow salinity depends on prior plume mixing. Just like plume outflow depends on estuarine mixing (Nash et al., 2009), estuarine inflow relates to plume mixing.

Based on our observations and the scaling presented above, we expect a pathway where freshwater is discharged from the river mouth to form a surface plume, and subsequently mixed to the bed in the mid-field plume and returns to the near-field at depth (Fig. 4.14). This pathway is also one of the pathways of estuarine inflow as found in idealised model simulations of Brasseale and MacCready (2021). Their Lagrangian particle tracking showed particles starting in the plume that travel away from the mouth at the surface, mix down into the lower layer, and are then transported back into the estuary. However, we observed that estuarine inflow happens primarily from the upcoast direction. This indicates a pathway slightly different from the Brasseale and MacCready (2021) study. During alongshore ebb currents when the flows are from downcoast direction, there is no estuarine inflow, so bottom waters bypass the estuary. This suggests that re-entering freshwater must first travel downcoast, then bypass the mouth in the upcoast direction, before possibly returning to the estuary. We hypothesise that strong cross-shore tidal straining causes this returning freshwater to overshoot the mouth. This suggests that in systems which are subject to this elliptical tidal

straining process (Visser et al., 1994; Souza and Simpson, 1996), the pathways of freshwater take as it makes its way back to the river mouth may be more complex than in less strained systems, and motivates more study in these types of tidally strained systems. These can be expected in systems around mid-latitudes, with a progressive tidal wave, and strong cross-shore density gradients (Flores et al., 2020).

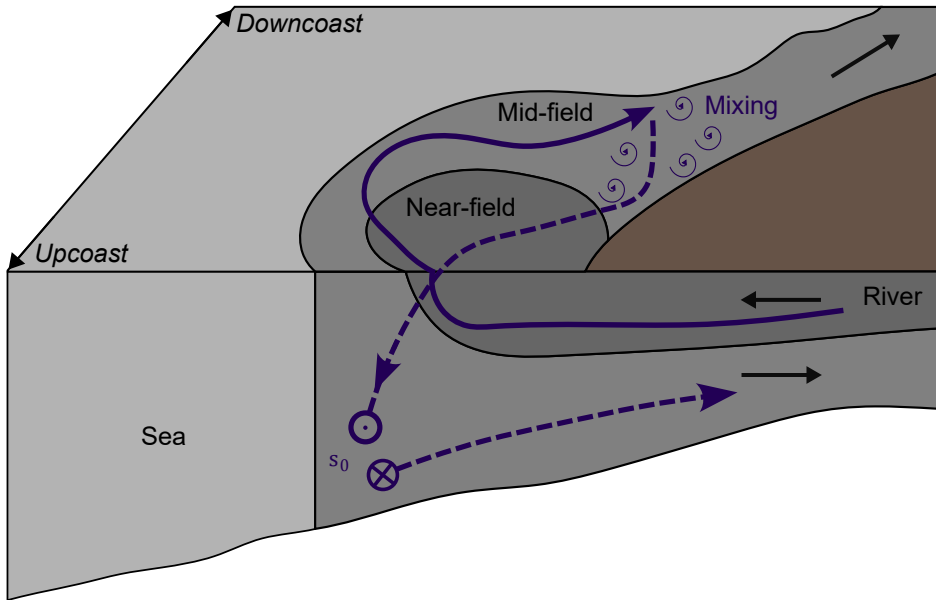


**Figure 4.14:** Conceptual sketch explaining the pathway of saline water between the estuary and the Rhine River plume. Solid lines indicate surface flows and dashed lines indicate flow in the lower layer. Adapted from Rijnsburger (2021), after Simpson (1997).

#### 4.4.2 The influence of near-field bottom salinity on estuarine salinity

Our results show that near-field bottom salinity  $s_0$  has a positive correlation with both estuarine salinity ( $s_{MDT}$ , 18 km from the mouth) and the along-estuary salinity gradient  $ds/dx$  (Fig. 4.13). The correlation between  $s_0$  and  $ds/dx$  ( $R = 0.53$ ) is stronger than between tidal velocity and  $ds/dx$  ( $R = -0.19$ ), and the correlation between  $s_0$  and  $s_{MDT}$  ( $R = 0.49$ ) also exceeds that of tidal velocity with  $s_{MDT}$  ( $R = -0.38$ ). These relationships suggest that variations in  $s_0$  may be more directly linked to estuarine salinity structure than to tides alone. Time-lag analysis, however, points toward a common tidal influence rather than a direct causal link. Tides lead  $s_0$  by about 2.5 days, while  $s_0$  and  $s_{MDT}$  vary in phase, and tides lead  $s_{MDT}$  by 3.0 days. The absence of a lag between  $s_0$  and  $s_{MDT}$ , despite the distance of 24 km between the stations, is inconsistent with a simple causal

propagation of salinity signals. By comparison, in Willapa Bay, salinity perturbations require about one day to travel 10 km into the estuary (Hickey et al., 2002). Taken together, the lag analysis suggests that both respond primarily to tidal forcing rather than one driving the other.

Even if the correlation arises from co-variation rather than a direct causal relationship, it still provides valuable insights for interpreting system behaviour. We expect that neap tides increase stratification, thereby increasing the exchange flow, and increasing the up-estuary salt flux. As the estuary lengthens, the reduced salinity gradient decreases the exchange flow again. And the reverse happens around spring tides. If on top of these fortnightly variations in exchange flow, the near-field bottom salinity also varies on this timescale, this could further enhance the variations in exchange flow on a fortnightly timescale, due to the variation in  $ds/dx$ .

A similar relation between near-field salinity and horizontal estuarine salinity gradient was observed in Willapa Bay (Hickey et al., 2002). However, a different mechanism causes the changes in offshore salinity. On the Washington shelf, a deep continental shelf, the offshore salinity variations are caused by upwelling and downwelling, which are independent of estuarine dynamics. In contrast, at the mouth of the Rhine-Meuse Delta estuary, wind and tidal mixing influence  $s_0$ . These same forcing mechanisms can also directly affect estuarine dynamics, making it difficult to disentangle cause and effect. This coupling introduces a potential feedback loop between near-field and estuarine dynamics, unique to shallow shelf environments such as the Dutch coast.

### 4.4.3 The role of wind on estuarine salinity

Earlier work in the Rhine-Meuse Delta estuary shows that coastal set-up drives salinity fluctuations inside the estuary, due to a saline water flux that is transported up-estuary (de Nijs et al., 2008; Wegman et al., 2025). This is a process that has been observed in many other estuaries as well (e.g., Ralston et al., 2008; Manca et al., 2014; Perales-Valdivia et al., 2018; Zhu et al., 2020; Cook et al., 2023).

We found that wind forcing modifies the cross-shore subtidal shear flow in the near-field. This flow pattern is linked to surface plume outflow and a return current (directed towards the estuary) at depth. Downwelling-favourable winds weaken this shear flow, while upwelling-favourable winds strengthen it. Assuming it has a connection to the estuarine exchange flow, downwelling winds reduce surface outflow and potentially the exchange flow, whereas upwelling winds enhance both surface outflow and bottom inflow. These responses are consistent with earlier studies (Giddings and MacCready, 2017; Geraeds et al., 2025). Whilst upwelling- and downwelling-favourable winds influence subtidal flows, these wind directions do not significantly impact the water level at the mouth of the estuary, in contrast to the onshore-directed wind.

We observed clear patterns between different wind conditions and subtidal flows (Fig. 4.11); however, we did not see any signal of changing bottom salin-

ity due to upwelling or downwelling water in the near-field. At NAV, which is located in the approach channel and therefore has no closed coastal boundary, the residual cross-shore profile (Fig. 4.11b) is still dominated by the exchange flow pattern, with outflow at the surface and inflow at depth. In the Rhine River plume, upwelling and downwelling-favourable winds mainly impact the plume thickness (Keyzer, 2025). In contrast to deep continental shelves, such as the Washington shelf (Hickey et al., 2002; Giddings and MacCready, 2017; Brasseale and MacCready, 2025), the North Sea is a shallow system with no nearby source of deep, cold, saline waters that can upwell, resulting in a weak horizontal salinity gradient. The source of saline water beneath the plume is most likely the English Channel, containing Atlantic-origin water mixed with plume waters from French and English rivers (Kelly-Gerreyn et al., 2006; Pietrzak et al., 2011; van der Molen and Pätsch, 2022). We found that near-field bottom salinity is strongly modulated by the strength of the tidal currents, and to a lesser extent by wind mixing. Any secondary influence of upwelling or downwelling cannot be clearly identified with the present dataset. The importance of alongshore winds on the bottom salinity variability needs further investigation, for example, through numerical modelling using a realistic domain combined with idealised forcing.

## 4.5 Conclusions

This chapter investigates what influences the estuarine inflow conditions, using field observations from a frictional plume–estuary system on a shallow shelf sea: the Rhine River plume and the Rhine-Meuse Delta estuary. We focused on how wind and tidal forcing influence the near-field region, which is the dynamical boundary condition for the estuary.

Bottom salinity in the near-field is modulated by the intensity of tide-driven mixing. A lag of approximately 2.5 days between variations in mixing intensity, based on the tidal velocities, and corresponding variations in bottom salinity suggests that salinity variability in the near-field is primarily governed by mixing processes occurring in the mid-field plume. This lag is consistent with the time scales of vertical mixing and horizontal advection. These results suggest that the salinity inflow depends on plume mixing.

In contrast to observations from deeper continental shelves, upwelling- and downwelling-favourable winds do not show a discernible influence on near-field bottom salinity. The shallow, wide North Sea shelf is different, where the absence of a deep source of dense water leads to a weaker cross-shelf salinity gradient. Consistent with previous modelling studies of the Rhine River plume, however, our observations show that these winds do affect plume advection and modify the subtidal velocity structure at the river mouth. While the overall influence of wind on bottom salinity is limited, isolated events reveal short-term salinity decreases following periods of strong winds, exceeding  $10 \text{ m s}^{-1}$ .

The observed variability in the salinity of the seaward boundary may influ-

ence estuarine salinity intrusion. However, quantifying the extent of this influence remains challenging, as tides and wind drive both the estuarine response and the near-field dynamics.

Our results support a conceptual picture of the processes setting the lower-layer salinity at the river mouth. Fresh river water is exported in the plume, mixed into the lower layer, and partly returned to the mouth, where it sets the inflow salinity.



# 5

## Conclusions and Outlook

### 5.1 Conclusions

Salt intrusion poses an increasing threat to estuaries and deltas worldwide, driven by consequences of climate change such as sea-level rise and more frequent and severe droughts. This thesis aimed to improve the understanding of salt intrusion dynamics in the complex, human-influenced Rhine–Meuse Delta (RMD), particularly under drought conditions. The thesis is based on an extensive field campaign carried out throughout the RMD, combining moored observations with shipborne measurements.

#### 5.1.1 Relation between flow, stratification, and turbulence

The second chapter of this thesis examined intratidal flow patterns and turbulence in the deep, stratified section of the RMD (Rotterdam Waterway), using field observations of velocity, density, and turbulence. The results showed that maxima in velocity shear often coincide with the strongest density stratification throughout the water column, as stratification suppresses vertical exchange between inflowing and outflowing layers. This means that they develop different flow speeds in the different layers, with associated velocity shear at their boundaries, around the pycnocline. These observations highlight the importance of stratification and the associated suppression of turbulence for flow patterns in the Rotterdam Waterway. The frequent occurrence of strong stratification with respect to the velocity shear ( $Ri > 0.25$ ) may be attributed to the overdeepened Rotterdam Waterway, where the water depth is maintained at approximately  $-16$  m NAP through regular dredging (Rijkswaterstaat, 2025). Similar to other urbanised deltas, such as the Duwamish River Estuary (McKeon et al., 2021), the Rotterdam Waterway is overdeepened to accommodate ship traffic. This may result in the inability of the bottom boundary layer turbulence to influence mixing at the

interface.

Elevated turbulence around the pycnocline during flood was associated with mid-depth jets, yet the salt wedge remained stable over the full tidal cycle. Observed patterns of stratification, shear, and turbulence support the use of the gradient Richardson number as an indicator of vertical mixing in this estuary. After calibration, four Richardson-number-based parameterisations were shown to capture the statistical behaviour of observation-based estimates of vertical diffusivity reasonably well. Accounting for the effect of the limited water depth using a parabolic shape function did not improve the performance of these parameterisations. The results and dataset presented here have the potential to improve the representation of vertical mixing in estuarine salt intrusion models.

### 5.1.2 Drivers of salt intrusion length during drought

The third chapter of this thesis focused on subtidal salt intrusion dynamics during a historic drought, providing insight into how salt intrusion length responds to different forcing mechanisms over multi-day timescales. The dominant control on subtidal salt intrusion length ( $L_2$ , based on the 2 PSU isohaline) is the Rhine River discharge, with a clear power-law relationship after averaging over four days to filter short-term variability.

Coastal set-up was found to be a secondary but important driver. Subtidal variations in sea level, linked to wind and atmospheric pressure over the North Sea, can cause salt intrusion limits to shift upstream or downstream by distances comparable to the tidal excursion. Local onshore winds were identified as particularly influential in this set-up mechanism. In contrast, spring–neap variations in tidal range had no discernible influence on subtidal salt intrusion length.

The side branches are governed by different physical processes than the main river, with downstream salinity as the dominant influence. Accounting for these branches separately is essential to capture the highly variable downstream boundary condition, a consideration that may be relevant for other deltas and complex estuarine systems.

### 5.1.3 The near-field plume region as a dynamic boundary condition

The fourth chapter of this thesis investigated the dynamic boundary at the mouth of the estuary, focusing on the velocity and salinity variations in the near-field Rhine River plume and its influence on estuarine salinity. Bottom salinity in the near-field is modulated by the intensity of tide-driven mixing. A lag of approximately 2.5 days between variations in mixing intensity, based on the tidal velocities, and corresponding variations in bottom salinity suggests that salinity variability in the near-field is primarily governed by mixing processes occurring in the mid-field plume. This lag is consistent with the time scales of vertical mixing and horizontal advection. These results suggest that the salinity inflow de-

depends on plume mixing, just like plume outflow depends on estuarine mixing Nash et al. (2009). In contrast to observations from deeper continental shelf regions, upwelling- and downwelling-favourable winds do not affect near-field bottom salinity. However, consistent with previous modelling studies of the Rhine River plume, our observations indicate that these winds do drive plume advection and modify the subtidal velocity boundary at the mouth. While the overall influence of wind on bottom salinity is limited, isolated events reveal short-term salinity decreases following periods of strong winds. Although such boundary variability likely impacts estuarine salt intrusion, its effect is difficult to isolate, as tides and wind simultaneously drive both near-field and estuarine dynamics.

#### 5.1.4 Concluding remarks

Together, the findings of this thesis provide new insights into estuarine salt intrusion dynamics in a complex, engineered delta, based on observational data from the Rhine-Meuse Delta. Observations of intratidal flow, density, and turbulence patterns highlight the importance of velocity shear-induced turbulence generation and turbulence damping at the pycnocline. Fitting of Richardson-number-based parameterisations shows promising results for the statistical representation of turbulence in estuarine models.

Idealised subtidal relations between salt intrusion and forcing of river discharge and set-up were found to hold in the main estuary. However, side branches with distinct dynamics must be treated separately, where the downstream boundary is a crucial control. These dynamic boundary conditions are also relevant for the main estuary.

This thesis provides one of the first insights into the main variations in this dynamic boundary condition in a shallow shelf sea, where the salinity changes in the near-field region are imposed by spring-neap variations of mid-field plume mixing. Overall, despite the short duration of the observations, this study has revealed key dynamics in a highly complex system. In addition to the new insights, the data presented in this thesis point to several important directions for future research.

## 5.2 Recommendations for future research

### 5.2.1 Investigating the absence of a spring-neap signal in salt intrusion

Observations collected for this thesis did not show a spring-neap dependence of salt intrusion length in the Rhine-Meuse Delta (RMD) estuary (Chapter 3). The reason for this lack of variation remains inconclusive. Here, we discuss how the two hypotheses that were proposed in the discussion of that chapter could be tested:

1. The relative strength of the dominant salt transport mechanisms, estuarine exchange flow and tidal dispersion, may vary inversely over a spring–neap cycle, potentially masking the spring–neap variability in salt intrusion.
2. The estuarine adjustment timescale may be comparable to, or larger than, the duration of the spring–neap cycle itself, preventing a fully developed response to varying tidal conditions.

To assess whether salt transport by exchange flow and tidal dispersion are similar in magnitude but vary in phase over a spring–neap cycle and potentially cancel each other out, a realistic hindcast simulation using the Delft3D-FM RMD model (Gerritsma et al., 2025) could be employed. The relative contributions of different salt transport mechanisms can be diagnosed using a salt flux decomposition (Lerczak et al., 2006). The model output would allow evaluation of how exchange flow and tidal dispersion evolve during a spring–neap cycle and whether their temporal variability explains the muted response in salt intrusion length.

Two idealised modelling studies in the RMD have shown that the dominant transport mechanisms vary along the length of the estuary (Dijkstra et al., 2022; Biemond et al., 2025). Reasons for this are the differences in water depth, discharge, phases of the tidal currents, and characteristics of the salinity distribution between those branches Biemond et al. (2025). Given this spatial variability, it is essential to evaluate the transport mechanisms throughout the estuary for the branches of interest.

If the first hypothesis is not true, then the response times of the estuary could be tested with a realistic model domain, but with idealised forcing. Based on theoretical formulations for adjustment times described by MacCready (2007), the response times were estimated in the Discussion of Chapter 3. The estimated response times for the main system and the Lek branch are 3–4 days, and for the Hollandsche IJssel, it was approximately 15 days. An idealised model of the RMD, based on a low discharge scenario, showed response times in line with our estimates (Biemond et al., 2025). By fitting field observations in the Hudson Estuary to a linearised model, Lerczak et al. (2009) found that estimated response time scales with the theoretical prediction ( $T_{ADJ} = \frac{LA}{Q}$ ), but it is 3–4 times larger than in the theoretical model presented by MacCready (2007). To evaluate the response times more accurately for the dataset analysed in Chapter 3, a hindcast could be done with the RMD model, but with idealised discharge forcing and without coastal set-up (the most important drivers in the RMD). A boundary condition with a realistic spring–neap cycle could be used to see whether the estuary length significantly responds to this.

For this question, it should be noted that the response time varies between the different branches of the RMD, due to the differences in discharge and salinity gradients, among other factors (Biemond et al., 2025). So the overall response time also depends on the total Rhine River discharge, because response time itself is dependent on  $Q_R$ , and  $Q_R$  determines which branches are saline to begin with. During high discharge periods, the salt intrusion length may be more correlated

to the spring-neap tidal cycle, since this decreases estuarine response times for two reasons in the RMD. Therefore, it is recommended to test the sensitivity of response time across various discharge regimes.

### 5.2.2 Testing causal relations between near-field bottom salinity and estuarine salinity

Results from Chapter 4 showed a correlation between near-field bottom salinity and estuarine salinity (up to 27 km from the mouth) and along-estuary salinity gradients. However, the dataset does not allow one to prove whether the changes in near-field bottom salinity and estuarine salinity gradient ( $ds/dx$ ) are a causal effect, or whether both respond independently to a common external driver, such as tidal forcing. However, the increased  $ds/dx$  can still be important for the observed dynamics in the RMD. This could be tested with an idealised model with a synthetic variation in the near-field salinity boundary. While near-field salinity values can vary synthetically within bounds of the observed values, the tidal conditions would be given according to a realistic hindcast of the spring-neap variability.

### 5.2.3 Next steps and applications of the turbulence analysis

Results from Chapter 2 demonstrated that the Rotterdam Waterway is strongly stratified, which suppresses turbulence at the interface. Future research could explore the implications of this suppression for estuarine dynamics in the Rotterdam Waterway. One possible consequence is reduced entrainment of freshwater into the saline layer, which may in turn enhance salt intrusion. A useful approach to evaluate this would be to estimate the entrainment coefficient, or interfacial drag coefficient (MacDonald and Geyer, 2004), and compare it with values reported for other estuarine systems.

Detailed turbulence datasets in estuaries are scarce. The dataset presented in Chapter 2 provides an opportunity to improve and validate numerical models. First, the RMD model (Gerritsma et al., 2025) could be validated against the dataset, and the turbulence data gives the opportunity to improve the  $k - \varepsilon$  turbulence closure. Second, the presented results on Richardson number parameterisations create opportunities to test those parameterisations in idealised estuarine models, such as those by MacCready (2004) and Biemond et al. (2022). These models typically represent vertical mixing using constant eddy viscosity and diffusivity, or simple scaling based on geometry and tidal forcing. However, Biemond (2024) argues that representing turbulence as a stochastic parameterisation could be more suitable in such models than the widely used  $k - \varepsilon$  closures, due to their deterministic nature. Given the short runtime of these models, ensemble simulations are feasible. The results presented in Chapter 2 are promising for the development and application of stochastic parameterisations for vertical diffusivity.

While the stochastic representation between  $Ri$  and vertical diffusivity shows promising results, the individual profiles do not fit perfectly. Further research could identify the reasons for this discrepancy between observations and parameterisations. Internal waves were observed in various shipborne measurements throughout the estuary. Quantifying the contribution of internal waves to turbulence generation in the RMD estuary could be a valuable next step. Their role could be further investigated using the current dataset, and possibly with additional observations.

#### 5.2.4 Characterising mixing from internal waves and shear-instabilities in the near-field river plume

Internal waves have also been observed in the near-field river plume region (Fig. 5.1). Earlier studies in the Rhine River plume, presented internal wave observations from the near- and mid-field, showing their presence ahead of the tidal plume fronts (Rijnsburger et al., 2021b). Their study suggested that the internal solitary wave packets were generated by multiple tidal plume fronts during one tidal cycle.

The study by Rijnsburger et al. (2021b) was based on remotely sensed images, in combination with moored observations in the mid-field. Looking at the near-field echosounder combined with radar or satellite data, more insights into the internal wave properties in the near-field could be gained, and whether they propagate to the mid-field.

The field campaign described in Chapter 4 also collected high-resolution echosounder data with ADCPs. The data from the ADCPs revealed internal waves in the near-field, with a period of roughly 2 minutes (Fig. 5.1a). Another snapshot suggests internal wave breaking (Fig. 5.1b). Furthermore, these echosounder data revealed smaller-scale structures such as Kelvin-Helmholtz instabilities (Fig. 5.1c). Together with turbulence estimates, which could be done with the raw ADCP data (Guerra and Thomson, 2017), it could also be estimated to what extent these features contribute to the turbulence levels in the near-field river plume.

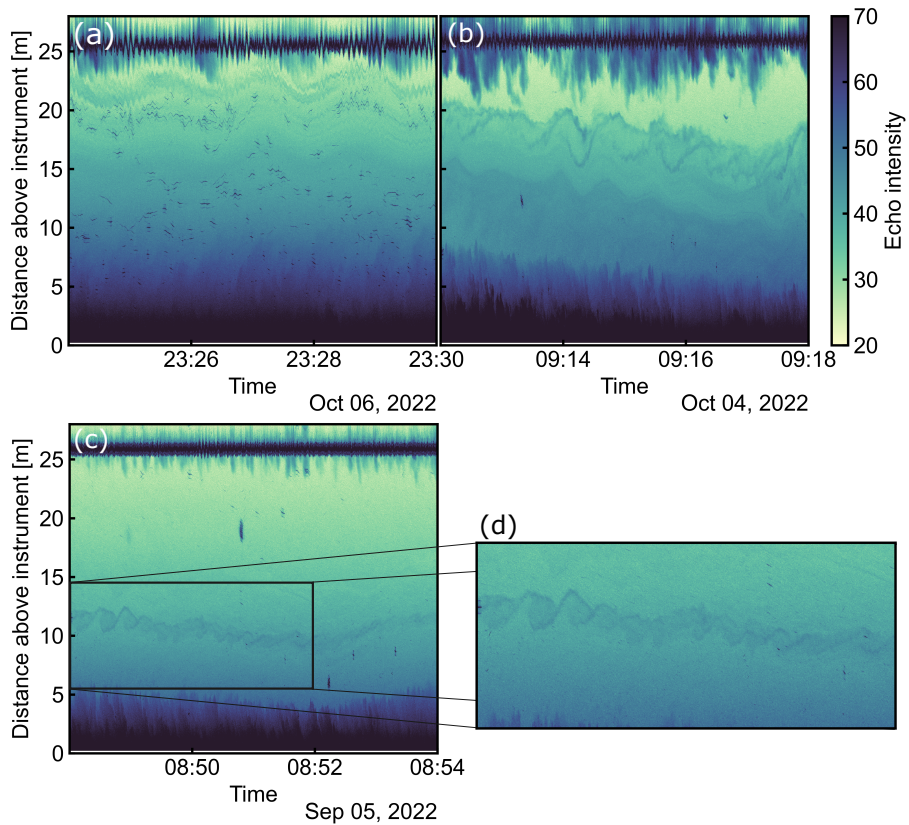


**Figure 5.1:** Several instances of echosounder data collected in the near-field Rhine River plume (at NAV, see Figure 4.1 in Chapter 4). (a) Internal waves with a period of approximately 2 minutes, (b) breaking internal waves, (c) Kelvin-Helmholtz instabilities, (d) zoomed in to the instabilities.



## References

- Abood, K. A. : Circulation in the Hudson Estuary, *Annals of the New York Academy of Sciences*, 250, 39–111, doi:10.1111/j.1749-6632.1974.tb43895.x, 1974.
- Alebregtse, N. C. and de Swart, H. E. : Effect of river discharge and geometry on tides and net water transport in an estuarine network, an idealized model applied to the Yangtze Estuary, *Continental Shelf Research*, 123, 29–49, doi:10.1016/j.csr.2016.03.028, 2016.
- Allen, J. T. , Keen, P. W. , Gardiner, J. , Quartley, M. , and Quartley, C. : A new salinity equation for sound speed instruments: New salinity equation for sound speed instruments, *Limnology and Oceanography: Methods*, 15, 810–820, doi:10.1002/lom3.10203, 2017.
- Arenas-López, J. P. and Badaoui, M. : Stochastic modelling of wind speeds based on turbulence intensity, *Renewable Energy*, 155, 10–22, doi:10.1016/j.renene.2020.03.104, 2020.
- Basdurak, N. B. , Huguenard, K. D. , Valle-Levinson, A. , Li, M. , and Chant, R. J. : Parameterization of mixing by secondary circulation in estuaries, *Journal of Geophysical Research: Oceans*, 122, 5666–5688, doi:10.1002/2016JC012328, 2017.
- Basdurak, N. B. , Burchard, H. , and Schuttelaars, H. M. : A local eddy viscosity parameterization for wind-driven estuarine exchange flow, Part II: Entrainment, *Progress in Oceanography*, 219, 103–166, doi:https://doi.org/10.1016/j.pocean.2023.103166, 2023.
- Bauer, W. , Chandramouli, P. , Li, L. , and Mémin, E. : Stochastic representation of mesoscale eddy effects in coarse-resolution barotropic models, *Ocean Modelling*, 151, 101–166, doi:10.1016/j.ocemod.2020.101646, 2020.
- Biamond, B. , de Swart, H. E. , Dijkstra, H. A. , and Díez-Minguito, M. : Estuarine Salinity Response to Freshwater Pulses, *Journal of Geophysical Research: Oceans*, 127, e2022JC018669, doi:10.1029/2022JC018669, 2022.
- Biamond, B. , Kranenburg, W. M. , Huismans, Y. , de Swart, H. E. , and Dijkstra, H. A. : Dynamics of salt intrusion in complex estuarine networks: an idealised model applied to the Rhine–Meuse Delta, *Ocean Science*, 21, 261–281, doi:10.5194/os-21-261-2025, 2025.
- Biamond, W. T. : Mechanisms of salt intrusion in estuarine channels and networks, Ph.d. thesis, Utrecht University, Utrecht, The Netherlands, see Chapter 7, 2024.
- Bowden, K. F. : Turbulent mixing in estuaries, *Ocean Management*, 6, 117–135, doi:10.1016/0302-184X(81)90033-0, 1981.
- Bowen, M. M. and Geyer, W. R. : Salt transport and the time-dependent salt bal-

- ance of a partially stratified estuary, *Journal of Geophysical Research: Oceans*, 108, doi:<https://doi.org/10.1029/2001JC001231>, 2003.
- Brasseale, E. and MacCready, P. : The shelf sources of estuarine inflow, *Journal of Physical Oceanography*, doi:[10.1175/JPO-D-20-0080.1](https://doi.org/10.1175/JPO-D-20-0080.1), 2021.
- Brasseale, E. and MacCready, P. : Seasonal Wind Stress Direction Influences Source and Properties of Inflow to the Salish Sea and Columbia River Estuary, *Journal of Geophysical Research: Oceans*, 130, e2024JC022024, doi:[10.1029/2024JC022024](https://doi.org/10.1029/2024JC022024), 2025.
- Chant, R. J. , Geyer, W. R. , Houghton, R. , Hunter, E. , and Lerczak, J. : Estuarine Boundary Layer Mixing Processes: Insights from Dye Experiments\*, *Journal of Physical Oceanography*, 37, 1859–1877, doi:[10.1175/jpo3088.1](https://doi.org/10.1175/jpo3088.1), publisher: American Meteorological Society, 2007.
- Chatwin, P. C. : Some remarks on the maintenance of the salinity distribution in estuaries, *Estuarine and Coastal Marine Science*, 4, 555–566, doi:[https://doi.org/10.1016/0302-3524\(76\)90030-X](https://doi.org/10.1016/0302-3524(76)90030-X), 1976.
- Chawla, A. , Jay, D. A. , Baptista, A. M. , Wilkin, M. , and Seaton, C. : Seasonal variability and estuary-shelf interactions in circulation dynamics of a river-dominated estuary, *Estuaries and Coasts*, 31, 269–288, doi:[10.1007/s12237-007-9022-7](https://doi.org/10.1007/s12237-007-9022-7), 2008.
- Chen, W. and de Swart, H. E. : Dynamic links between shape of the eddy viscosity profile and the vertical structure of tidal current amplitude in bays and estuaries, *Ocean Dynamics*, 66, 299–312, doi:[10.1007/s10236-015-0919-6](https://doi.org/10.1007/s10236-015-0919-6), 2016.
- Conroy, T. , Sutherland, D. A. , and Ralston, D. K. : Estuarine Exchange Flow Variability in a Seasonal, Segmented Estuary, *Journal of Physical Oceanography*, 50, 595–613, doi:[10.1175/JPO-D-19-0108.1](https://doi.org/10.1175/JPO-D-19-0108.1), 2020.
- Cook, S. E. , Warner, J. C. , and Russell, K. L. : A numerical investigation of the mechanisms controlling salt intrusion in the Delaware Bay estuary, *Estuarine, Coastal and Shelf Science*, 283, 108 257, doi:[10.1016/j.ecss.2023.108257](https://doi.org/10.1016/j.ecss.2023.108257), 2023.
- Cover, T. M. and Thomas, J. A. : *Elements of Information Theory*, Wiley-Interscience, Hoboken, NJ, 2nd edn., doi:[10.1002/047174882X](https://doi.org/10.1002/047174882X), 2006.
- Cox, J. R. , Huismans, Y. , Knaake, S. M. , Leuven, J. R. F. W. , Vellinga, N. E. , van der Vegt, M. , Hoitink, A. J. F. , and Kleinhans, M. G. : Anthropogenic Effects on the Contemporary Sediment Budget of the Lower Rhine-Meuse Delta Channel Network, *Earth's Future*, 9, e2020EF001869, doi:[10.1029/2020EF001869](https://doi.org/10.1029/2020EF001869), 2021.
- Dai, Z. , Chu, A. , Stive, M. , Zhang, X. , and Yan, H. : Unusual Salinity Conditions in the Yangtze Estuary in 2006: Impacts of an Extreme Drought or of the Three Gorges Dam?, *AMBIO*, 40, 496–505, doi:[10.1007/s13280-011-0148-2](https://doi.org/10.1007/s13280-011-0148-2), 2011.
- Dangendorf, S. , Calafat, F. M. , Arns, A. , Wahl, T. , Haigh, I. D. , and Jensen, J. : Mean sea level variability in the North Sea: Processes and implications, *Journal of Geophysical Research: Oceans*, 119, doi:<https://doi.org/10.1002/2014JC009901>, 2014.
- de Boer, G. J. , Pietrzak, J. D. , and Winterwerp, J. C. : On the vertical structure

- of the Rhine region of freshwater influence, *Ocean Dynamics*, 56, 198–216, doi:10.1007/s10236-005-0042-1, 2006.
- de Boer, G. J. , Pietrzak, J. D. , and Winterwerp, J. C. : Using the potential energy anomaly equation to investigate tidal straining and advection of stratification in a region of freshwater influence, *Ocean Modelling*, 22, 1–11, doi:10.1016/j.ocemod.2007.12.003, 2008.
- de Nijs, M. A. J. and Pietrzak, J. D. : On total turbulent energy and the passive and active role of buoyancy in turbulent momentum and mass transfer, *Ocean Dynamics*, 62, 849–865, doi:10.1007/s10236-012-0536-6, 2012.
- de Nijs, M. A. J. , Winterwerp, J. C. , and Pietrzak, J. D. : Chapter 25 SPM variations in a harbour basin, in: *Sediment and Ecohydraulics*, edited by Kusuda, T. , Yamanishi, H. , Spearman, J. , and Gailani, J. Z. , vol. 9 of *Proceedings in Marine Science*, pp. 357–378, Elsevier, doi:https://doi.org/10.1016/S1568-2692(08)80027-7, 2008.
- de Nijs, M. A. J. , Pietrzak, J. D. , and Winterwerp, J. C. : Advection of the Salt Wedge and Evolution of the Internal Flow Structure in the Rotterdam Waterway, *Journal of Physical Oceanography*, 41, 3–27, doi:10.1175/2010jpo4228.1, 2011.
- de Wilde, H. : Tidal phase differences in multi-branch systems and their effect on salt intrusion, Delft University of Technology, master thesis, 2024.
- Dijkstra, Y. M. and Schuttelaars, H. M. : A unifying approach to subtidal salt intrusion modeling in tidal estuaries, *Journal of Physical Oceanography*, 51, 147–167, doi:10.1175/JPO-D-20-0006.1, 2021.
- Dijkstra, Y. M. , Schuttelaars, H. M. , and Kranenburg, W. M. : Salt Transport Regimes Caused by Tidal and Subtidal Processes in Narrow Estuaries, *Journal of Geophysical Research: Oceans*, 127, e2021JC018391, doi:10.1029/2021JC018391, 2022.
- Eslami, S. , Hoekstra, P. , Nguyen Trung, N. , Ahmed Kantoush, S. , Van Binh, D. , Duc Dung, D. , Tran Quang, T. , and van der Vegt, M. : Tidal amplification and salt intrusion in the Mekong Delta driven by anthropogenic sediment starvation, *Scientific Reports*, 9, 18 746, doi:10.1038/s41598-019-55018-9, 2019.
- Eslami, S. , Hoekstra, P. , Kernkamp, H. W. J. , Nguyen Trung, N. , Do Duc, D. , Nguyen Nghia, H. , Tran Quang, T. , van Dam, A. , Darby, S. E. , Parsons, D. R. , Vasilopoulos, G. , Braat, L. , and van der Vegt, M. : Dynamics of salt intrusion in the Mekong Delta: results of field observations and integrated coastal–inland modelling, *Earth Surface Dynamics*, 9, 953–976, doi:10.5194/esurf-9-953-2021, 2021a.
- Eslami, S. , Hoekstra, P. , Minderhoud, P. S. J. , Trung, N. N. , Hoch, J. M. , Sultanudjaja, E. H. , Dung, D. D. , Tho, T. Q. , Voepel, H. E. , Woillez, M.-N. , and van der Vegt, M. : Projections of salt intrusion in a mega-delta under climatic and anthropogenic stressors, *Communications Earth & Environment*, 2, 142, doi:10.1038/s43247-021-00208-5, 2021b.
- Fischer, H. : Mass transport mechanisms in partially stratified estuaries, *Journal*

- of Fluid Mechanics, 53, 671–687, doi:10.1017/S0022112072000412, 1972.
- Flores, R. P. , Rijnsburger, S. , Horner-Devine, A. R. , Souza, A. J. , and Pietrzak, J. D. : The impact of storms and stratification on sediment transport in the Rhine region of freshwater influence, *Journal of Geophysical Research: Oceans*, 122, 4456–4477, doi:10.1002/2016jc012362, 2017.
- Flores, R. P. , Rijnsburger, S. , Horner-Devine, A. R. , Kumar, N. , Souza, A. J. , and Pietrzak, J. D. : The Formation of Turbidity Maximum Zones by Minor Axis Tidal Straining in Regions of Freshwater Influence, *Journal of Physical Oceanography*, 50, 1265–1287, doi:10.1175/JPO-D-18-0264.1, 2020.
- Fong, D. A. and Geyer, W. R. : Response of a river plume during an upwelling favorable wind event, *Journal of Geophysical Research: Oceans*, 106, 1067–1084, doi:10.1029/2000JC900134, 2001.
- Fong, D. A. , Geyer, W. R. , and Signell, R. P. : The wind-forced response on a buoyant coastal current: Observations of the western Gulf of Maine plume, *Journal of Marine Systems*, 12, 69–81, doi:10.1016/S0924-7963(96)00089-9, 1997.
- Freire, L. S. and Chamecki, M. : A one-dimensional stochastic model of turbulence within and above plant canopies, *Agricultural and Forest Meteorology*, 250–251, 9–23, doi:10.1016/j.agrformet.2017.12.211, 2018.
- Garcia, A. M. P. , Geyer, W. R. , and Randall, N. : Exchange Flows in Tributary Creeks Enhance Dispersion by Tidal Trapping, *Estuaries and Coasts*, 45, 363–381, doi:10.1007/s12237-021-00969-4, 2022.
- Garvine, R. W. : A dynamical system for classifying buoyant coastal discharges, *Continental Shelf Research*, 15, 1585–1596, doi:10.1016/0278-4343(94)00065-U, 1995.
- Geraeds, M. , Pietrzak, J. , Gerritsma, A. , Verlaan, M. , and Katsman, C. A. : Assessing the importance of the near-field plume state on estuarine dynamics under varying wind conditions, doi:10.22541/essoar.174534309.94419306/v1, 2025.
- Gerritsma, A. , Verlaan, M. , Geraeds, M. , Huismans, Y. , and Pietrzak, J. : The Effects of a Storm Surge Event on Salt Intrusion: Insights From the Rhine-Meuse Delta, *Journal of Geophysical Research: Oceans*, 130, e2024JC021520, doi:10.1029/2024JC021520, 2025.
- Gerz, T. and Schumann, U. : A possible explanation of countergradient fluxes in homogeneous turbulence, *Theoretical and Computational Fluid Dynamics*, 8, 169–181, doi:10.1007/BF00418056, 1996.
- Geyer, W. R. : Influence of Wind on Dynamics and Flushing of Shallow Estuaries, *Estuarine, Coastal and Shelf Science*, 44, 713–722, 1997.
- Geyer, W. R. and Farmer, D. M. : Tide-Induced Variation of the Dynamics of a Salt Wedge Estuary, *Journal of Physical Oceanography*, 19, 1060–1072, 1989.
- Geyer, W. R. and MacCready, P. : The Estuarine Circulation, *Annual Review of Fluid Mechanics*, 46, 175–197, doi:10.1146/annurev-fluid-010313-141302, 2014.

- Geyer, W. R. and Ralston, D. K. : The Dynamics of Strongly Stratified Estuaries, in: *Treatise on Estuarine and Coastal Science*, pp. 37–51, Elsevier, doi:10.1016/B978-0-12-374711-2.00206-0, 2011.
- Geyer, W. R. and Smith, J. D. : Shear Instability in a Highly Stratified Estuary, *Journal of Physical Oceanography*, 17, 1668–1679, doi:10.1175/1520-0485(1987)017<1668:SIIAHS>2.0.CO;2, 1987.
- Geyer, W. R. , Trowbridge, J. H. , and Bowen, M. M. : The Dynamics of a Partially Mixed Estuary, *Journal of Physical Oceanography*, 30, 2035 – 2048, doi:10.1175/1520-0485(2000)030<2035:TDOAPM>2.0.CO;2, 2000.
- Geyer, W. R. , Scully, M. E. , and Ralston, D. K. : Quantifying vertical mixing in estuaries, *Environmental Fluid Mechanics*, 8, 495–509, doi:10.1007/s10652-008-9107-2, 2008.
- Geyer, W. R. , Lavery, A. C. , Scully, M. E. , and Trowbridge, J. H. : Mixing by shear instability at high Reynolds number, *Geophysical Research Letters*, 37, 2010GL045 272, doi:10.1029/2010GL045272, 2010.
- Geyer, W. R. , Ralston, D. K. , and Holleman, R. C. : Hydraulics and mixing in a laterally divergent channel of a highly stratified estuary, *Journal of Geophysical Research: Oceans*, 122, 4743–4760, doi:10.1002/2016JC012455, 2017.
- Geyer, W. R. , Ralston, D. K. , and Chen, J.-L. : Mechanisms of Exchange Flow in an Estuary With a Narrow, Deep Channel and Wide, Shallow Shoals, *Journal of Geophysical Research: Oceans*, 125, e2020JC016 092, doi:https://doi.org/10.1029/2020JC016092, e2020JC016092 2020JC016092, 2020.
- Giddings, S. N. and MacCready, P. : Reverse Estuarine Circulation Due to Local and Remote Wind Forcing, Enhanced by the Presence of Along-Coast Estuaries, *Journal of Geophysical Research: Oceans*, 122, 10 184–10 205, doi:10.1002/2016JC012479, 2017.
- Giddings, S. N. , Fong, D. A. , and Monismith, S. G. : Role of straining and advection in the intratidal evolution of stratification, vertical mixing, and longitudinal dispersion of a shallow, macrotidal, salt wedge estuary, *Journal of Geophysical Research: Oceans*, 116, doi:10.1029/2010JC006482, 2011.
- Godin, G. : *The analysis of tides*, University of Toronto Press [Toronto], [Toronto], section: xxi, 264 pages illustrations 26 cm, 1972.
- Guerra, M. and Thomson, J. : Turbulence Measurements from Five-Beam Acoustic Doppler Current Profilers, *Journal of Atmospheric and Oceanic Technology*, 34, 1267 – 1284, doi:10.1175/JTECH-D-16-0148.1, 2017.
- Hammond, J. C. , Simeone, C. , Hecht, J. S. , Hodgkins, G. A. , Lombard, M. , McCabe, G. , Wolock, D. , Wiczorek, M. , Olson, C. , Caldwell, T. , Dudley, R. , and Price, A. N. : Going Beyond Low Flows: Streamflow Drought Deficit and Duration Illuminate Distinct Spatiotemporal Drought Patterns and Trends in the U.S. During the Last Century, *Water Resources Research*, 58, e2022WR031 930, doi:10.1029/2022WR031930, 2022.
- Hansen, D. V. and Rattray, M. : Gravitational circulation in straits and estuaries,

- 1965.
- Hickey, B. M. and Banas, N. S. : Oceanography of the U.S. Pacific Northwest Coastal Ocean and estuaries with application to coastal ecology, *Estuaries*, 26, 1010–1031, doi:10.1007/BF02803360, 2003.
- Hickey, B. M. , Zhang, X. , and Banas, N. : Coupling between the California Current System and a coastal plain estuary in low riverflow conditions, *Journal of Geophysical Research: Oceans*, 107, doi:10.1029/1999JC000160, 2002.
- Hill, A. E. and Souza, A. J. : Tidal dynamics in channels: 2. Complex channel networks, *Journal of Geophysical Research: Oceans*, 111, 2006JC003670, doi:10.1029/2006JC003670, 2006.
- Holleman, R. C. , Geyer, W. R. , and Ralston, D. K. : Stratified Turbulence and Mixing Efficiency in a Salt Wedge Estuary, *Journal of Physical Oceanography*, 46, 1769–1783, doi:10.1175/jpo-d-15-0193.1, 2016.
- Hong, B. , Liu, Z. , Shen, J. , Wu, H. , Gong, W. , Xu, H. , and Wang, D. : Potential physical impacts of sea-level rise on the Pearl River Estuary, China, *Journal of Marine Systems*, 201, 103–245, doi:https://doi.org/10.1016/j.jmarsys.2019.103245, 2020.
- Horner-Devine, A. R. , Hetland, R. D. , and MacDonald, D. G. : Mixing and Transport in Coastal River Plumes, *Annual Review of Fluid Mechanics*, 47, 569–594, doi:10.1146/annurev-fluid-010313-141408, 2015.
- Huguenard, K. D. , Valle-Levinson, A. , Li, M. , Chant, R. J. , and Souza, A. J. : Linkage between lateral circulation and near-surface vertical mixing in a coastal plain estuary, *Journal of Geophysical Research: Oceans*, 120, 4048–4067, doi:10.1002/2014JC010679, 2015.
- Huijts, K. M. H. , Schuttelaars, H. M. , de Swart, H. E. , and Valle-Levinson, A. : Lateral entrainment of sediment in tidal estuaries: An idealized model study, *Journal of Geophysical Research: Oceans*, 111, doi:10.1029/2006JC003615, 2006.
- Huisman, Y. , Leummens, L. , Rodrigo, S. , Laan, S. , Wouter, K. , and van der Wijk, R. : Extra debiet over stuw Hagestein voor het tegengaan van verzilting van de Lek, Technical Report 11210363-001-ZKS-0001,, Deltares, Delft, 2024.
- Jakšić, L. : The recirculation near Maasvlakte 2 in the Rhine ROFI: Assessing the influence of a manmade headland and baroclinic processes, Master's thesis, Delft University of Technology, Faculty of Civil Engineering and Geosciences, URL <https://resolver.tudelft.nl/f19d486a-2010-4951-bd16-a5a3c3ed378c>, supervisors: J.D. Pietrzak, M.M. Busnelli, L.M. Keyzer, M. Verlaan, 2021.
- Jay, D. A. : Estuarine variability, in: *Contemporary Issues in Estuarine Physics*, edited by Valle-Levinson, A. , p. 62–99, Cambridge University Press, 2010.
- Jay, D. A. and Dungan Smith, J. : Circulation, density distribution and neap-spring transitions in the Columbia River Estuary, *Progress in Oceanography*, 25, 81–112, doi:10.1016/0079-6611(90)90004-L, 1990.
- Jay, D. A. and Musiak, J. D. : Internal Tidal Asymmetry in Channel

- Flows: Origins and Consequences, in: *Mixing in Estuaries and Coastal Seas*, Volume 50, chap. 13, pp. 219–258, American Geophysical Union, doi:<https://doi.org/10.1029/CE050p0211>, 1996.
- Jones, W. P. and Launder, B. E. : The prediction of laminarization with a two-equation model of turbulence, *International Journal of Heat and Mass Transfer*, 15, 301–314, doi:[https://doi.org/10.1016/0017-9310\(72\)90076-2](https://doi.org/10.1016/0017-9310(72)90076-2), 1972.
- Juarez, B. , Valle-Levinson, A. , and Li, C. : Estuarine salt-plug induced by freshwater pulses from the inner shelf, *Estuarine, Coastal and Shelf Science*, 232, 106–149, doi:<https://doi.org/10.1016/j.ecss.2019.106491>, 2020.
- Juarez, B. , Valle-Levinson, A. , and Canestrelli, A. : Mechanisms of Estuarine Salt-Plug Formation by an Along-Shelf Buoyant Current: A Numerical Model Approach, *Journal of Geophysical Research: Oceans*, 127, e2021JC017971, doi:[10.1029/2021JC017971](https://doi.org/10.1029/2021JC017971), 2022.
- Kay, A. L. , Bell, V. A. , Guillod, B. P. , Jones, R. G. , and Rudd, A. C. : National-scale analysis of low flow frequency: historical trends and potential future changes, *Climatic Change*, 147, 585–599, doi:[10.1007/s10584-018-2145-y](https://doi.org/10.1007/s10584-018-2145-y), 2018.
- Kelly-Gerrey, B. A. , Hydes, D. J. , Jégou, A. M. , Lazure, P. , Fernandez, L. J. , Puillat, I. , and Garcia-Soto, C. : Low salinity intrusions in the western English Channel, *Continental Shelf Research*, 26, 1241–1257, doi:[10.1016/j.csr.2006.03.007](https://doi.org/10.1016/j.csr.2006.03.007), publisher: Elsevier BV, 2006.
- Keyzer, L. M. : The Rhine River plume: Unravelling its dynamics and sea-level contributions, Ph.d. thesis, Delft University of Technology, Delft, The Netherlands, see Chapter 2, 2025.
- Kilcher, L. F. , Nash, J. D. , and Moum, J. N. : The role of turbulence stress divergence in decelerating a river plume, *Journal of Geophysical Research: Oceans*, 117, 2011JC007398, doi:[10.1029/2011JC007398](https://doi.org/10.1029/2011JC007398), 2012.
- Korotenko, K. A. , Osadchiv, A. A. , Zavialov, P. O. , Kao, R.-C. , and Ding, C.-F. : Effects of bottom topography on dynamics of river discharges in tidal regions: case study of twin plumes in Taiwan Strait, *Ocean Science*, 10, 863–879, doi:[10.5194/os-10-863-2014](https://doi.org/10.5194/os-10-863-2014), 2014.
- Kranenburg, C. , Pietrzak, J. D. , and Abraham, G. : Trapped internal waves over undular topography, *Journal of Fluid Mechanics*, 226, 205–217, doi:[10.1017/s0022112091002355](https://doi.org/10.1017/s0022112091002355), 1991.
- Kranenburg, W. , van der Kaaij, T. , Tiessen, M. , Friocourt, Y. , and Blaas, M. : Salt Intrusion In The Rhine Meuse Delta: Estuarine Circulation, Tidal Dispersion Or Surge Effect, in: *Proceedings of the 39th IAHR World Congress*, June, pp. 5601–5608, International Association for Hydro-Environment Engineering and Research (IAHR), Spain, doi:[10.3850/IAHR-39WC2521711920221058](https://doi.org/10.3850/IAHR-39WC2521711920221058), 2022.
- Kuijper, K. : Analyse van de zoutmetingen in november 2015 langs de Hollandse IJssel—Afleiding dispersiecoefficient, Technical Report 1230077–001, Deltares, Delft, 2016.
- Kullback, S. and Leibler, R. A. : On information and sufficiency, *The annals of*

- mathematical statistics, 22, 79–86, 1951.
- Large, W. G. , McWilliams, J. C. , and Doney, S. C. : Oceanic vertical mixing: A review and a model with a nonlocal boundary layer parameterization, *Reviews of Geophysics*, 32, 363–403, doi:10.1029/94RG01872, 1994.
- Lee, J. , Biemond, B. , de Swart, H. , and Dijkstra, H. A. : Increasing risks of extreme salt intrusion events across European estuaries in a warming climate, *Communications Earth & Environment*, 5, 60, doi:10.1038/s43247-024-01225-w, 2024.
- Lee, J. , Biemond, B. , van Keulen, D. , Huisman, Y. , van Westen, R. M. , de Swart, H. E. , Dijkstra, H. A. , and Kranenburg, W. M. : Global increases of salt intrusion in estuaries under future environmental conditions, *Nature Communications*, 16, 3444, doi:10.1038/s41467-025-58783-6, 2025.
- Lee, Y. J. and Lwiza, K. M. M. : Factors driving bottom salinity variability in the Chesapeake Bay, *Continental Shelf Research*, 28, 1352–1362, doi:10.1016/j.csr.2008.03.016, publisher: Elsevier BV, 2008.
- Lehfeldt, R. and Bloss, S. : Algebraic Turbulence Model for Stratified Tidal Flows, in: *Physical Processes in Estuaries*, edited by Dronkers, J. and van Leussen, W. , pp. 278–291, Springer Berlin Heidelberg, Berlin, Heidelberg, 1988.
- Lentz, S. : The Response of Buoyant Coastal Plumes to Upwelling-Favorable Winds\*, *Journal of Physical Oceanography*, 34, 2458–2469, doi:10.1175/JPO2647.1, 2004.
- Lerczak, J. A. , Geyer, W. R. , and Chant, R. J. : Mechanisms Driving the Time-Dependent Salt Flux in a Partially Stratified Estuary\*, *Journal of Physical Oceanography*, 36, 2296–2311, doi:10.1175/JPO2959.1, 2006.
- Lerczak, J. A. , Geyer, W. R. , and Ralston, D. K. : The Temporal Response of the Length of a Partially Stratified Estuary to Changes in River Flow and Tidal Amplitude, *Journal of Physical Oceanography*, 39, 915–933, doi:10.1175/2008JPO3933.1, 2009.
- Lewis, R. E. and Lewis, J. O. : The principal factors contributing to the flux of salt in a narrow, partially stratified estuary, *Estuarine, Coastal and Shelf Science*, 16, 599–626, doi:https://doi.org/10.1016/0272-7714(83)90074-4, 1983.
- Li, Y. and Li, M. : Effects of winds on stratification and circulation in a partially mixed estuary, *Journal of Geophysical Research: Oceans*, 116, doi:10.1029/2010JC006893, 2011.
- Liu, B. , Peng, S. , Liao, Y. , and Wang, H. : The characteristics and causes of increasingly severe saltwater intrusion in Pearl River Estuary, *Estuarine, Coastal and Shelf Science*, 220, 54–63, doi:https://doi.org/10.1016/j.ecss.2019.02.041, 2019.
- Liu, W.-C. , Hsu, M.-H. , and Kuo, A. Y. : Application of different turbulence closure model for stratified tidal flows and salinity in an estuarine system, *Mathematics and computers in simulation*, 59, 437–451, doi:10.1016/S0378-4754(01)00427-X, 2002.
- MacCready, P. : Estuarine Adjustment to Changes in River Flow and Tidal

- Mixing, *Journal of Physical Oceanography*, 29, 708–726, doi:10.1175/1520-0485(1999)029<0708:EATCIR>2.0.CO;2, 1999.
- MacCready, P. : Toward a unified theory of tidally-averaged estuarine salinity structure, *Estuaries*, 27, 561–570, doi:10.1007/BF02907644, 2004.
- MacCready, P. : Estuarine adjustment, *Journal of Physical Oceanography*, 37, 2133–2145, doi:10.1175/JPO3082.1, 2007.
- MacCready, P. and Geyer, W. R. : Advances in estuarine physics, *Annual Review of Marine Science*, 2, 35–58, doi:10.1146/annurev-marine-120308-081015, 2010.
- MacDonald, D. G. and Geyer, W. R. : Turbulent energy production and entrainment at a highly stratified estuarine front, *Journal of Geophysical Research: Oceans*, 109, 2003JC002094, doi:10.1029/2003JC002094, 2004.
- MacDonald, D. G. and Horner-Devine, A. R. : Temporal and spatial variability of vertical salt flux in a highly stratified estuary, *Journal of Geophysical Research*, 113, doi:10.1029/2007jc004620, 2008.
- MacDonald, D. G. , Goodman, L. , and Hetland, R. D. : Turbulent dissipation in a near-field river plume: A comparison of control volume and microstructure observations with a numerical model, *Journal of Geophysical Research: Oceans*, 112, 2006JC004075, doi:10.1029/2006JC004075, 2007.
- MacVean, L. J. and Stacey, M. T. : Estuarine Dispersion from Tidal Trapping: A New Analytical Framework, *Estuaries and Coasts*, 34, 45–59, doi:10.1007/s12237-010-9298-x, 2011.
- Manca, F. , Capelli, G. , Vigna, F. L. , Mazza, R. , and Pascarella, A. : Wind-induced salt-wedge intrusion in the Tiber river mouth (Rome-Central Italy), *Environmental Earth Sciences*, 72, 1083–1095, doi:10.1007/s12665-013-3024-5, 2014.
- Matte, P. , Secretan, Y. , and Morin, J. : Hydrodynamic Modeling of the St. Lawrence Fluvial Estuary. I: Model Setup, Calibration, and Validation, *Journal of Waterway, Port, Coastal, and Ocean Engineering*, 143, 04017010, doi:10.1061/(ASCE)WW.1943-5460.0000397, 2017.
- McCabe, R. M. , Hickey, B. M. , and MacCready, P. : Observational estimates of entrainment and vertical salt flux in the interior of a spreading river plume, *Journal of Geophysical Research: Oceans*, 113, 2007JC004361, doi:10.1029/2007JC004361, 2008.
- McCabe, R. M. , MacCready, P. , and Hickey, B. M. : Ebb-Tide Dynamics and Spreading of a Large River Plume\*, *Journal of Physical Oceanography*, 39, 2839–2856, doi:10.1175/2009JPO4061.1, 2009.
- McCarthy, R. K. : Residual currents in tidally dominated, well-mixed estuaries, *Tellus A: Dynamic Meteorology and Oceanography*, 45, 325–340, doi:10.3402/tellusa.v45i4.14896, 1993.
- McKeon, M. A. , Horner-Devine, A. R. , and Giddings, S. N. : Seasonal Changes in Structure and Dynamics in an Urbanized Salt Wedge Estuary, *Estuaries and Coasts*, 44, 589–607, doi:10.1007/s12237-020-00788-z/Published, 2021.

- Mellor, G. L. and Yamada, T. : Development of a turbulence closure model for geophysical fluid problems, *Reviews of Geophysics*, 20, 851–875, doi:10.1029/RG020i004p00851, 1982.
- Miles, J. W. : On the stability of heterogeneous shear flows, *Journal of Fluid Mechanics*, 10, 496, doi:10.1017/S0022112061000305, 1961.
- Mohammadian, A. , Morse, B. , and Robert, J.-L. : Calibration of a 3D hydrodynamic model for a hypertidal estuary with complex irregular bathymetry using adaptive parametrization of bottom roughness and eddy viscosity, *Estuarine, Coastal and Shelf Science*, 265, 107 655, doi:10.1016/j.ecss.2021.107655, 2022.
- Monismith, S. G. , Kimmerer, W. , Burau, J. R. , and Stacey, M. T. : Structure and Flow-Induced Variability of the Subtidal Salinity Field in Northern San Francisco Bay, *Journal of Physical Oceanography*, 32, 3003 – 3019, doi:10.1175/1520-0485(2002)032<3003:SAFIVO>2.0.CO;2, 2002.
- Munk, W. H. and Anderson, R. E. : Notes on the theory of the thermocline, *Journal of Marine Research*, 7, 276–295, 1948.
- Nash, J. D. , Kilcher, L. F. , and Moum, J. N. : Structure and composition of a strongly stratified, tidally pulsed river plume, *Journal of Geophysical Research: Oceans*, 114, doi:https://doi.org/10.1029/2008JC005036, 2009.
- Niessen, I. , Huismans, Y. , and Hoitink, A. J. F. : Ebb-Dominant Mixing Increases the Seaward Sediment Flux in a Stratified Estuary, *Journal of Geophysical Research: Oceans*, 129, e2024JC021 201, doi:10.1029/2024JC021201, 2024.
- Nunes Vaz, R. A. and Simpson, J. H. : Turbulence closure modeling of estuarine stratification, *Journal of Geophysical Research: Oceans*, 99, 16 143–16 160, doi:10.1029/94JC01200, 1994.
- Osborn, T. R. : Estimates of the Local Rate of Vertical Diffusion from Dissipation Measurements, *Journal of Physical Oceanography*, 10, 83–89, doi:10.1175/1520-0485(1980)010<0083:EOTLRO>2.0.CO;2, 1980.
- Pacanowski, R. C. and Philander, S. G. H. : Parameterization of Vertical Mixing in Numerical Models of Tropical Oceans, *Journal of Physical Oceanography*, 11, 1443 – 1451, doi:10.1175/1520-0485(1981)011<1443:POVMIN>2.0.CO;2, 1981.
- Park, K. and Kuo, A. Y. : A vertical two-dimensional model of estuarine hydrodynamics and water quality, *Special Reports in Applied Marine Science and Ocean Engineering*, 321, doi:10.21220/V50F2M, 1993.
- Perales-Valdivia, H. , Sanay-González, R. , and Valle-Levinson, A. : Effects of tides, wind and river discharge on the salt intrusion in a microtidal tropical estuary, *Regional Studies in Marine Science*, 24, 400–410, doi:https://doi.org/10.1016/j.rsma.2018.10.001, 2018.
- Peters, H. : Spatial and temporal variability of turbulent mixing in an estuary, *Journal of Marine Research*, 57, 805–845, 1999.
- Piccolroaz, S. , Fernández-Castro, B. , Toffolon, M. , and Dijkstra, H. A. : A multi-site, year-round turbulence microstructure atlas for the deep perialpine Lake Garda, *Scientific Data*, 8, 188, doi:10.1038/s41597-021-00965-0, 2021.

- Pietrzak, J. D. , Kranenburg, C. , and Abraham, G. : Resonant internal waves in fluid flow, *Nature*, 344, 844–847, doi:10.1038/344844a0, 1990.
- Pietrzak, J. D. , Kranenburg, C. , Abraham, G. , Kranenburg, B. , and van der Wekken, A. : Internal Wave Activity in Rotterdam Waterway, *Journal of Hydraulic Engineering*, 117, 738–757, doi:10.1061/(asce)0733-9429(1991)117:6(738), 1991.
- Pietrzak, J. D. , de Boer, G. J. , and Eleveld, M. A. : Mechanisms controlling the intra-annual mesoscale variability of SST and SPM in the southern North Sea, *Continental Shelf Research*, 31, 594–610, doi:10.1016/j.csr.2010.12.014, publisher: Elsevier BV, 2011.
- Poggioli, A. R. and Horner-Devine, A. R. : The sensitivity of salt wedge estuaries to channel geometry, *Journal of Physical Oceanography*, 45, 3169–3183, doi:10.1175/JPO-D-14-0218.1, 2015.
- Ralston, D. K. , Geyer, W. R. , and Lerczak, J. A. : Subtidal Salinity and Velocity in the Hudson River Estuary: Observations and Modeling, *Journal of Physical Oceanography*, 38, 753–770, doi:10.1175/2007JPO3808.1, 2008.
- Ralston, D. K. , Geyer, W. R. , and Lerczak, J. A. : Structure, variability, and salt flux in a strongly forced salt wedge estuary, *Journal of Geophysical Research: Oceans*, 115, doi:10.1029/2009JC005806, 2010.
- Ralston, D. K. , Cowles, G. W. , Geyer, W. R. , and Holleman, R. C. : Turbulent and numerical mixing in a salt wedge estuary: Dependence on grid resolution, bottom roughness, and turbulence closure, *Journal of Geophysical Research: Oceans*, 122, 692–712, doi:10.1002/2016JC011738, 2017.
- Ralston, D. K. , Geyer, W. R. , Wackerman, C. C. , Dzwonkowski, B. , Honegger, D. A. , and Haller, M. C. : Interacting Influences of Diurnal Tides, Winds, and River Discharge on a Large Coastal Plume, *Journal of Geophysical Research: Oceans*, 129, e2024JC021288, doi:https://doi.org/10.1029/2024JC021288, e2024JC021288 2024JC021288, 2024.
- Rijkswaterstaat: Hollandsche IJssel, URL <https://www.rijkswaterstaat.nl/water/vaarwegenoverzicht/hollandsche-ijssel>, 2024a.
- Rijkswaterstaat: Lek, URL <https://www.rijkswaterstaat.nl/water/vaarwegenoverzicht/lek>, 2024b.
- Rijkswaterstaat: Nieuwe Waterweg, URL <https://www.rijkswaterstaat.nl/water/vaarwegenoverzicht/nieuwe-waterweg>, 2025.
- Rijnsburger, S. : On the dynamics of tidal plume fronts in the Rhine Region of Freshwater Influence, Ph.d. thesis, Delft University of Technology, Delft, The Netherlands, see Chapter 1, 2021.
- Rijnsburger, S. , Flores, R. P. , Pietrzak, J. D. , Horner-Devine, A. R. , and Souza, A. J. : The Influence of Tide and Wind on the Propagation of Fronts in a Shallow River Plume, *Journal of Geophysical Research: Oceans*, 123, 5426–5442, doi:10.1029/2017jc013422, 2018.
- Rijnsburger, S. , Flores, R. P. , Pietrzak, J. D. , Horner-Devine, A. R. , Souza, A. J. , and Zijl, F. : The Evolution of Plume Fronts in the Rhine Re-

- gion of Freshwater Influence, *Journal of Geophysical Research: Oceans*, 126, doi:10.1029/2019jc015927, 2021a.
- Rijnsburger, S. , Flores, R. P. , Pietrzak, J. D. , Lamb, K. G. , Jones, N. L. , Horner-Devine, A. R. , and Souza, A. J. : Observations of Multiple Internal Wave Packets in a Tidal River Plume, *Journal of Geophysical Research: Oceans*, 126, doi:10.1029/2020jc016575, 2021b.
- Rossby, C.-G. and Montgomery, R. B. : The layer of frictional influence in wind and ocean currents, *Papers in Physical Oceanography and Meteorology*, doi:10.1575/1912/1157, 1935.
- Salcedo-Castro, J. , Olita, A. , Saavedra, F. , Saldías, G. S. , Cruz-Gómez, R. C. , and De la Torre Martínez, C. D. : Modeling the interannual variability in Maipo and Rapel river plumes off central Chile, *Ocean Science*, 19, 1687–1703, doi:10.5194/os-19-1687-2023, 2023.
- Sanchez, C. , Williams, K. D. , and Collins, M. : Improved stochastic physics schemes for global weather and climate models, *Quarterly Journal of the Royal Meteorological Society*, 142, 147–159, doi:10.1002/qj.2640, 2016.
- Schijf, B. and Schönfeld, C. : *Theoretical Considerations on the Motion of Salt and Freshwater*, 1953.
- Schloen, J. , Stanev, E. V. , and Grashorn, S. : Wave-current interactions in the southern North Sea: The impact on salinity, *Ocean Modelling*, 111, 19–37, doi:10.1016/j.ocemod.2017.01.003, 2017.
- Scully, M. E. , Friedrichs, C. , and Brubaker, J. : Control of Estuarine Stratification and Mixing by Wind-induced Straining of the Estuarine Density Field, *Estuarine Research Federation Estuaries*, 28, 321–326, 2005.
- Scully, M. E. , Geyer, W. R. , and Trowbridge, J. H. : The Influence of Stratification and Nonlocal Turbulent Production on Estuarine Turbulence: An Assessment of Turbulence Closure with Field Observations, *Journal of Physical Oceanography*, 41, 166–185, doi:10.1175/2010JPO4470.1, 2011.
- Sherin, V. R. , Durand, F. , Papa, F. , Islam, A. S. , Gopalakrishna, V. V. , Khaki, M. , and Suneel, V. : Recent salinity intrusion in the Bengal delta: Observations and possible causes, *Continental Shelf Research*, 202, 104–142, doi:https://doi.org/10.1016/j.csr.2020.104142, 2020.
- Simpson, J. H. : Physical processes in the ROFI regime, *Journal of Marine Systems*, 12, 3–15, doi:https://doi.org/10.1016/S0924-7963(96)00085-1, 1997.
- Simpson, J. H. and Bowers, D. : Models of stratification and frontal movement in shelf seas, *Deep Sea Research Part A. Oceanographic Research Papers*, 28, 727–738, doi:10.1016/0198-0149(81)90132-1, 1981.
- Simpson, J. H. and Souza, A. J. : Semidiurnal switching of stratification in the region of freshwater influence of the Rhine, *Journal of Geophysical Research: Oceans*, 100, 7037–7044, doi:10.1029/95JC00067, 1995.
- Simpson, J. H. , Brown, J. , Matthews, J. , and Allen, G. : Tidal Straining, Density Currents, and Stirring in the Control of Estuarine Stratification, *Estuaries*, 13, 125, doi:10.2307/1351581, 1990.

- Simpson, J. H. , Williams, E. , Brasseur, L. H. , and Brubaker, J. M. : The impact of tidal straining on the cycle of turbulence in a partially stratified estuary, *Continental Shelf Research*, 25, 51–64, doi:10.1016/j.csr.2004.08.003, 2005.
- Souza, A. J. and Simpson, J. H. : The modification of tidal ellipses by stratification in the Rhine ROFI, *Continental Shelf Research*, 16, 997–1007, doi:https://doi.org/10.1016/0278-4343(95)00042-9, 1996.
- Spicer, P. and Huguenard, K. : Observations of Near-Surface Mixing Behind a Headland, *Journal of Marine Science and Engineering*, 8, doi:10.3390/jmse8020068, 2020.
- Stacey, M. T. , Burau, J. R. , and Monismith, S. G. : Creation of residual flows in a partially stratified estuary, *Journal of Geophysical Research: Oceans*, 106, 17 013–17 037, doi:https://doi.org/10.1029/2000JC000576, 2001.
- Tedford, E. W. , Carpenter, J. R. , Pawlowicz, R. , Pieters, R. , and Lawrence, G. A. : Observation and analysis of shear instability in the Fraser River estuary, *Journal of Geophysical Research: Oceans*, 114, doi:https://doi.org/10.1029/2009JC005313, 2009.
- Tjernström, M. : Turbulence Length Scales in Stably Stratified Free Shear Flow Analyzed from Slant Aircraft Profiles, *Journal of Applied Meteorology*, 32, 948–963, doi:10.1175/1520-0450(1993)032<0948:TLSISS>2.0.CO;2, 1993.
- Umlauf, L. and Burchard, H. : A generic length-scale equation for geophysical turbulence models, *Journal of Marine Research*, 61, 235–265, doi:10.1357/002224003322005087, 2003.
- van der Molen, J. and Pätsch, J. : An overview of Atlantic forcing of the North Sea with focus on oceanography and biogeochemistry, *Journal of Sea Research*, 189, 102 281, doi:10.1016/j.seares.2022.102281, publisher: Elsevier BV, 2022.
- van der Weijden, C. and Middelburg, J. : Hydrogeochemistry of the River Rhine: Long term and seasonal variability, elemental budgets, base levels and pollution, *Water Research*, 23, 1247–1266, doi:https://doi.org/10.1016/0043-1354(89)90187-5, 1989.
- Visser, A. W. , Souza, A. S. , Hessner, K. , and Simpson, J. H. : The effect of stratification on tidal current profiles in a region of freshwater influence, *Oceanol Acta*, 17, 369–381, doi:10.2307/1351581, 1994.
- Warner, J. , Schoellhamer, D. , Burau, J. , and Schladow, G. : Effects of tidal current phase at the junction of two straits, *Continental Shelf Research*, 22, 1629–1642, doi:https://doi.org/10.1016/S0278-4343(02)00026-2, proceedings from the Tenth Biennial Conference on the Physics of Estuaries and Coastal Seas, 2002.
- Wegman, T. M. , Pietrzak, J. D. , Horner-Devine, A. R. , Dijkstra, H. A. , and Ralston, D. K. : Observations of Estuarine Salt Intrusion Dynamics During a Prolonged Drought Event in the Rhine-Meuse Delta, *Journal of Geophysical Research: Oceans*, 130, e2024JC021 655, doi:https://doi.org/10.1029/2024JC021655, e2024JC021655 2024JC021655, 2025.

- Weisse, R. , von Storch, H. , Niemeier, H. D. , and Knaack, H. : Changing North Sea storm surge climate: An increasing hazard?, *Ocean & Coastal Management*, 68, 58–68, doi:<https://doi.org/10.1016/j.ocecoaman.2011.09.005>, special Issue on the Wadden Sea Region, 2012.
- Whitney, M. M. and Garvine, R. W. : Wind influence on a coastal buoyant outflow, *Journal of Geophysical Research: Oceans*, 110, doi:<https://doi.org/10.1029/2003JC002261>, 2005.
- Wilson, B. W. : Note on surface wind stress over water at low and high wind speeds, *Journal of Geophysical Research*, 65, 3377–3382, doi:[10.1029/JZ065i010p03377](https://doi.org/10.1029/JZ065i010p03377), 1960.
- Wong, K.-C. and Garvine, R. W. : Observations of wind-induced, subtidal variability in the Delaware estuary, *Journal of Geophysical Research: Oceans*, 89, 10 589–10 597, doi:<https://doi.org/10.1029/JC089iC06p10589>, 1984.
- Wong, K.-C. and Valle-Levinson, A. : On the relative importance of the remote and local wind effects on the subtidal exchange at the entrance to the Chesapeake Bay, *Journal of Marine Research*, 60, 477–498, doi:[10.1357/002224002762231188](https://doi.org/10.1357/002224002762231188), 2002.
- Wunsch, C. and Stammer, D. : Atmospheric loading and the oceanic “inverted barometer” effect, *Reviews of Geophysics*, 35, 79–107, doi:<https://doi.org/10.1029/96RG03037>, 1997.
- Zhang, X. , Hetland, R. D. , Marta-Almeida, M. , and DiMarco, S. F. : A numerical investigation of the Mississippi and Atchafalaya freshwater transport, filling and flushing times on the Texas-Louisiana Shelf, *Journal of Geophysical Research: Oceans*, 117, 2012JC008 108, doi:[10.1029/2012JC008108](https://doi.org/10.1029/2012JC008108), 2012.
- Zhu, C. , van Maren, D. S. , Guo, L. , Lin, J. , He, Q. , and Wang, Z. B. : Effects of Sediment-Induced Density Gradients on the Estuarine Turbidity Maximum in the Yangtze Estuary, *Journal of Geophysical Research: Oceans*, 126, e2020JC016 927, doi:[10.1029/2020JC016927](https://doi.org/10.1029/2020JC016927), 2021.
- Zhu, J. , Cheng, X. , Li, L. , Wu, H. , Gu, J. , and Lyu, H. : Dynamic mechanism of an extremely severe saltwater intrusion in the Changjiang estuary in February 2014, *Hydrology and Earth System Sciences*, 24, 5043–5056, doi:[10.5194/hess-24-5043-2020](https://doi.org/10.5194/hess-24-5043-2020), 2020.

# Acknowledgements

This PhD journey has brought me many great experiences, allowed me to meet inspiring people, and has helped me grow both personally and professionally. I would like to thank everyone who contributed along the way to my PhD, either directly to the research or to the journey itself. Here, I would like to thank some people in particular.

First of all, I would like to thank my supervisory team for giving me the opportunity to pursue this PhD. Especially Julie, for your contagious enthusiasm for river plumes and internal waves, and for the endless stream of ideas. I also very much appreciate that you introduced me to a great international network of oceanographers. I am thankful to Alex, for contributing creative ideas to the analysis and for teaching me how to clearly define research questions. Furthermore, a highlight of my PhD was staying in Seattle and getting to know the Civil Engineering and Oceanography groups at UW. Thank you for the warm welcome, both in your street and at the University of Washington. Thanks to Henk for joining the MicroCTD surveys, and for spending thirteen hours together on a ship. You taught me a lot through your pragmatic approach and critical feedback, and for giving me the confidence that I am becoming an independent researcher.

Besides my supervisors, this booklet would not have been possible, without the co-authors that I collaborated with. First of all, I would like to thank Dave for providing your expertise in designing a challenging field campaign. I highly appreciate your good ideas for the analysis, as well as the way you challenged me by answering my questions with questions instead of answers. Wouter, thank you for your enthusiasm for oceanography and field work, and for providing constructive feedback. Furthermore, I very much enjoyed working with Bouke; thanks for taking the challenge of fishing with the MicroCTD in the Rotterdam Waterway multiple times. I highly appreciate your contribution to the paper related to these campaigns, it was always great to have in-depth discussions on the content, as well as (very loud) laughs together! Thanks Sebastiano, for trusting us with your MicroCTD in the very dynamic and shallow Rotterdam Waterway (in contrast to Lake Garda), and for your help and discussions on the turbulence data processing.

Furthermore, I would like to thank the members of the independent committee, Hans Burchard, Ad Reniers, Arnaldo Valle-Levinson, Henk Schuttelaars, and Bram van Prooijen, for reading and assessing my thesis, and for providing constructive feedback.

I very much enjoyed doing my PhD research within the SALTISolutions consortium. I am very grateful for the extensive network of salt intrusion enthusiasts, both from the user side and the research side. It was a lot of fun to have many PhDs and postdocs simultaneously working on the same topic from different per-

spectives. Specific thanks go out to users with whom I had fruitful discussions and who helped with providing instruments and data, and collecting or interpreting the field data: Lambert, Marlous, Meave, Meinte, Nathalie, Sicco, and Ymkje.

I also want to thank everyone who contributed to the field work. In particular, the team from the Hydraulic Engineering lab, Pieter, Arie, Arno, and Chantal. From the user side, I would like to thank Rijkswaterstaat for substantial in-kind support during the fieldwork. Jan-Willem, Arjen, thank you for making the field work a success, your enthusiasm and experience made it a very successful campaign. The 13-hour cruises with the Port of Rotterdam were both successful and enjoyable thanks to the great crew on board. Lastly, I would like to thank all TU Delft and SALTI colleagues who helped to prepare instruments, joined on any of the many ship cruises, or helped to clean the instruments.

The PhD journey was very enjoyable thanks to the wide range of colleagues I met along the way and with whom I shared both the highs and the lows. Thanks to all EFM/HE colleagues for the laughs, pétanque/Molky Fridays, dinners, runs, and bike rides, especially my PhD/PD colleagues from the second floor: Anna, Avelon, Bouke, Cem, Dennis, Filipe, Floris, Hannah, Inge, Jessamy, Lennart, Lucas, Marlein, Patrick, Paul, and Silke. I also want to thank the TUD SALTISolutions PhDs for our weekly coffee moments, which I always looked forward to. I am especially grateful to Marlein for our collaborations throughout the PhD, as sharing both the research journey and many memorable conference experiences made the process much more fun. I also had a wonderful time at UW, thanks to Walter, Lily, Dakota, Aurora, Erin, and all other members of EFM who made me feel at home.

I am also very thankful to my paranymphs and great friends, Fransje and Vesna, with whom I shared the PhD journey. Thanks for the support in finalising my thesis and helping with the defence preparations. I would also like to thank all my other friends who were always there to listen to my complaints or simply take me out for a run or a bike ride. I would also like to thank my family for their unconditional support and for believing in me. Tjerk, thanks for always being on my side, always encouraging, patient, and endlessly positive.

# A

## Supplementary Figures of Chapter 2

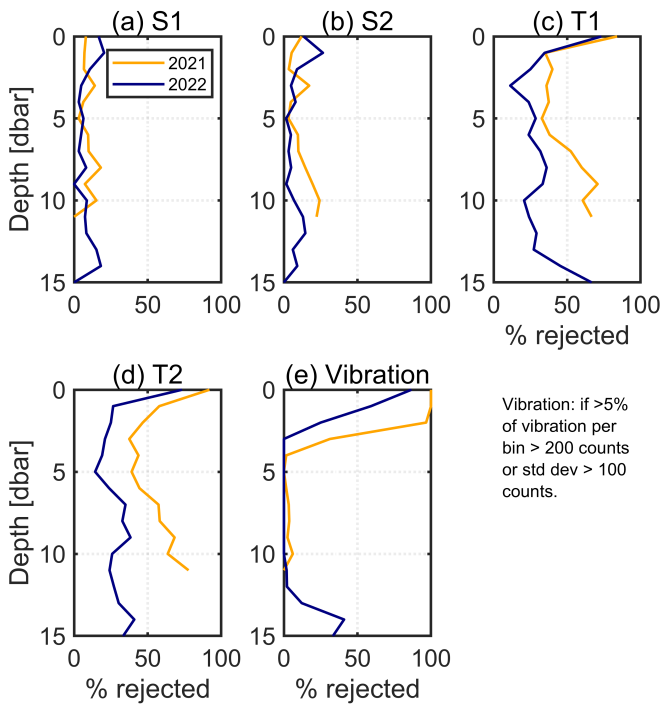


**Figure A.1:** Percentage of the rejected  $\varepsilon$  estimates, based on (a)-(b) shear sensors, (c)-(d) temperature sensors, (e) vibration.

It is *a posteriori* confirmed that the agreement between observations and parametrisations of  $K_v$  is not sensitive to the value of this threshold (variation in the skill score (defined below) is smaller than 5% when applying the threshold or not).

A

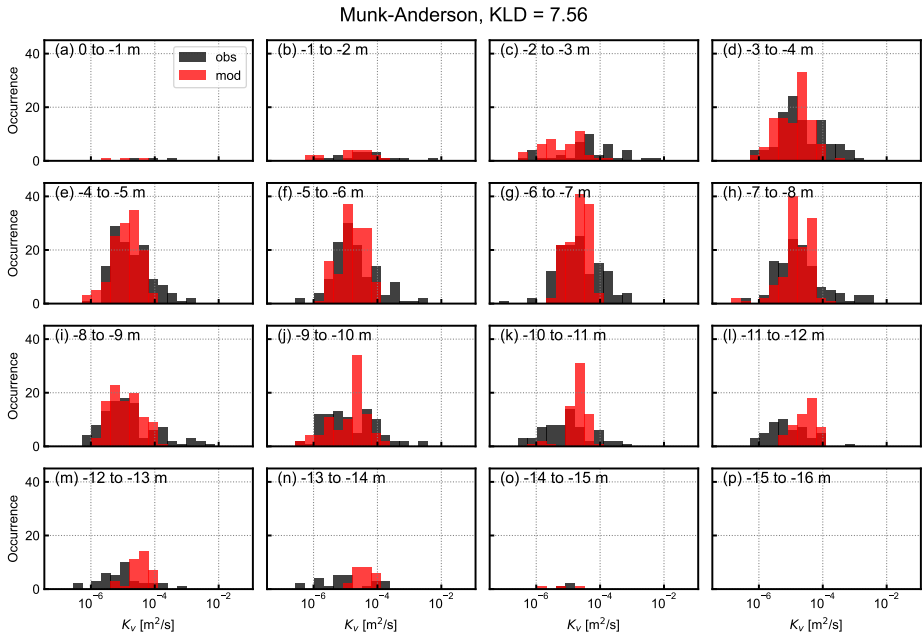


**Figure A.2:** (a) Histogram of the observed  $K_v$  of all casts binned between 0 and 1 m depth (in black), and the corresponding values from the Munk and Anderson (1948) parametrisation (in red). (b)-(p): As (a), but for different vertical ranges.

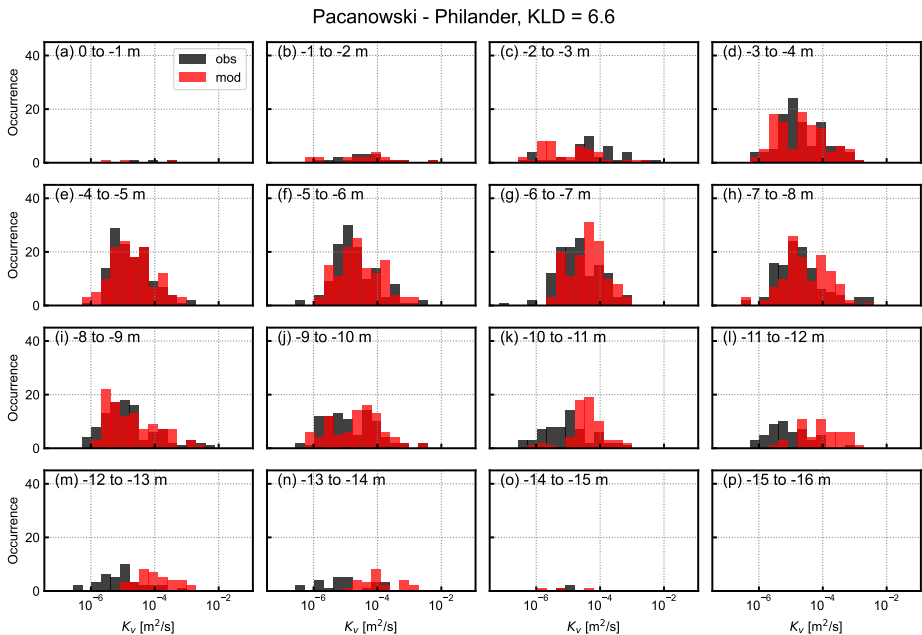


**Figure A.3:** As Figure A.2, but for the Pacanowski and Philander (1981) parametrisation.

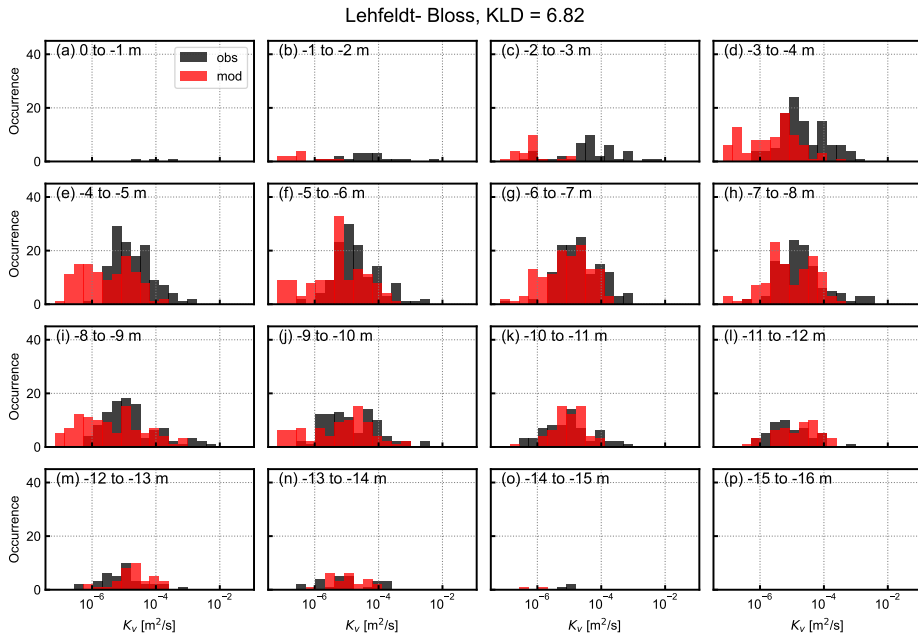


**Figure A.4:** As Figure A.2, but for the Lehfeldt and Bloss (1988) parametrization.

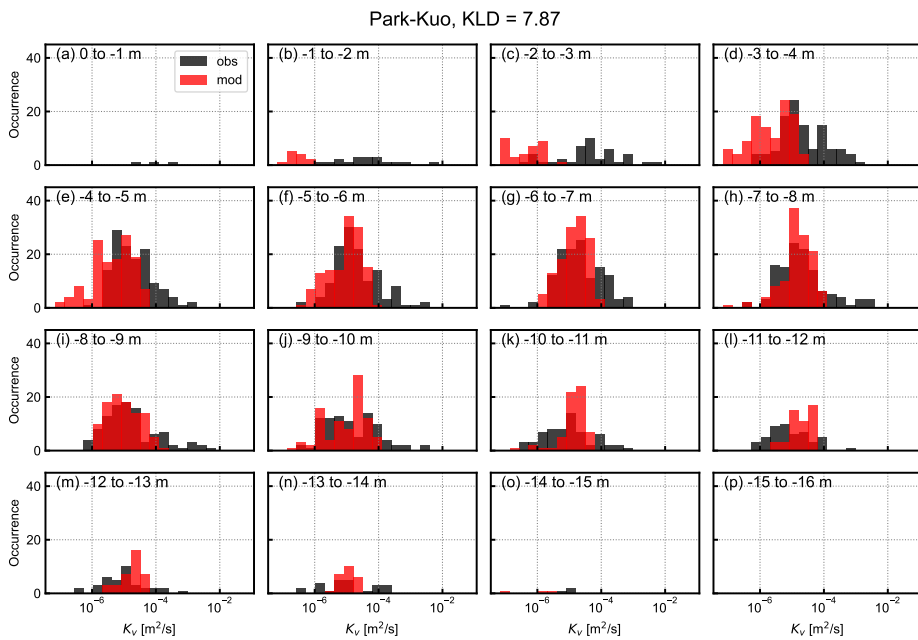


**Figure A.5:** As Figure A.2, but for the Park and Kuo (1993) parametrization.

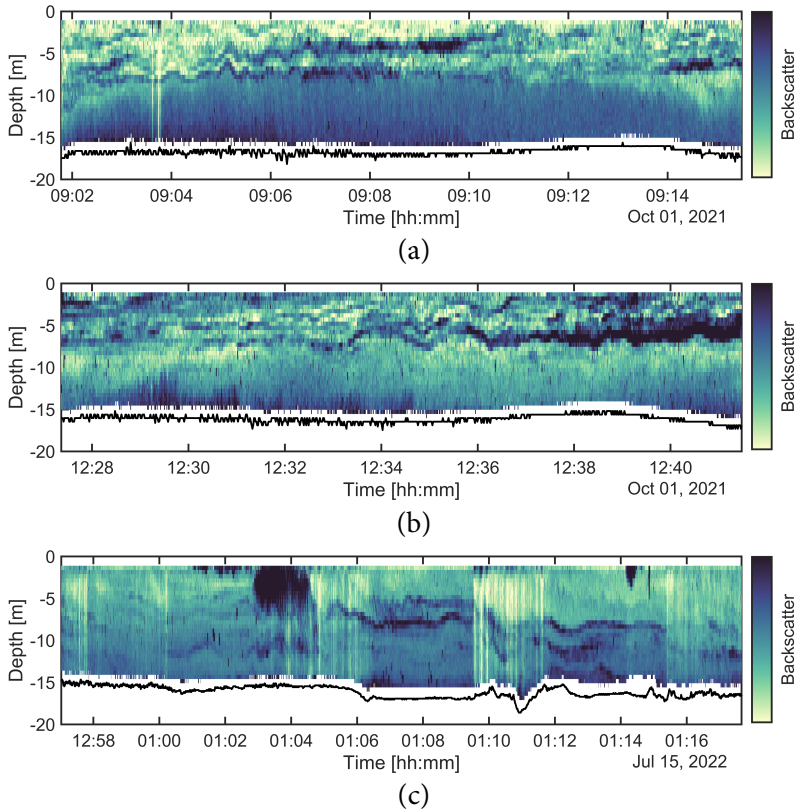


**Figure A.6:** ADCP backscatter at instances where internal waves were observed. (a) On 1<sup>st</sup> October 2021, during flood tide, (b) on 1<sup>st</sup> October 2021, on high water slack, (c) on 15<sup>th</sup> July 2022, during ebb tide.

# B

## Supplementary Figures of Chapter 3

This Appendix includes complementary figures to Chapter 3 "Observations of estuarine salt intrusion dynamics during a prolonged drought event in the Rhine-Meuse Delta". Without correction for the river discharge, there is no correlation between the coastal set-up at Hoek van Holland and salt intrusion length. When the offset to the discharge fit is taken on the y-axis, the  $R^2$  is increased to 0.16 (Figure B.1). Figure B.2 shows the stratification pattern together with the spring-neap tidal cycle. We observed an increased stratification just after neaps and a decreased stratification just after springs. Figure B.3 shows that there is no correlation between the discharge through the branches  $Q_{branch}$  and salt intrusion length  $L_{0.3}$ .

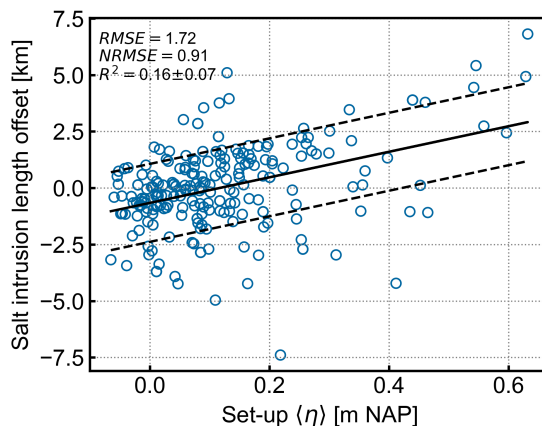


**Figure B.1:** Coastal set-up dependence of salt intrusion length, showing the tidally averaged set-up at Hoek van Holland versus salt intrusion length offset, corrected for river discharge. The solid black lines indicate the least-squares linear fit and the dashed lines indicate this fit  $\pm RMSE$ .

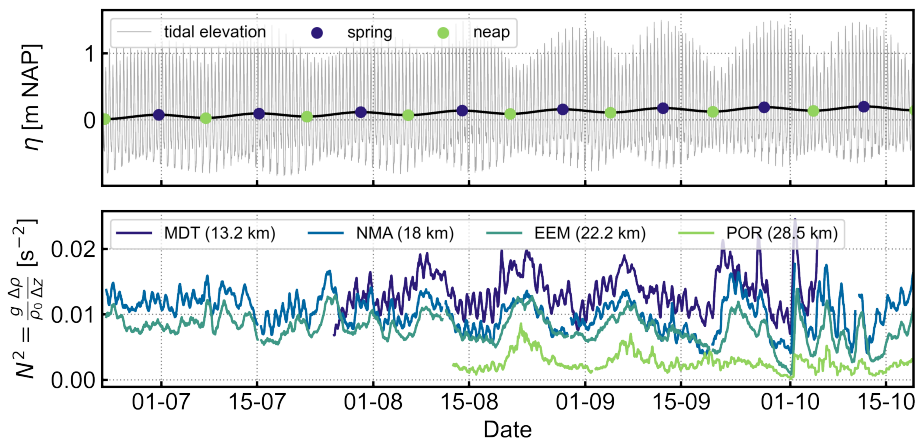
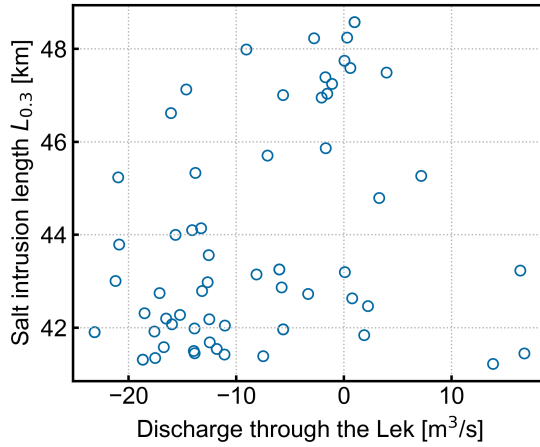
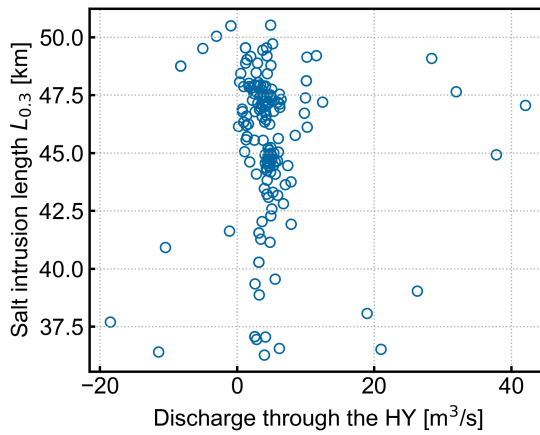


**Figure B.2:** Time series indicating the relation between stratification and the spring-neap cycle, shown by a) the buoyancy frequency  $N^2 = \frac{g \Delta \rho}{\rho_0 \Delta z}$  for different locations in the estuary and b) tidal elevation  $\eta$  at Hoek van Holland, indicating the spring-neap cycle.



(a)



(b)

**Figure B.3:** Salt intrusion length  $L_{0.3}$  versus discharge through the branch a) in the Lek and b) in the Hollandsche IJssel (HY).



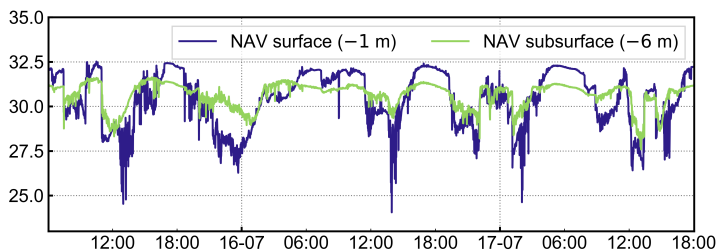
# C

## Supplementary Figures of Chapter 4

### C.1 Salinity correction NAV surface sensor

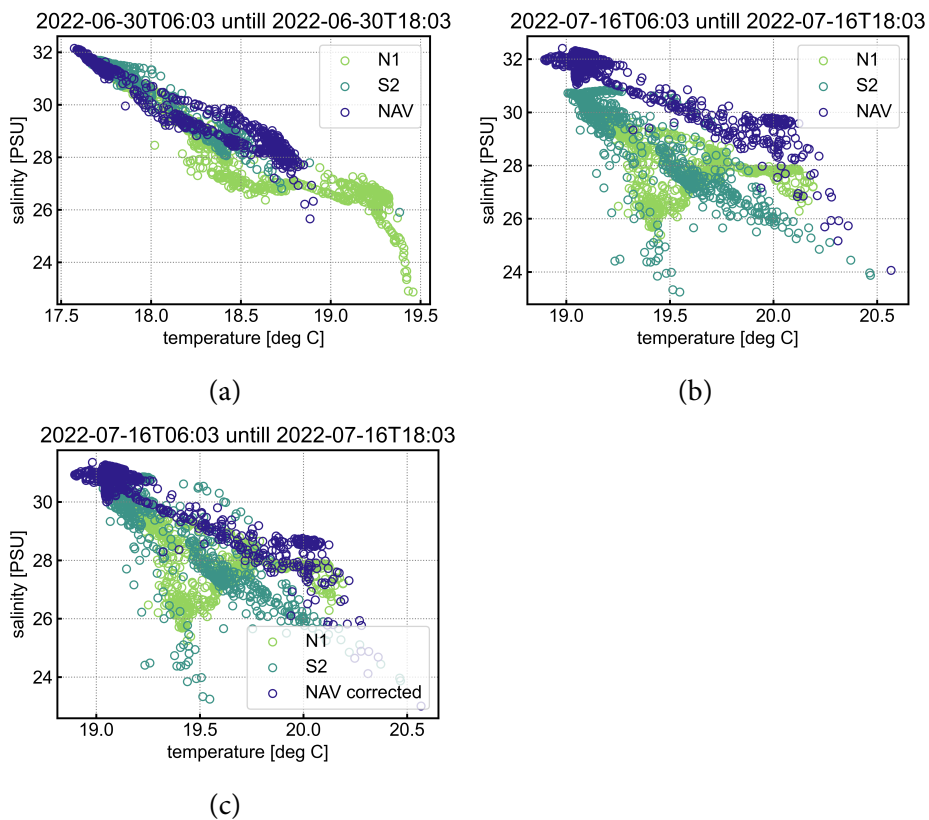
The measurement period after 14 July 2022, the surface sensor at NAV had an offset towards higher salinities. The surface (mean water depth of 1 m) salinity often exceeded the subsurface (mean water depth of 6 m) salinity during this period (Fig. C.1). To correct this data, we compared the maximum salinity within a tidal cycle to the other mooring locations with a surface sensor (N1 and S2). This gave a mean offset of 1.05 PSU.

Figure C.2a gives a T-S diagram before the correction and Figure C.2b after the correction. Figure C.2c gives a T-S diagram before the sensor had an offset.



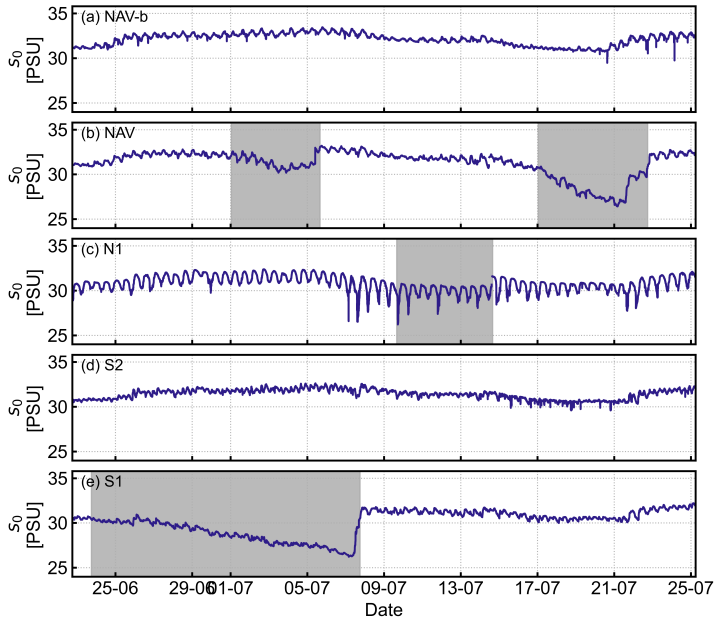
**Figure C.1:** Surface and subsurface salinity at NAV, showing that the surface salinity occasionally exceeds the subsurface salinity.

C



**Figure C.2:** Temperature-salinity plots of surface sensors at N1, S2, and NAV. (a) before the correction (b) after the correction, and (c) before the sensor had an offset.

## C.2 Near-field bottom salinity comparison between stations



(d)

**Figure C.3:** Near-field bottom salinity  $s_0$  comparison between sensors (a) NAV-b, (b) NAV, (c) N1, (d) S2, (e) S1. Grey areas indicate periods of biofouling or sediment-clogged salinity sensors.

C

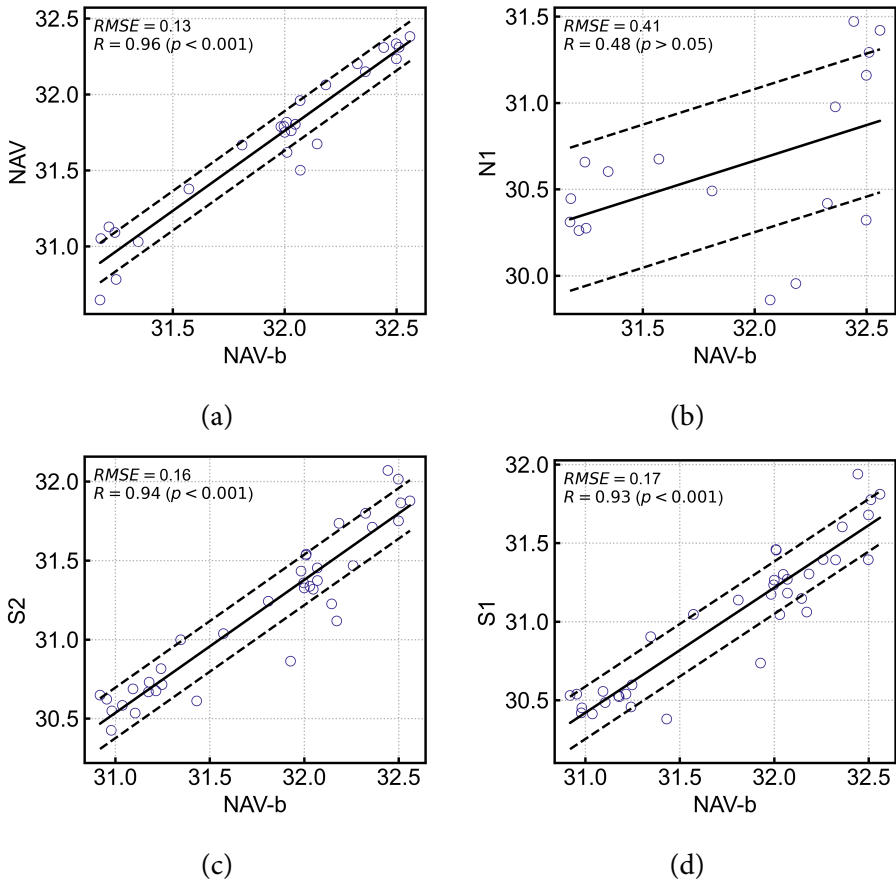


**Figure C.4:** Near-field bottom salinity comparison between sensors, for the valid periods between 22 June and 25 July, as indicated in Fig C1. (a) NAV vs NAV-b, (b) NAV vs N1, (c) NAV vs S2, (d) NAV vs S1

### C.3 Additional Figures: Wind response

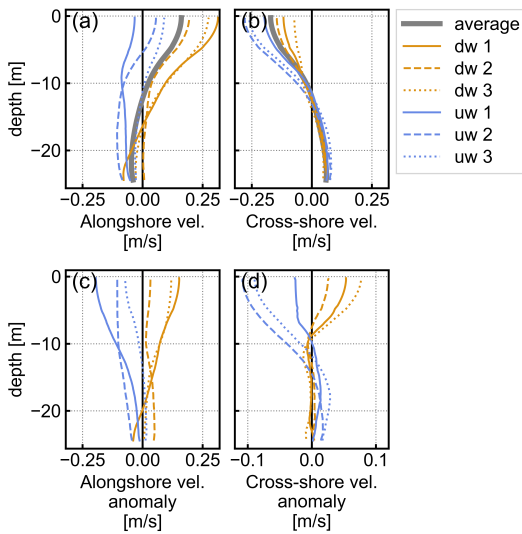


**Figure C.5:** Velocity profiles at NAV of selected periods with upwelling and downwelling-favourable winds. Including tidally filtered (a) alongshore velocities and (b) cross-shore velocities. (c-d) similar to (a-b), but then the anomalies (difference between temporal mean).

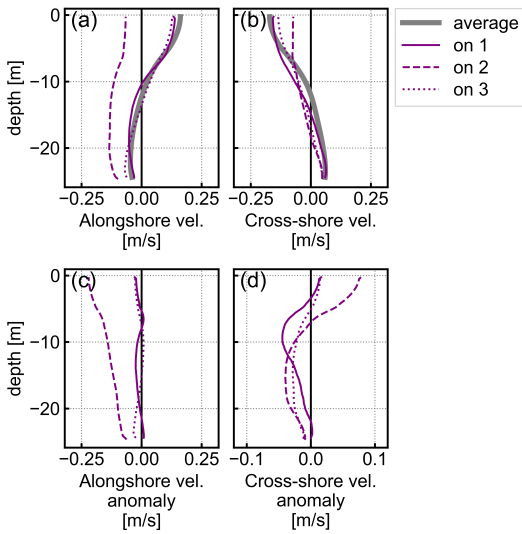


**Figure C.6:** Velocity profiles at NAV of selected periods with onshore winds. Including tidally filtered (a) alongshore velocities and (b) cross-shore velocities. (c-d) similar to (a-b), but then the anomalies (difference between temporal mean).

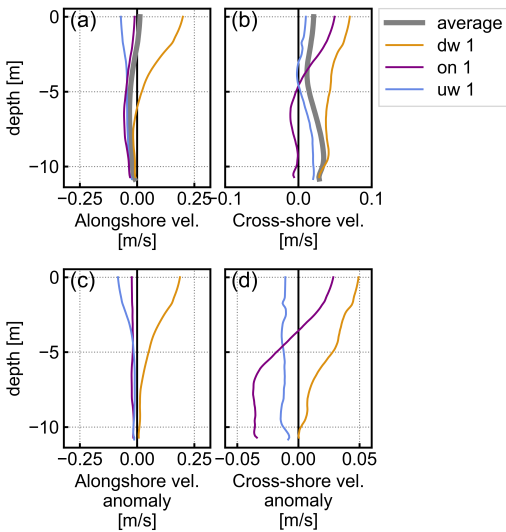


**Figure C.7:** Velocity profiles at N2 of selected periods with upwelling-favourable, downwelling-favourable, and onshore winds. Including tidally filtered (a) alongshore velocities and (b) cross-shore velocities. (c-d) similar to (a-b), but then the anomalies (difference between temporal mean).

## C.4 Additional Figures: Relation between river discharge and estuarine salinity

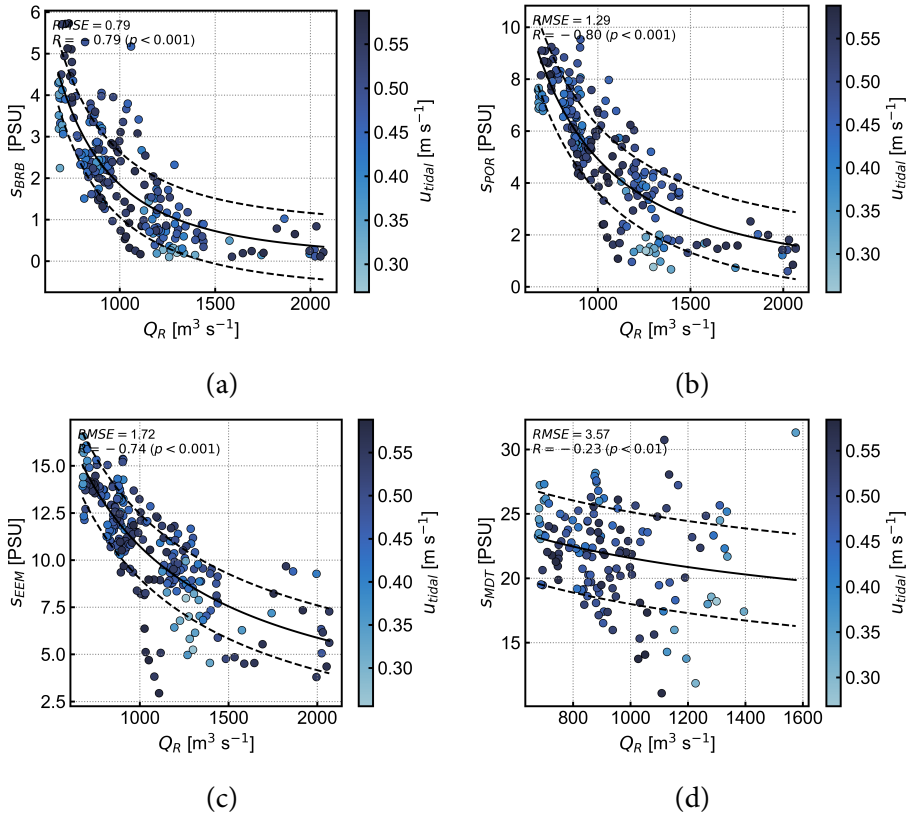


**Figure C.8:** Relation between Rhine River discharge  $Q_R$  and bottom salinity in the estuary at (a) BRB, 40 km inland, (b) POR, 33 km inland, (c) EEM, 27 km inland, and (d) MDT, 18 km inland.



# List of symbols

## Roman letters

$A$	cross-sectional area of the estuary [ $\text{m}^2$ ]
$A_s$	surface area of the estuary [ $\text{m}^2$ ]
$B$	channel width [m]
$C_d$	dimensionless drag coefficient [-]
$c_n$	calibration constants $n = 1 - 7$ [-]
$g$	gravitational acceleration [ $\text{m s}^{-2}$ ]
$H$	water depth [m]
$H_0$	tidally averaged water depth [m]
$h$	thickness of the freshwater layer [m]
$K_h$	alongchannel/horizontal diffusivity [ $\text{m}^2 \text{s}^{-1}$ ]
$K_v$	vertical turbulent diffusivity [ $\text{m}^2 \text{s}^{-1}$ ]
$k_s$	Nikuradse roughness height [m]
$L_s$	salt intrusion length, based on $s$ PSU isohaline [km]
$N$	buoyancy frequency [ $\text{s}^{-1}$ ]
$P$	atmospheric pressure [hPa]
$P_0$	reference atmospheric pressure [hPa]
$p$	$p$ -value; significance level result from hypothesis testing [-]
$Q_{Lek}$	Lek River discharge [ $\text{m}^3 \text{s}^{-1}$ ]
$Q_{in}$	up-estuary volume flux [ $\text{m}^3 \text{s}^{-1}$ ]
$Q_R$	river discharge [ $\text{m}^3 \text{s}^{-1}$ ]
$Q_{Rhine}$	Rhine River discharge [ $\text{m}^3 \text{s}^{-1}$ ]
$R$	Pearson correlation coefficient [-]
$Ri$	gradient Richardson number [-]
$Ri_E$	estuarine Richardson number [-]
$S$	vertical velocity shear [ $\text{s}^{-1}$ ]
$s$	salinity [PSU]
$s_0$	near-field bottom salinity [PSU]
$s_{plume}$	plume salinity [PSU]
$t$	time [s]
$U$	velocity magnitude [ $\text{m s}^{-1}$ ]
$U_{10}$	wind speed at 10 m elevation [ $\text{m s}^{-1}$ ]
$u$	velocity (in x-direction) [ $\text{m s}^{-1}$ ]
$u_0$	subtidal depth averaged flow [ $\text{m s}^{-1}$ ]
$u_1$	subtidal shear flow [ $\text{m s}^{-1}$ ]
$u_{plume,cs}$	cross-shore plume velocity [ $\text{m s}^{-1}$ ]
$u_i$	eastward velocity component [ $\text{m s}^{-1}$ ]
$u_j$	northward velocity component [ $\text{m s}^{-1}$ ]

$u_R$	freshwater flow velocity [ $\text{m s}^{-1}$ ]
$u_{tidal}$	tidal velocity [ $\text{m s}^{-1}$ ]
$v$	velocity in y-direction [ $\text{m s}^{-1}$ ]
$W$	Wedderburn number [-]
$x$	x-coordinate [m]
$y$	y-coordinate [m]
$z$	z-coordinate [m]

### Greek letters

$\Gamma$	mixing efficiency [-]
$\varepsilon$	turbulent kinetic energy dissipation rate [ $\text{m}^2 \text{s}^{-3}$ ]
$\eta$	water surface elevation [m]
$\langle \eta \rangle$	coastal set-up [m]
$\nu$	kinematic viscosity of water [ $\text{kg m}^{-1} \text{s}^{-1}$ ]
$\rho_a$	air density [ $\text{kg m}^{-3}$ ]
$\rho_s$	seawater density [ $\text{kg m}^{-3}$ ]
$\rho_w$	water density [ $\text{kg m}^{-3}$ ]
$\tau_w$	wind shear stress [ $\text{N m}^{-2}$ ]
$\Psi_s$	Nasmyth spectrum [ $\text{s}^{-2} \text{cpm}^{-1}$ ]

### Abbreviations

ADCP	Acoustic Doppler Current Profiler
CTD	Conductivity, Temperature, Depth
KLD	Kullback-Leibler Divergence
MAD	mean absolute deviation
MSL	Mean Sea Level
NRMSE	Normalised Root Mean Square Error
RMD	Rhine-Meuse Delta
RMSE	Root Mean Square Error
TKE	turbulent kinetic energy

# List of Publications

## Journal articles

**Wegman, T. M.**, Pietrzak, J. D., Horner-Devine, A. R., Dijkstra, H. A., & Ralston, D. K. (2025). Observations of Estuarine Salt Intrusion Dynamics During a Prolonged Drought Event in the Rhine-Meuse Delta. *Journal of Geophysical Research: Oceans*, 130(1), Article e2024JC021655. <https://doi.org/10.1029/2024JC021655> (Chapter 3)

**Wegman, T. M.**, Biemond, B., Piccolroaz, S., Horner-Devine, A. R., Dijkstra, H. A., & Pietrzak, J. D. (in review). Direct observations of turbulence in a salt wedge estuary. *Journal of Coastal Research*. (Chapter 2)

**Wegman, T. M.**, Pietrzak, J. D., Horner-Devine, A. R., Ralston, D. K. & Kranenburg, W. M. (in preparation). Influences of tides and winds on estuarine inflow conditions. (Chapter 4)

Gerritsma, A., Verlaan, M., **Wegman, T. M.**, Groenenboom, J., de Goede, E., van Kester, J., Zijl, F., Pietrzak, J. D. (submitted). On the performance of a standard  $k - \epsilon$  model to represent salt dynamics in a complex delta. *Estuarine, Coastal and Shelf Science*.

## Conference presentations

**Wegman, T. M.**, Pietrzak, J. D., Labeur, R. J., Kranenburg, W. M., Verlaan, M., On the role of trapped internal waves generated by topography on mixing in an estuary (online presentation), Ocean Sciences Meeting 2022, Online, 24 February – 4 March 2022.

**Wegman, T. M.**, Pietrzak, J. D., Kranenburg, W. M., Labeur, R. J., and Verlaan, M., Mixing contributions from resonant trapped internal waves generated by bottom topography in an estuary (oral presentation), EGU General Assembly 2022, Vienna, Austria, 23 – 27 May 2022, EGU22-5790, <https://doi.org/10.5194/egusphere-egu22-5790>, 2022.

**Wegman, T. M.**, Pietrzak, J. D., Horner-Devine, A. R., Dijkstra, H. A., Ralston, D. K., and Kranenburg, W. M., Preliminary analysis of salt intrusion observations during the extreme drought of 2022 (poster), NCK days 2023, Delft, The Netherlands, 29 - 31 March 2023.

**Wegman, T.M.**, Pietrzak, J.D., Horner-Devine, A.R., Dijkstra, H.A., Ralston, D.K., and Kranenburg, W.M., Unique salt intrusion observations during the severe drought of 2022 (oral presentation), EGU General Assembly 2023, Vienna, Austria, 23 – 28 Apr 2023, EGU23-9412, <https://doi.org/10.5194/egusphere-egu23-9412>, 2023.

**Wegman, T. M.**, Pietrzak, J. D., Horner-Devine, A. R., Dijkstra, H. A., Ralston, D. K., and Kranenburg, W. M., (2023). Rare salt intrusion observations during the exceptional drought of 2022 (poster), Coastal Ocean Dynamics Gordon Research Conference 2023, Smithfield, Rhode Island, United States, 18 - 23 June 2023.

**Wegman, T. M.**, Pietrzak, J. D., Horner-Devine, A. R., Dijkstra, H. A., Ralston, D. K., and Kranenburg, W. M.,. Response of a salt wedge estuary to extremely low river discharge (oral presentation), Ocean Sciences Meeting 2024, New Orleans, Louisiana, United States, 18 - 23 February 2024.

**Wegman, T. M.**, Pietrzak, J. D., Horner-Devine, A. R., Dijkstra, H. A., Ralston, D. K., What drives salt intrusion in a low-lying river delta during an exceptional drought? (oral presentation), Physics of Estuaries and Coastal Seas 2024, Bordeaux, France, 23 - 27 September 2024.

## Datasets

**Wegman, T. M.**, van Keulen, D., Pietrzak, J. D., Horner-Devine, A. R., Dijkstra, H. A., & Ralston, D. (2025). Dataset underlying the study "Observations of Estuarine Salt Intrusion Dynamics During a Prolonged Drought Event in the Rhine-Meuse Delta" (Version 2) [Data set]. 4TU.ResearchData. doi:10.4121/ABC2EB1F-9291-44BD-9810-2EA0E98AE7EB.V2

**Wegman, T. M.**, Biemond, B., Piccolroaz, S., Horner-Devine, A. R., Dijkstra, H. A., & Pietrzak, J. D. (2024). Dataset underlying the study "Direct observations of turbulence in a salt wedge estuary" (Version 1) [Data set]. 4TU.ResearchData. doi:10.4121/BCF32F81-291A-4D60-BE5E-90A92CA37AA1.V1

# Curriculum Vitae



March 25, 1996    Born in Willemstad, Curaçao

## Education

- 2008 – 2014    Tweetaling Voortgezet Wetenschappelijk Onderwijs  
't Atrium, Amersfoort, The Netherlands
- 2014 – 2018    Bachelor of Science in Civil Engineering  
Delft University of Technology, Delft, The Netherlands  
B.Sc. thesis "HT-ATES system case study on TU Delft campus:  
Increasing efficiency with density difference compensation  
with the application of saline groundwater from deeper layers"
- 2018 – 2021    Master of Science in Civil Engineering  
Delft University of Technology, Delft, the Netherlands  
M.Sc. thesis "Undular bottom topography as a salt intrusion  
mitigation measure: A study on the potential of trapped  
internal waves to enhance vertical mixing"
- 2021 – 2026    PhD candidate at the department of Hydraulic Engineering  
Delft University of Technology, Delft, The Netherlands

## Professional Experience

- 2020 – 2021    Graduation intern  
Deltares, Delft, The Netherlands
- 2019    Intern Estimating & Engineering  
Van Oord, Rotterdam, The Netherlands
- 2018    Project Engineer Geotechnical Consultant  
BT Geoconsult, The Hague, The Netherlands



